Cell

Article

# Tissue-resident FOLR2$^+$ macrophages associate with CD8$^+$ T cell infiltration in human breast cancer

## Graphical abstract

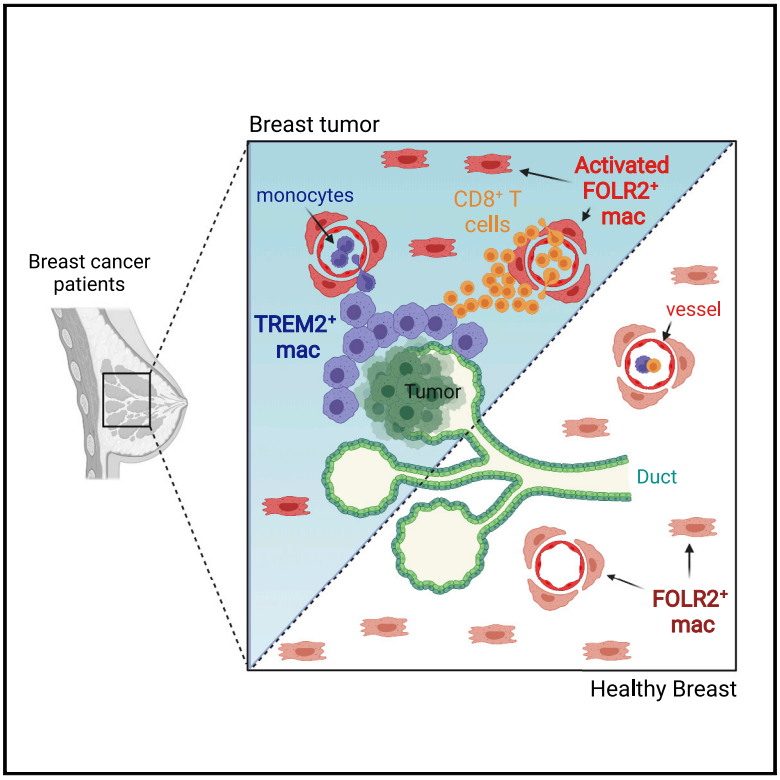


## Highlights

- FOLR2$^+$ macrophages are tissue-resident cells found in healthy and malignant breasts
- FOLR2$^+$ macrophages reside in a perivascular niche in the tumor stroma
- FOLR2$^+$ macrophages interact with tumor-infiltrating CD8$^+$ T cells
- FOLR2$^+$ macrophages positively correlate with T cell infiltration and better prognosis

## Authors

Rodrigo Nalio Ramos, Yoann Missolo-Koussou, Yohan Gerber-Ferder, ..., Pierre Guermonprez, Eliane Piaggio, Julie Helft

## Correspondence

julie.helft@inserm.fr

## In brief

A subset of macrophages marked by FOLR2 that interact with tumor-infiltrating CD8$^+$ T cells are associated with favorable prognosis.

Nalio Ramos et al., 2022, Cell *185*, 1189–1207
March 31, 2022 
https://doi.org/10.1016/j.cell.2022.02.021

CellPress

Cell

CellPress

Article

# Tissue-resident FOLR2$^+$ macrophages associate with CD8$^+$ T cell infiltration in human breast cancer

Rodrigo Nalio Ramos,[1,17,14,15] Yoann Missolo-Koussou,[1,17] Yohan Gerber-Ferder,[1,18] Christian P. Bromley,[2,18] Mattia Bugatti,[3] Nicolas Gonzalo Núñez,[1,16] Jimena Tosello Boari,[1] Wilfrid Richer,[1] Laurie Menger,[4] Jordan Denizeau,[1] Christine Sedlik,[1] Pamela Caudana,[1] Fiorella Kotsias,[1] Leticia L. Niborski,[1] Sophie Viel,[1] Mylène Bohec,[6] Sonia Lameiras,[6] Sylvain Baulande,[6] Laëtitia Lesage,[7] André Nicolas,[7] Didier Meseure,[7] Anne Vincent-Salomon,[7] Fabien Reyal,[8] Charles-Antoine Dutertre,[9] Florent Ginhoux,[9,10] Lene Vimeux,[11] Emmanuel Donnadieu,[11] Bénédicte Buttard,[12] Jérôme Galon,[12] Santiago Zelenay,[2] William Vermi,[3,5] Pierre Guermonprez,[13] Eliane Piaggio,[1,19] and Julie Helft[1,19,20,*]

[1]PSL University, Institut Curie Research Center, INSERM U932 & SiRIC, Translational Immunotherapy Team, 75005 Paris, France
[2]Cancer Inflammation and Immunity Group, Cancer Research UK Manchester Institute, The University of Manchester, Alderley Park, Manchester, UK
[3]Department of Pathology, University of Brescia, Brescia 25123, Italy
[4]PSL University, Institut Curie Research Center, INSERM U932, 75005 Paris, France
[5]Department of Pathology and Immunology, Washington University School of Medicine, St. Louis, MO 63110, USA
[6]PSL University, Institut Curie Research Center, Institut Curie Genomics of Excellence Platform, 75005 Paris, France
[7]PSL University, Institut Curie Hospital, Department of Pathology, 75005 Paris, France
[8]PSL University, Institut Curie Hospital, Department of Surgery, 75005 Paris, France
[9]Université Paris-Saclay, Institut Gustave Roussy, INSERM U1015, Villejuif, France
[10]Singapore Immunology Network, Agency for Science, Technology and Research, Singapore 138648, Singapore
[11]University of Paris, Institut Cochin, INSERM U1016, CNRS UMR 8104, 75014 Paris, France
[12]INSERM, Sorbonne Université, Université de Paris, Centre de Recherche des Cordeliers, Laboratory of Integrative Cancer Immunology, Paris, France
[13]Université de Paris, Centre for Inflammation Research, CNRS ERL8252, INSERM1149, Paris, France
[14]Present address: Laboratory of Medical Investigation in Pathogenesis and Directed Therapy in Onco-Immuno-Hematology (LIM-31), Department of Hematology and Cell Therapy, Hospital das Clínicas HCFMUSP, Faculdade de Medicina, University of São Paulo, São Paulo, Brazil
[15]Present address: Instituto D'Or de Ensino e Pesquisa, São Paulo, Brazil
[16]Present address: Institute of Experimental Immunology, University of Zurich, Zurich, Switzerland
[17]These authors contributed equally
[18]These authors contributed equally
[19]These authors contributed equally
[20]Lead contact
*Correspondence: julie.helft@inserm.fr
https://doi.org/10.1016/j.cell.2022.02.021

## SUMMARY

Macrophage infiltration is a hallmark of solid cancers, and overall macrophage infiltration correlates with lower patient survival and resistance to therapy. Tumor-associated macrophages, however, are phenotypically and functionally heterogeneous. Specific subsets of tumor-associated macrophage might be endowed with distinct roles on cancer progression and antitumor immunity. Here, we identify a discrete population of FOLR2$^+$ tissue-resident macrophages in healthy mammary gland and breast cancer primary tumors. FOLR2$^+$ macrophages localize in perivascular areas in the tumor stroma, where they interact with CD8$^+$ T cells. FOLR2$^+$ macrophages efficiently prime effector CD8$^+$ T cells *ex vivo*. The density of FOLR2$^+$ macrophages in tumors positively correlates with better patient survival. This study highlights specific roles for tumor-associated macrophage subsets and paves the way for subset-targeted therapeutic interventions in macrophages-based cancer therapies.

## INTRODUCTION

Macrophages are a major cellular component of the breast tumor microenvironment (Cassetta and Pollard, 2018). The extent of macrophage infiltration in tumors correlates with poor clinical outcome (Zhao et al., 2017). Indeed, tumor-associated macrophages (TAMs) play protumorigenic roles by promoting angiogenesis, by providing tumor growth factors, and by enhancing

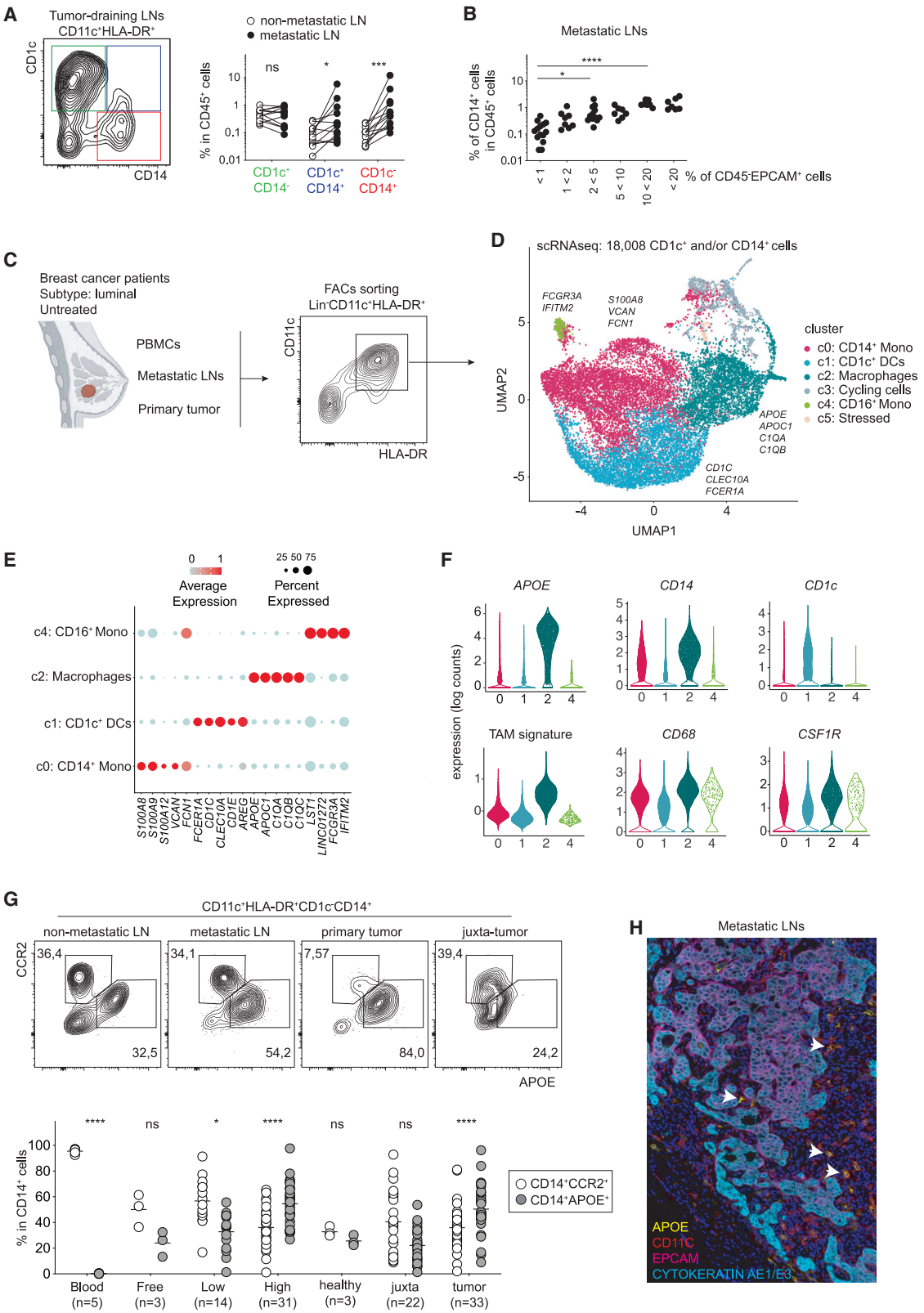


(legend on next page)

tumor cell invasion and metastasis (Ruffell and Coussens, 2015). TAMs also exert immunosuppressive functions thereby preventing tumor cell destruction by NK and T lymphocytes (Lewis and Pollard, 2006; Engblom et al., 2016). Therefore, targeting TAM recruitment, survival, and function has become a major therapeutic goal (Ries et al., 2014; Mantovani et al., 2017). Even though the current paradigm ascribes protumorigenic functions to TAMs, several studies have highlighted protective roles for TAMs in specific disease stages or organs (Ruffell and Coussens, 2015; Bonapace et al., 2014; Hanna et al., 2015). Distinct populations of macrophages with opposite pro- and anti-tumorigenic functions might coexist within the same tumor (Mantovani et al., 2004; Ali et al., 2016). Therefore, establishing the extent of heterogeneity in the macrophage compartment is a prerequisite for the rational design of macrophage-targeting therapies. Macrophage heterogeneity might potentially arise from (1) alternative activation states (Mantovani et al., 2017), (2) imprinting by tissue- or tumor-associated cues defining macrophage niches (Cassetta et al., 2019; Guilliams and Scott, 2017), (3) distinct TAM ontogenetic origins (adult monocyte versus embryonic progenitors) (Franklin et al., 2014; Loyher et al., 2018), and (4) tumor-induced systemic modification of circulating monocytes (Gallina et al., 2006; Cassetta et al., 2019; Ramos et al., 2020). In human breast cancer (BC), macrophage infiltration has been assessed with markers such as CD14, CSF1R, or CD68 (Ruffell et al., 2012; Cassetta et al., 2019; Leek et al., 1996; Yuan et al., 2014). However, CD14 and CSF1R also mark undifferentiated monocytes, whereas CD68 expression among phagocytes is not fully characterized (Colonna et al., 2004). Other markers like CD163, TIE2, MRC1/CD206, or MARCO have been implemented to assess TAM phenotypic heterogeneity (Cassetta and Pollard, 2018). Pioneer single-cell RNA sequencing (scRNA-seq) studies have invalidated alternative activation as the main mechanism accounting for TAM heterogeneity (Azizi et al., 2018). In summary, the phenotypic and functional diversities of TAM infiltrating human BC remain to be elucidated.

Here, we implement scRNA-seq of tumor-associated $CD14^+HLA\text{-}DR^+$ cells isolated from metastatic lymph nodes (LNs) and primary breast tumors to assess the cellular heterogeneity within the $CD14^+$ compartment. We identify two phenotypically distinct macrophage populations: (1) $TREM2^+$ macrophages expressing triggering receptor expressed by myeloid cells-2 (*TREM2*) and osteopontin (*SPP1*) genes, (2) $FOLR2^+$ macrophages expressing folate receptor 2 (FOLR2), hyaluronan receptor (*LYVE-1*), and mannose receptor C-Type 1 (*MRC1/CD206*) genes. We show that $TREM2^+$ and $FOLR2^+$ TAMs are evolutionarily conserved between human and mouse BC. $TREM2^+$ macrophages are poorly represented in healthy breast tissues but increase with tumor development. By contrast, we show that $FOLR2^+$ macrophages are tissue-resident macrophages (TRMs) populating healthy mammary glands (MGs) prior the onset of cancer development. Specific gene signatures defining $FOLR2^+$ macrophages correlate with better survival of patients with BC. Accordingly, $FOLR2^+$ macrophages positively correlate with signatures of major cellular players of antitumor immunity, including $CD8^+$ T cells. We further show that $FOLR2^+$ macrophages locate in the tumor stroma near vessels and cluster with $CD8^+$ T cell aggregates. This $FOLR2^+$ macrophage/$CD8^+$ T cell colocalization correlates with favorable clinical outcomes suggesting an antitumorigenic role for this newly characterized macrophage subset.

## RESULTS

### APOE expression defines TAMs in human BC

To unambiguously identify TAMs within breast tumors, we sought to define specific features enabling their distinction from infiltrating $CD14^+CD1c^-$ monocytes, $CD14^+CD1c^+$ inflammatory DCs/DC3 or $CD14^-CD1c^+$ cDC2 (Villani et al., 2017; Bourdely et al., 2020; Dutertre et al., 2019). First, we quantified mononuclear phagocytes of matched primary tumors—non-metastatic and metastatic LNs—from a cohort of treatment-naive patients with luminal BC (Table S1). We found that $CD1c^-CD14^+$ monocyte/macrophage population increased most significantly in metastatic LNs as compared with matched non-metastatic LNs (Figures 1A and S1A). $CD14^+$ cell infiltration correlated with the extent of tumor invasion in LNs (Figure 1B). We next sought to characterize the heterogeneity within the entire tumor-infiltrating $CD14^+$ cells in an unbiased manner. To this end, we isolated mononuclear phagocytes from metastatic LNs, primary tumors, and blood of untreated patients with luminal BC by FACS-sorting $CD11c^+HLA\text{-}DR^+$ cells and performed scRNA-seq (Figure 1C; Table S1). We used the SEURAT pipeline to process the data (Figure 1D) and merged ~18,000 myeloid cells from all the patients (Figures 1D and S1B). Louvain graph-based clustering identified 4 clusters of mononuclear phagocytes and populations of cycling (*mKI67*, *TOP2A*, and *CDC20*) and "stressed" cells (*HSPA1A* and *HSPB1*) (Figure S1C; Table S2). Cluster 0 (c0) was characterized by the selective expression of markers defining $CD14^+CD16^-$ monocytes (*S100A8*, *S100A9*, *S100A12*, and *VCAN*) (Villani et al., 2017; Figures 1D and 1E; Table S2). Cluster 1 (c1) was characterized by genes defining $CD1c^+$ DCs, whereas cluster

**Figure 1. APOE expression defines tumor-associated macrophages in human breast cancer**

(A) Flow cytometry analysis of myeloid cells in patient-matched non-metastatic and metastatic LNs (n = 13 patients). Wilcoxon matched-pairs signed rank test.

(B) Flow cytometry analysis of $CD14^+$ cells in metastatic LNs stratified according to $CD45^-EPCAM^+$ tumor cells frequency (n = 55 patients). One-way ANOVA, Tukey multiple test.

(C) Pipeline for scRNA-seq of BC patient myeloid cells (n = 6 patients).

(D) UMAP of scRNA-seq data merged from blood, metastatic LNs, and primary tumors (n = 18,008 cells). Representative genes from each cluster are depicted.

(E) Top five most significant expressed genes across clusters. Circles sizes represent percentage of cells within a cluster expressing a gene. Color represents the average expression of each gene.

(F) Expression distributions of selected genes of interest.

(G) Flow cytometry analysis of $CD14^+CCR2^+$ monocytes versus $CD14^+APOE^+$ macrophages in healthy or metastatic LNs and breast tissues. Number of patients per group is indicated. Wilcoxon matched-pairs signed rank test.

(H) Immunofluorescence images of $APOE^+$ macrophages and $EPCAM^+CK^+$ tumor cells in a representative metastatic LN.

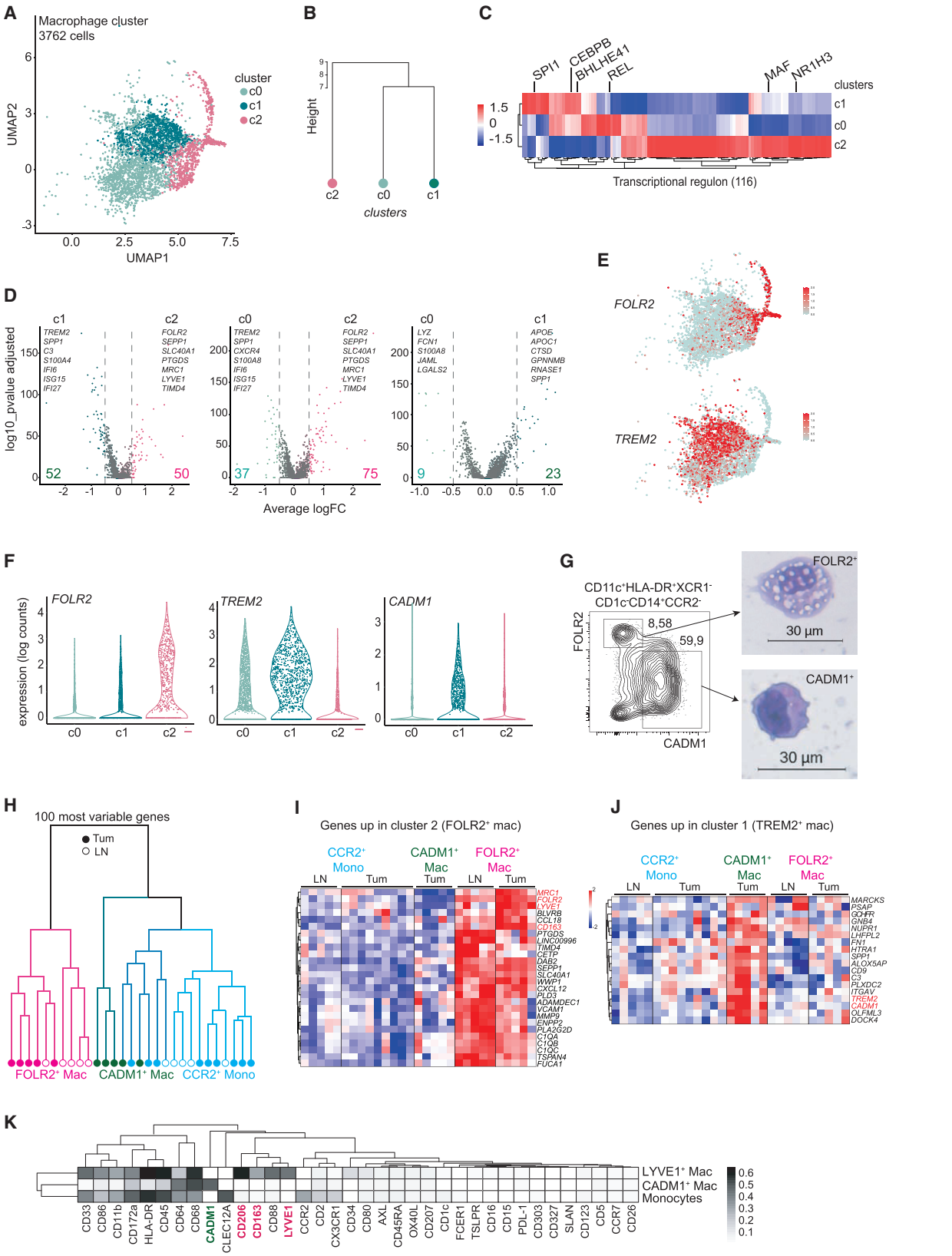


*(legend on next page)*

4 (c4) was identified as CD14$^-$CD16$^+$ monocytes (Villani et al., 2017; Dutertre et al., 2019; Bourdely et al., 2020). Cluster 2 (c2) was identified as TAMs because it selectively expressed high levels of a TAM signature (Figure 1F; Azizi et al., 2018). Cluster 2 expressed high levels of *APOE*, *APOC1*, *C1QA*, and *C1QC* enabling the distinction from monocytes (Figures 1E and S1D). We show that homogenous expression of APOE selectively discriminate TAMs from both CD14$^+$ monocytes and CD1c$^+$ DCs (Figure 1F). No other commonly used markers (*CSF1R*, *CD68*, and *CD14*) achieved this discrimination (Figure 1F). We next validated protein expression distinguishing macrophages/TAMs from monocytes within CD1c$^-$CD14$^+$ cells. The best monocyte/macrophage discrimination was obtained by staining with APOE and CCR2 (Figures 1G and S1E). We analyzed the contribution of CCR2$^+$ monocytes versus APOE$^+$ macrophages to the CD14$^+$ cell compartment within luminal BC lesions and tumor-free tissues. We found that the frequency of APOE$^+$ macrophages increased with tumor burden, whereas the frequency of CCR2$^+$ monocytes decreased (Figure 1G). Finally, we found that APOE$^+$ cells located near and inside the tumor lesions in metastatic LNs and primary tumors (Figures 1H and S1F). Altogether, our results establish APOE as a specific marker to identify macrophages in luminal BC primary tumors and metastatic LNs.

## Single-cell RNA sequencing reveals two subsets of APOE$^+$ macrophages

We next investigated the heterogeneity of APOE$^+$ TAMs. Louvain graph-based clustering identified 3 clusters of TAMs (Figures 2A, S2A, and S2B). Hierarchical clustering showed that clusters 0 and 1 (c0 and c1) were transcriptionally closer to each other as compared with cluster 2 (c2) (Figure 2B). To further explore the transcriptional heterogeneity found within the APOE$^+$ macrophages, we implemented single-cell regulatory network inference and clustering (SCENIC) to study the gene regulatory network (regulon) of each macrophage cluster. Hierarchical clustering revealed that c0 and c1 shared around half of their regulons including CEBPB and BHLHE41, whereas c2 presented mostly unique regulons like NR1H3 and MAF (Figure 2C; Table S2). Analysis of differentially expressed genes (DEGs) revealed that *FOLR2*, *SEPP1*, *SLC40A1*, *MRC1*, and *LYVE1* discriminated c2 from both c0 and c1 (Figure 2D; Table S2). Conversely, *TREM2*, *SPP1*, and *ISG15* discriminated both c0 and c1 from c2 (Figure 2D; Table S2). Altogether, we show that *FOLR2* is a defining marker for c2, whereas *TREM2* defines c0 and c1 (Figure 2E). We conclude that APOE$^+$ TAMs comprise two distinct populations: the TREM2$^+$ macrophages and the FOLR2$^+$ macrophages.

We next sought to validate this finding by prospective isolation of these populations for bulk transcriptome analysis. We searched for surface proteins differentially expressed between the two populations. We failed to detect TREM2 at the cell surface of TAMs after tissue dissociation. Alternatively, we found that c1 (TREM2$^{high}$ macrophages) specifically expressed and stained positive for CADM1 (Figures 2F, 2G, and S2C). Flow cytometry analysis of FOLR2 and CADM1 expression revealed mutually exclusive expression patterns within CD11c$^+$HLADR$^+$XCR1$^-$CD1c$^-$CCR2$^-$CD14$^+$ macrophage population (Figure 2G). We isolated FOLR2$^+$CADM1$^-$ and FOLR2$^{low}$CADM1$^+$ macrophages from primary tumors and metastatic LNs by FACS sorting (Figure S2D). FOLR2$^+$CADM1$^-$ macrophages presented a typical macrophage shape and were filled with vacuoles. In contrast, FOLR2$^{low}$CADM1$^+$ macrophages were smaller in size, with a morphology closer to monocytes (Figure 2G). We next performed bulk RNA-seq on FOLR2$^+$CADM1$^-$ macrophages, FOLR2$^{low}$CADM1$^+$ macrophages, and CD14$^+$CCR2$^+$ monocytes (Figures 2H–2J; Table S1). Hierarchical clustering showed that FOLR2$^+$CADM1$^-$ macrophages from primary tumors and metastatic LNs clustered together away from FOLR2$^{low}$CADM1$^+$ macrophages or CD14$^+$CCR2$^+$ monocytes (Figure 2H). We confirmed our scRNA-seq results showing that FOLR2$^+$ macrophages isolated from metastatic LNs or primary tumors expressed higher levels of *FOLR2*, *SEPP1*, *SLC40A1*, and *LYVE1* as compared with FOLR2$^{low}$CADM1$^+$ macrophages and CD14$^+$CCR2$^+$ monocytes (Figures 2I and S2E). FOLR2$^{low}$CADM1$^+$ macrophages from primary tumors clustered together with CD14$^+$CCR2$^+$ monocytes (Figure 2H) but specifically expressed *TREM2* and genes found to be overexpressed in c1 (*C3*, *FN1*, and *SPP1*) of the scRNA-seq analysis (Figure 2J). Some of these phenotypic differences were confirmed by CyTOF profiling of CD14$^+$CCR2$^-$ macrophages from metastatic LNs. Coexpression of LYVE1, MRC1/CD206, and CD163 was found in a macrophage population distinct from CADM1$^+$ expressing macrophages (Figure 2K). Altogether, our results show that breast TAMs comprise two populations separable by their mutually exclusive expression of TREM2/CADM1 and FOLR2.

**Figure 2. Single-cell RNA sequencing reveals two subsets of APOE$^+$ macrophages**

(A) UMAP visualization of APOE$^+$ macrophages (n = 3,762 cells).

(B) Hierarchical clustering of c0, c1, and c2 based on average gene expression (1,200 genes).

(C) Heatmap and hierarchical clustering of differentially predicted transcriptional regulons.

(D) Volcano plot showing DEG between each cluster. Selected genes among the Top25 were depicted.

(E) UMAP showing mutually exclusive expression of *TREM2* and *FOLR2* in *APOE*$^+$ macrophages.

(F) Expression distributions of *FOLR2*, *TREM2*, and *CADM1* across *APOE*$^+$ macrophage clusters.

(G) Representative flow cytometry plot and cytospin images from FOLR2$^+$ and CADM1$^+$ macrophages isolated from metastatic LNs and primary tumors. Scale bars, 30 μ.

(H) Hierarchical clustering using the 100 most variable genes from bulk RNA-seq of FOLR2$^+$ macrophages, CADM1$^+$ macrophages, and CCR2$^+$ monocytes isolated from metastatic LNs and primary tumor of untreated patients with luminal BC (n = 12 patients).

(I and J) Heatmap of the DEG between *FOLR2*$^+$ (C2) and *TREM2*$^{high}$ (C1) macrophages selected from scRNA-seq dataset and applied to bulk RNA-seq of FOLR2$^+$ macrophages, CADM1$^+$ macrophages, and CCR2$^+$ monocytes.

(K) Protein expression analysis (CyTOF) in CD14$^+$CCR2$^+$ monocytes, CD14$^+$CCR2$^-$CD68$^+$LYVE1$^+$ macrophages, and CD14$^+$CCR2$^-$CD68$^+$CADM1$^+$ macrophages in metastatic LNs (n = 6 patients).

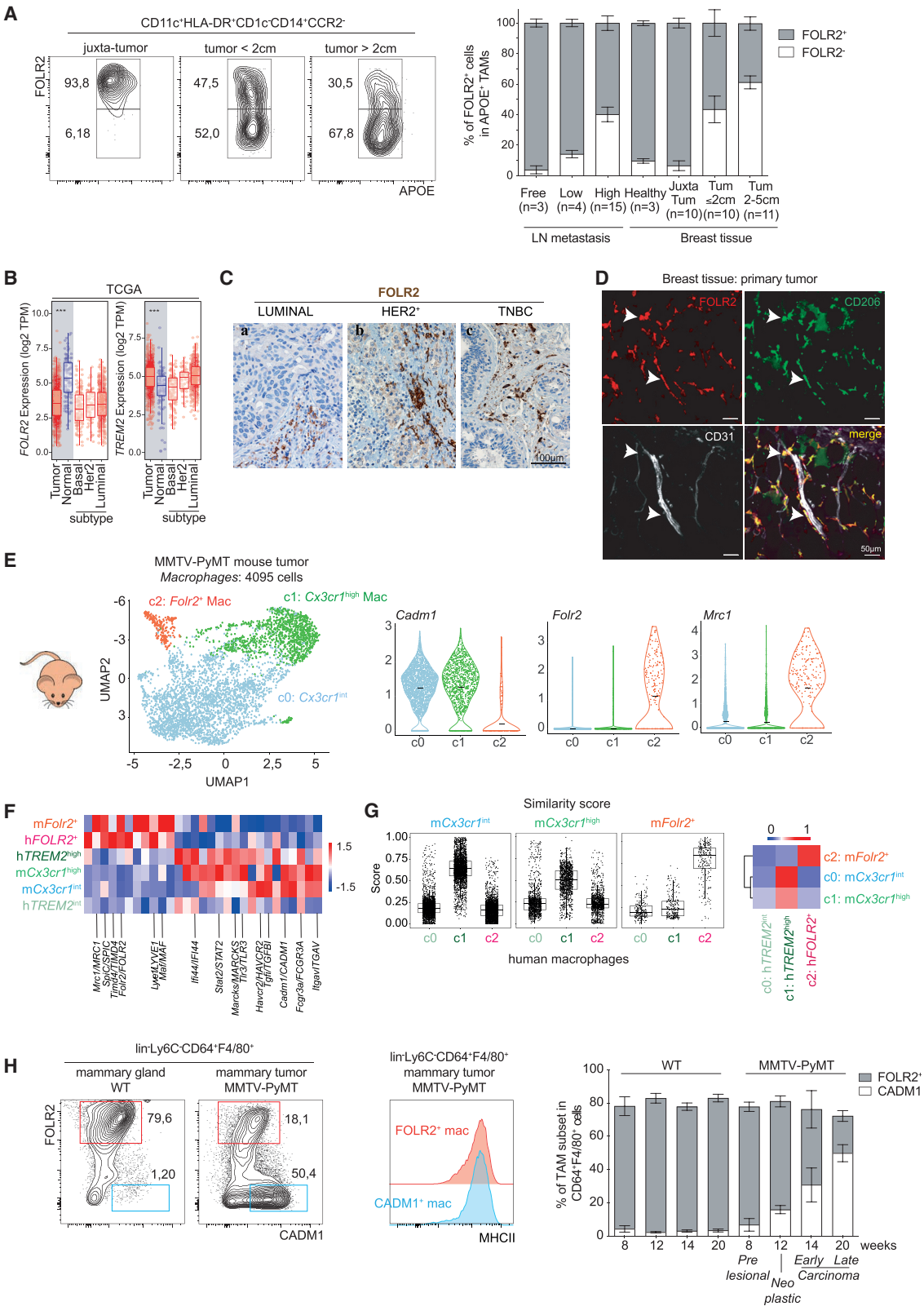


*(legend on next page)*

### FOLR2$^+$ macrophages are tissue-resident macrophages

A recent study identifies the infiltration of TREM2$^+$ macrophages as an event associated to cancer development (Molgora et al., 2020). Our data establish their transcriptional proximity to CD14$^+$CCR2$^+$ monocytes in breast tumors (Figure 2H). These results suggest that TREM2$^+$CADM1$^+$ macrophages arise from infiltration of circulating monocytes during tumor progression. The origin of FOLR2$^+$ macrophages is not known, and we therefore wondered whether they correspond to mammary TRMs (i.e., present in healthy breast) or tumor-recruited monocyte-derived macrophages like the TREM2$^+$ macrophages. To address this question, we quantified FOLR2$^+$ macrophages by flow cytometry in healthy tissues versus luminal breast tumor lesion. We found that among APOE$^+$ macrophages, FOLR2$^+$ macrophages were enriched in healthy and juxta-tumor tissues (Figure 3A). Upon tumor progression, the frequency of FOLR2$^+$ macrophages got relatively diluted among APOE$^+$ macrophages by FOLR2$^-$ macrophages (comprising TREM2$^+$ macrophages) (Figure 3A). However, the population of FOLR2$^+$ macrophages did not decrease in tumor lesion as their frequency among total live cells remain constant between healthy and tumor tissue (Figure S3A). The enrichment of FOLR2$^+$ macrophages in adjacent normal tissue versus tumor lesions was also confirmed at the transcriptional level by analyzing BC samples of different subtypes (Her2$^+$, triple negative BC [TNBC], luminal) from The Cancer Genome Atlas (TCGA) database (Figures 3B and S3B; Li et al., 2017). In contrast, *TREM2* transcripts were enriched in breast tumor lesions as compared with tumor-adjacent normal and nondisease healthy tissues (Figures 3B and S3B). Immunohistochemistry (IHC) analysis revealed that FOLR2$^+$ macrophages were present in all subtypes of BC (Figure 3C). Bulk RNA-seq (Figure 2J) and CyTOF (Figure 2K) analysis of FOLR2$^+$ macrophages show that FOLR2$^+$ macrophages specifically express LYVE1 and MRC1/CD206, both markers of perivascular (PV) macrophages (Lin et al., 2006; Lim et al., 2018; Chakarov et al., 2019). Confocal imaging on tumor resection specimens showed that indeed FOLR2$^+$CD206$^+$ macrophages located near CD31$^+$ vessels in both tumor and adjacent tissue (Figures 3D and S3C). Altogether, these results show that FOLR2$^+$ macrophages are PV TRMs associated with healthy MGs.

We next analyzed macrophage subsets in healthy or malignant MGs in mouse models, enabling a longitudinal analysis of immune populations in steady state and during tumor progression. In a published scRNA-seq dataset performed on hematopoietic cells from healthy MGs (Han et al., 2018), we identified a subset of TRMs coexpressing *Folr2*, *Mrc1*, and *Lyve1*, like human FOLR2$^+$ macrophages (Figure S3D). These cells align to previously described MRC1$^+$LYVE1$^+$ TRMs (Franklin et al., 2014; Jäppinen et al., 2019; Wang et al., 2020; Figure S3G). We next performed scRNA-seq on CD45$^+$CD3$^-$CD19$^-$B220$^-$NKP46$^-$ cells isolated from breast tumors of the MMTV-PyMT (PyMT) autochthonous model developing mammary tumors that morphology closely resemble human luminal BC (Lin et al., 2003; Davie et al., 2007; Franklin et al., 2014; Figures 3E and S3E). Contaminating lymphocytes, *Ly6c2*$^+$ monocytes (c3), *Ly6c2*$^-$*Nr4a1*$^{high}$ monocytes (c6), cycling cells (c4), and cells with high content of ribosomal genes (c1) were excluded (Figure S3E). Among the remaining *Fcgr1*$^+$ cells, we identified 3 clusters of macrophages, among which, two expressed *Cadm1* (c0 and c1) (Figure 3E). In addition, we identified a discrete population of *Folr2*$^+$*Mrc1*$^+$ macrophages (c2). Mouse and human FOLR2$^+$ macrophages shared the expression of *FOLR2*, *MRC1*, *LYVE1*, and *MAF* (Figure 3F; Table S3). On the other hand, *Cadm1*$^+$*Cx3cr1*$^+$ mouse macrophages (c0 and c1) resembled human CADM1$^+$TREM2$^{high}$ macrophages (c1, Figure 2A) and shared the expression of *CADM1*, *HAVCR2*, *IFI44* (Figure 3F; Table S3). Of note, the *Trem2* expression pattern was more conspicuous in murine as compared with human macrophages (Figure S3F). To probe the similarity between human and mouse FOLR2$^+$ macrophages, we performed a similarity analysis across orthologous genes at the level of each cell (Figure 3G; Table S3). This unbiased analysis confirmed the marker-based alignment of murine *Folr2*$^+$ macrophage to human *FOLR2*$^+$ macrophages. Conversely, the *Cadm1*$^+$*Cx3cr1*$^+$ murine macrophages (c0 and c1) presented high similarity with CADM1$^+$TREM2$^+$ human macrophages. Thus, we conclude that FOLR2$^+$ macrophages are evolutionarily conserved between murine and human luminal mammary tumors.

We next analyzed longitudinally the dynamics of FOLR2$^+$ and CADM1$^+$ macrophages during tumor development by quantifying MG macrophages in healthy littermate (WT), prelesion

**Figure 3. FOLR2$^+$ macrophages are tissue-resident macrophages**

(A) Representative contour plots and quantification of FOLR2$^+$APOE$^+$ and FOLR2$^-$APOE$^+$macrophages across distinct BC patient tissues by flow cytometry. Number of patients per group is indicated. Data are represented as mean ± SEM.

(B) *FOLR2* and *TREM2* mRNA expression in tumor microarrays from patients with BC of the TCGA database. Tumor = 1,093 samples; normal n = 112 samples; basal n = 190 samples; Her2 n = 82 samples; and luminal n = 564 samples. Wilcoxon test.

(C) FOLR2 expression by immunohistochemistry. Sections are from 3 cases of primary BC showing luminal (a), HER2$^+$ (b), and triple negative (c) subtypes. Scale bars, 100μ.

(D) Representative confocal immunofluorescence images of BC tissues. White arrows indicate FOLR2$^+$CD206$^+$ macrophages colocalizing with CD31$^+$ vessels. Scale bar, 50μm.

(E) UMAP of *Fcgr1*$^+$ macrophages (n = 4,095 cells) isolated from mammary tumors of 23-week-old PyMT mice (n = 2). Expression distributions of *Cadm1*, *Folr2*, and *Mrc1* across *Fcgr1*$^+$ macrophages.

(F) Heatmap showing gene orthologs similarly expressed across mouse and human macrophage subsets.

(G) Similarity score (Seurat v3 reference label transfer integration). Graph plots showing prediction scores of each mouse macrophage cluster (Figure 3D) applied to each human macrophage cluster (Figure 2A). Each dot represents a cell. Heatmap of the mean of the prediction score.

(H) Quantification of FOLR2$^+$ and CADM1$^+$ mammary macrophages by flow cytometry during tumor development. Representative contour plots of macrophages in mammary tissues from tumor-free and tumor-bearing mice (20-week-old) are shown. Expression of MHC-II by FOLR2$^+$ and CADM1$^+$ macrophages isolated from mammary tumors. Bar plots represent the quantification of macrophage subsets in WT mammary glands (n = 16) or tumors (n = 16). Data are represented as mean ± SEM.

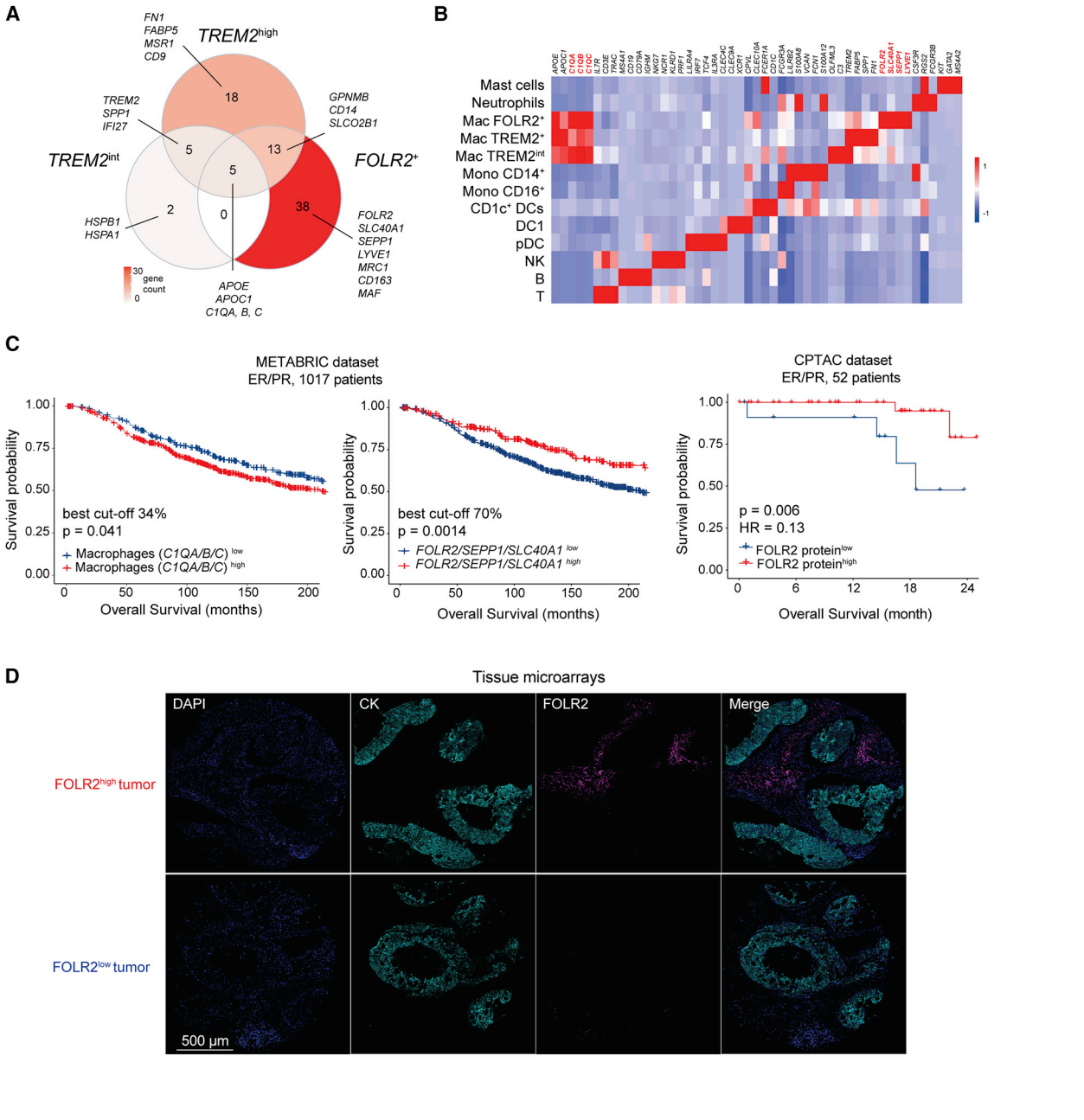


(legend on next page)

PyMT mice, neoplastic lesions, early carcinoma, and advanced carcinoma. We found that FOLR2$^+$ macrophages constitute around 80% of total macrophages in healthy MG (WT) (Figures 3H and S3I). The frequency, but not the absolute number, of FOLR2$^+$ macrophages progressively decreased upon carcinoma progression reaching a minimum of 10%–20% in advanced carcinoma lesion of 20-week-old PyMT mice (Figures 3H, S3H, and S3J). In contrast, carcinoma development was accompanied by the *de novo* expansion of CADM1$^+$ macrophages representing up to 80% of total macrophage in 20-week-old PyMT mice (Figure 3H). Altogether, we conclude that FOLR2$^+$ macrophages represent an evolutionarily conserved TRM subset persisting in advanced carcinoma.

## FOLR2$^+$ macrophages correlate with increased survival in patients with BC

Macrophages are generally thought to promote tumor growth and inhibit antitumor immunity. This is particularly well established in mouse models (Lin et al., 2006; Qian et al., 2011; Franklin et al., 2014; Linde et al., 2018). In human, macrophages generally correlate with poor prognosis and higher tumor grade. However, clinical studies have probed the association of macrophages to patient survival by using markers shared by DCs, monocytes, and macrophages (*CSF1R*, *CD68*, *MRC1/CD206*, and *CD163 e.g*) (Figures S2F and S2G). Therefore, we wondered whether FOLR2$^+$ macrophages are similarly associated with worse survival in patients with BC. To this end, we defined gene signatures enabling to infer the abundance of total macrophages or the FOLR2$^+$ macrophage subset within bulk tumor transcriptomes. Three genes (*C1QA*, *C1QB*, and *C1QC*) define a core macrophage signature shared by the 3 macrophage clusters identified in this study (Figures 2A and 4A) and suffice to distinguish macrophages from other leukocytes lineages (Figures 4A and 4B; Table S2). Three genes (*FOLR2*, *SEPP1*, and *SLC40A1*) uniquely distinguish FOLR2$^+$ macrophages from other macrophages and other leukocytes lineages (Figures 4A and 4B; Azizi et al., 2018; Table S2). *LYVE1* was not included in the signature because of its endothelial expression. We analyzed the representation of these gene signatures within bulk transcriptomes of luminal BC (Curtis et al., 2012). In accordance with previous reports (Ruffell and Coussens, 2015), we found that the highest level of macrophage infiltration correlated with worse overall survival (Figures 4C and S4A). In stark contrast, high FOLR2 gene signature correlated with increased overall survival (Figures 4C and S4A). The association between the FOLR2 gene-signature and patient clinical outcome was confirmed in an independent BC patient cohort using the same cutoff (Wang et al., 2005a; Figure S4B). We also analyzed the association between FOLR2 protein expression and patient prognosis within 52 ER$^+$/HER2$^-$ patients with BC from the CPTAC dataset. We found that FOLR2 protein abundance positively correlated with better survival (Figure 4C). We next wanted to directly assess if the cellular density of FOLR2$^+$ macrophages was associated with favorable clinical outcomes. To this end, we used multispectral imaging to analyze tissue microarrays comprising tumors from two retrospective and independent cohorts of patients with BC. We stained the tumors for FOLR2, cytokeratin (CK), and 4′,6-diamidino-2-phenylindole (DAPI) and calculated the cellular density of FOLR2$^+$ macrophages (Figure 4D). Using the best performing threshold as a cutoff, we found that FOLR2$^+$ macrophage density positively correlated with patient survival (Figure 4E). Since FOLR2$^+$ macrophages are a tissue-resident population in healthy MG, *FOLR2* mRNA abundance could be associated to smaller tumors. To test whether this could be a confounding factor, we analyzed the level of expression of *FOLR2* mRNA for breast tumors of different stages and grade. We found no significant differences in *FOLR2* expression between grades and a slight increase in late-stage tumors (Figure S4C). Moreover, multivariate analysis of the prognostic value of the FOLR2 gene signature adjusted for various clinical parameters showed that the FOLR2 gene signature was an independent prognostic factor correlated with better survival of patients with luminal BC (Figure S4D, S4E, and S4F). Altogether, these results showed that the FOLR2 gene signature and FOLR2$^+$ macrophage abundance associate with better prognosis in patients with BC.

## FOLR2$^+$ macrophages reside in the tumor stroma and are spatially separated from TREM2$^+$ macrophages across cancers

We have shown that FOLR2$^+$ macrophages are MG TRMs. Moreover, others have recently shown that macrophages expressing FOLR2 are found in healthy human tissues (Samaniego et al., 2014; Sharma et al., 2020; Thomas et al., 2021). Therefore, we wondered whether we could detect FOLR2$^+$ macrophages across cancer types. To address this question, we analyzed the spatial distribution of FOLR2$^+$ cells in 80 histological tumor sections of distinct human cancers (Table S1). We found FOLR2$^+$ macrophages across all these cancers (Figures 5A and S5A). Spatial distribution quantification showed that FOLR2$^+$ cells were consistently found within the tumor stroma and rarely infiltrated tumor nests (Figures 5A and S5B). We stained FOLR2 and TREM2 on serial sections of various cancer types and

**Figure 4. FOLR2$^+$ macrophages correlate with increased survival in patients with breast cancer**

(A) Venn diagram showing specific and common DEG ($log_2$(FC) > 0.75) of each APOE$^+$ macrophages clusters (Figure 2A).

(B) Heatmap showing mean expression of specific genes discriminating tumor-infiltrating immune cell populations in a published scRNA-seq dataset of CD45$^+$ cells isolated from patients with BC (Azizi et al., 2018).

(C) Kaplan-Meier survival curves generated for a macrophage gene signature (*C1QA/C1QB/C1QC*) and a FOLR2$^+$ TAM gene signature (*FOLR2/SEPP1/SLC40A1*) in the METABRIC luminal BC cohort (n = 1,017 patients). Patients were divided in high- and low-expressing groups based on the best cutoff. Kaplan-Meier survival curve generated for FOLR2 protein expression in the CPTAC luminal BC cohort (n = 52). Patients were divided in high- and low-expressing groups based on a 25% cutoff.

(D) Representative images of multiplex immunofluorescence from tissue microarray showing FOLR2$^{high}$ (top) and FOLR2$^{low}$ (bottom) profiles. Scale bars, 500 μ.

(E) Kaplan-Meier survival curves generated for FOLR2$^+$ macrophage density calculated by multispectral analysis of tumors from two independent cohorts (cohort 1: FOLR2$^{high}$ n = 76; FOLR2$^{low}$ n = 46; cohort 2: FOLR2$^{high}$ n = 36; FOLR2$^{low}$ n = 90). Graph shows the quantification of FOLR2$^+$ macrophage density in tumors. Patients were divided in high- and low-cell density groups based on best p value cutoff. Mann-Whitney test.

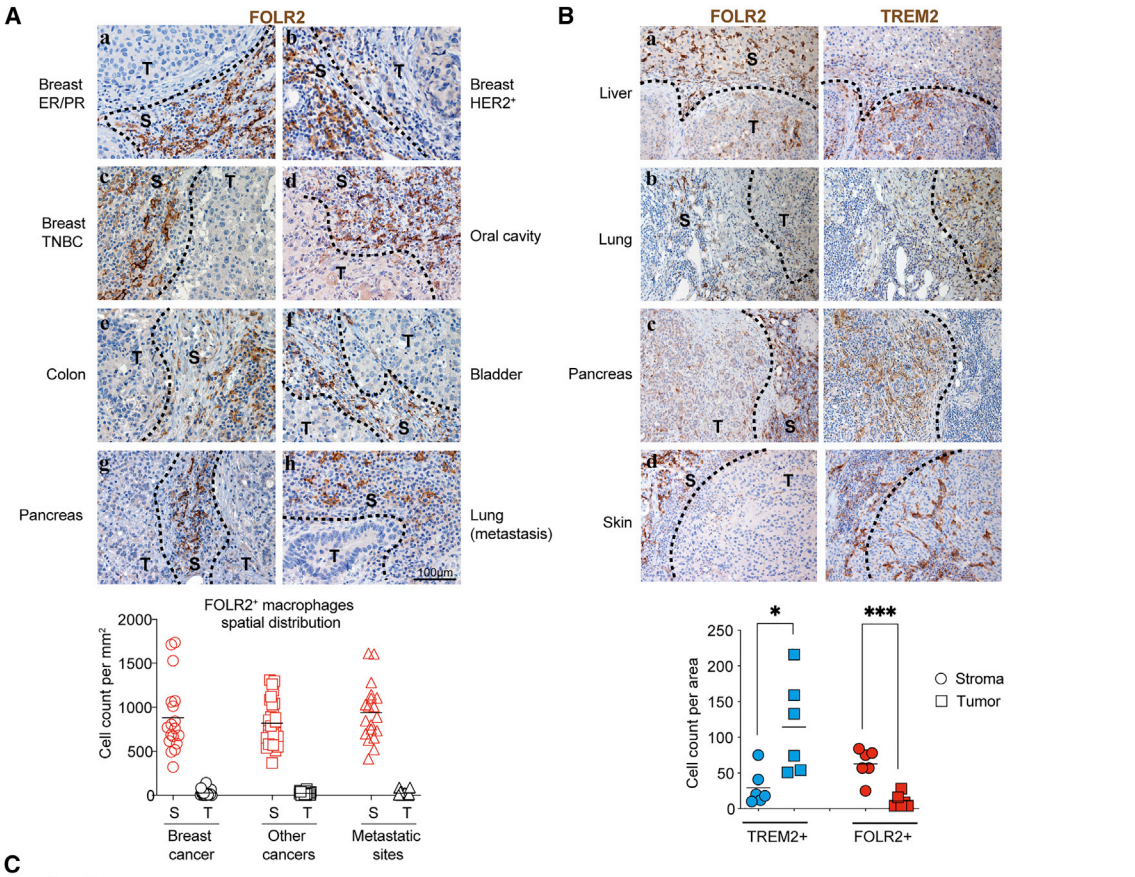


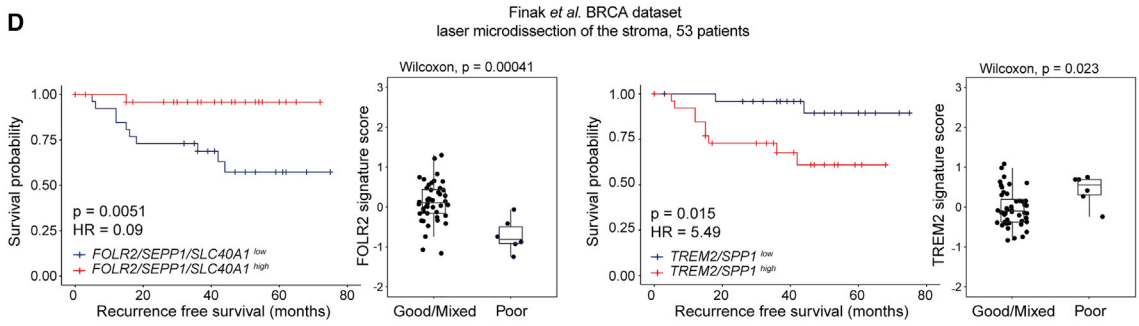


*(legend on next page)*

showed that they were often spatially separated (Figure 5B). TREM2$^+$ macrophages infiltrate or localize close to the tumor nest, whereas FOLR2$^+$ macrophages largely locate in the tumor stroma (Figure 5B). This spatial distribution was found in hepatocellular (Figure 5Ba), lung (Figure 5Bb), and pancreatic carcinomas (Figure 5Bc). In some cancers, TREM2$^+$ cells were found in both tumor stroma and tumor nests (Figures 5Bd and S5C), whereas FOLR2$^+$ cells remain located in the tumor stroma. Altogether, these results show that FOLR2$^+$ and TREM2$^+$ macrophages are associated with specific locations in the tumor microenvironment across various cancer types.

To quantitatively assess the spatial distribution of FOLR2$^+$ and TREM2$^+$ macrophages in breast tumors, we used multispectral imaging on the tissue microarray comprising tumors from 122 patients (Figure 4D). Tumor nests were identified by their expression of CK (Figure S5D). Automated classification of tumor regions (tumor nest CK$^+$ versus tumor stroma CK$^{NEG}$) and spatial distribution of FOLR2$^+$ and TREM2$^+$ cells were performed (Figure S5D). Consistent with our IHC results, we found that FOLR2$^+$ macrophages located in the tumor stroma at a mean distance of 95 μm from the tumor nest (Figures 5C and S5E). By contrast, TREM2$^+$ macrophages were found inside tumor nests and at the invasive margin near to tumor nests (mean distance 47 μm, Figure S5E). TREM2$^+$ macrophages surrounding the tumor nests often formed cells clusters (see IFs Figures S2C, S5E, and S5F). We conclude that FOLR2$^+$ macrophages mainly locate in the tumor stroma and are further away from tumor nests as compared with TREM2$^+$ macrophages (Figure 5C). In the tissue microarrays from cohorts 1 and 2 (Figures 4D and 4E), TREM2$^+$ cell density was not reproducibly and significantly associated with survival (Figure S5G). Interestingly, *TREM2* or the TREM2 gene-signature mRNA levels in the TCGA whole tumor transcriptome dataset was associated with worse survival in TNBC (Table S4 tab "TCGA"), kidney renal clear cell carcinoma (KIRC), pancreatic adenocarcinoma (PAAD), low grade glioma (LGG), and liver hepatocellular carcinoma (LIHC) (Table S4; Figure S5H). To test whether FOLR2$^+$ and TREM2$^+$ macrophage abundance in tumor stroma was associated with clinical outcome, we analyzed a microarray dataset generated by laser capture microdissection of BC peritumor stroma (Finak et al., 2008). We found that the FOLR2 gene signature strongly associated with better survival and that low FOLR2 gene-signature expressers had poor clinical outcome (Figure 5D). Conversely, patients with higher expression of the TREM2 gene signature had decreased survival probability and high expresser patients felt into the poor outcome patient group (Figure 5D).

In sum, we conclude that FOLR2$^+$ and TREM2$^+$ macrophages are spatially separated within the tumor microenvironment and that their abundance in tumor stroma associates to distinct clinical outcome for patients with BC.

## FOLR2$^+$ macrophages are enriched in CD8$^+$ T cell-infiltrated tumors and colocalize with lymphoid aggregates across cancers

To gain further functional insight, we used the FOLR2 gene signature or *FOLR2* expression alone to correlate abundance of FOLR2$^+$ macrophages with other immune and stromal cell types in the tumor microenvironment (Figure 6A; Table S4). We found that the FOLR2 gene signature (or *FOLR2* gene) positively correlated with known players of antitumor immunity like CD8$^+$ T cells, DCs, B cells, and tertiary lymphoid structures (TLSs) (Figures 6A and S6A). In contrast, TREM2$^+$ macrophage gene signature or *TREM2* expression alone did not correlate with T cells, CD8$^+$ T cells, NK cells, or B cells (Figure 6A). In addition, the highest level of *FOLR2* expression in bulk tumor transcriptomes coincides, in the same tumor, with coordinated infiltration by multiple lymphocyte lineages and a gene signature of TLS (Figure 6B). No correlation was found when patients were stratified according to levels of *TREM2* transcript (Figure 6B). We analyzed the gene pathways represented in all genes positively correlated to *FOLR2* (or *TREM2*) expression in whole tumor transcriptome (Figure S6B). We found a strong correlation between *FOLR2* expression in tumors and various immune pathways, including TCR and PD-1 signaling and antigen processing. We also analyzed gene pathways enriched in FOLR2$^+$ macrophages as compared with CADM1$^+$TREM2$^+$ macrophages in our bulk RNA-seq dataset and found that chemotaxis and functional modules of immune response regulation were gene pathways enriched in FOLR2$^+$ macrophages (Figures 6C and S6C; Bindea et al., 2009). Altogether, these results suggest that FOLR2$^+$ macrophages are part of an immune contexture underlying the onset of antitumor immunity.

Since CD8$^+$ T cells are associated to better survival in various cancer types including BC (DeNardo et al., 2011; Ali et al., 2014; Pagès et al., 2018), we investigated whether FOLR2$^+$ macrophages were interacting with tumor-infiltrating CD8$^+$ T cells. We used confocal microscopy on tumor resection samples and found that FOLR2$^+$ macrophages located near CD31$^+$ vessels were closely associated with CD8$^+$ T cell aggregates

**Figure 5. FOLR2$^+$ macrophages are spatially separated from TREM2$^+$ macrophages**

(A–C) Sections from breast carcinomas (a–c), oral cavity (d), colon (e), bladder (f), pancreas (g), lung (h) stained for FOLR2. Dotted line represents invasive margin. Scale bars, 100 μ. Quantification of the spatial distribution of FOLR2$^+$ macrophages in the tumor stroma (S) versus the tumor nest (T) in 80 tumor sections.

(B) Spatial distribution of FOLR2$^+$ TAMs and TREM2$^+$ TAMs in human primary carcinomas. Serial sections are from 6 cases of primary cancers including one hepatocellular (a), lung (b), and pancreatic carcinomas (c) and melanoma (d) stained as labeled. Scale bars, 100 μ. Quantification of the spatial distribution of FOLR2$^+$ and TREM2$^+$ macrophages in the tumor stroma (S) versus the tumor nest (T) in 10 tumor sections. Unpaired t test.

(C) Representative tumor spot of multiplex immunofluorescence from BC tissue microarray showing TREM2$^+$ (cyan) and FOLR2$^+$ (red) macrophages spatial distribution. Dotted line represents invasive margin. Quantification of the distance of FOLR2$^+$ or TREM2$^+$ macrophages to the tumor nest. Quantification of the spatial distribution of FOLR2$^+$ and TREM2$^+$ macrophages in the tumor stroma (S) versus the tumor nest (T) in 122 patients. Scale bars, 250 μ. Mann-Whitney test.

(D) Kaplan-Meier survival curves generated for a FOLR2$^+$ macrophage gene signature (*FOLR2*/*SEPP1*/*SLC40A1*) and a TREM2$^+$ macrophage gene signature (*TREM2*/*SPP1*) in the Finak et al. luminal ER/PR BC cohort (n = 53 patients). Quantification of the signatures in groups of patients with good/mixed versus poor prognosis. Wilcoxon test.

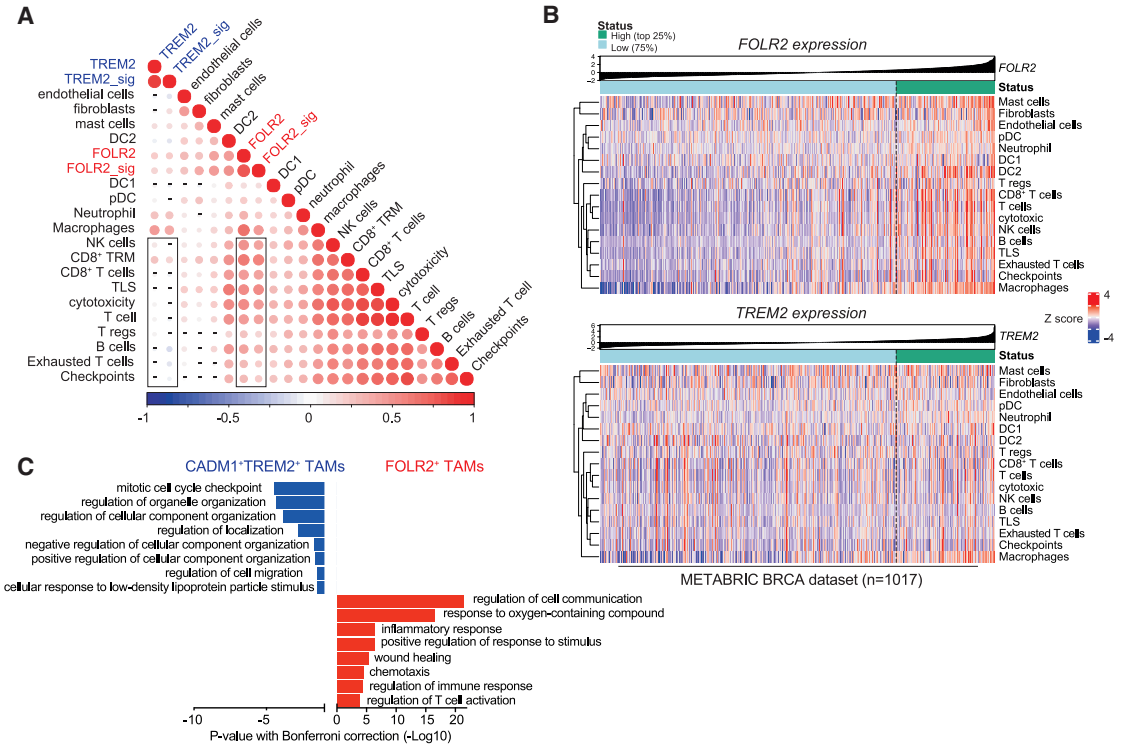


(legend on next page)

(Figure 6D). To confirm the spatial association between FOLR2$^+$ macrophages and CD8$^+$ T cells, we stained the previous tissue microarray patient cohorts for both CD8$^+$ and FOLR2$^+$ cells and calculated their respective cellular density. FOLR2$^+$ and CD8$^+$ cell densities were not significantly different between BC subtypes nor between tumor stages and grades (Figures S6D and S6E). However, tumors with high FOLR2$^+$ macrophage content had significantly higher CD8$^+$ T cell density than tumors with low FOLR2$^+$ macrophage content (Figures 6E and S6F). There was no significant association between the abundance of TREM2$^+$ cells and CD8$^+$ cell infiltration (Figures S5F and S6F). FOLR2$^+$ macrophages could also be detected within TLS (Figure S6G). Altogether, these results show that stroma-associated FOLR2$^+$ macrophages are structural component of lymphoid aggregates near tumor nests.

To further investigate whether FOLR2$^+$ macrophages productively engage with CD8$^+$ T cells, we performed confocal live imaging on fresh human BC lesions. We stained endogenous CD8$^+$ T cells, FOLR2$^+$ macrophages, and EPCAM$^+$ tumor cells from the tumor lesion with fluorescently coupled antibodies against CD8, FOLR2, and EPCAM and subsequently imaged the cellular dynamics by time-lapse microscopy (Figure 6F). We observed that FOLR2$^+$ macrophages localized within the tumor stroma and formed a network of sessile cells with active membrane ruffling (Video S1). Quantification of the speed of displacement of CD8$^+$ T cells showed a heterogeneous behavior with more or less motile cells. Importantly, we reproducibly found that CD8$^+$ T cells reduced their speed and established long-lasting contacts with FOLR2$^+$ macrophages (Video S1). This was in contrast with a higher motility of CD8$^+$ T cells in FOLR2-deprived tumor regions (Figure 6F; Videos S2 and S3). We conclude that CD8$^+$ T cells establish prolonged interactions with FOLR2$^+$ macrophages, a behavior likely to promote T cell activation. In line with this result, *FOLR2* expression in whole tumor transcriptome positively correlated with genes controlling cytotoxic function in T cells (*GZMA*, *GZMB*, *GZMK*, *PFR1*, *KLRB1*, and *KLRD1*) but not with genes of T cell dysfunction like *LAG3* (Figure 6G). *TREM2* expression showed no significant correlation with genes controlling the cytotoxic function of CD8$^+$ T cells.

It has been previously proposed that TAMs in the tumor stroma of lung or in pleural and peritoneal cavities sequester T cells from reaching the tumors and may have a negative impact on antitumor immunity (Peranzoni et al., 2018; Chow et al., 2021). In other studies, long-lasting interactions between antigen presenting cells and T cells precede T cell activation and may therefore promote T cell immunity (Hugues et al., 2004; Mempel et al., 2004). To assess whether CD8$^+$ T cell/macrophages interactions translate into favorable clinical outcome in BC, we performed a quantitative spatial analysis of the cellular interactions between CD8$^+$ T cells and macrophage subsets in T cell-infiltrated tumors. To this end, we performed multiplex imaging of tumors from <60 patients with BC, in which the density of CD8$^+$ T cells was superior to 50 CD8$^+$ T cells per mm$^2$. We quantified the percentage of CD8$^+$ T cells in close proximity (<30 μm) with either FOLR2$^+$ or TREM2$^+$ macrophages and stratified the patients according to the percentage "high" or "low" of CD8$^+$ T cells in close contact with these two macrophage subsets. We found that a high percentage of CD8$^+$ T cells in close contact with FOLR2$^+$ macrophages associated with a better outcome for patients with BC, whereas this was not the case for CD8$^+$ T cells interacting with TREM2$^+$ macrophages (Figure S6H). We therefore conclude that tumor-infiltrating CD8$^+$ T cells actively engage with FOLR2$^+$ macrophages and that this interaction positively correlates with CD8$^+$ T cell activation and patient survival.

## FOLR2$^+$ macrophages respond to tumor growth and acquire T cell-priming ability

Nascent tumors have been shown to engage in cellular cross talk with TRMs, which in turn promote tumor growth, motility, and invasiveness (Cassetta and Pollard, 2018). To explore the functional characteristics of FOLR2$^+$ macrophages, we turn to the PyMT BC murine model. First, we ask whether FOLR2$^+$ macrophages of healthy MG would respond to the developing tumor. To this end, we used bulk RNA-seq to profile FOLR2$^+$ macrophages isolated from healthy versus small or medium tumor murine MGs (Figures 7A, 7B, and S7A). Principal component (PC) analysis using the 10,000 most variable genes showed that FOLR2$^+$ macrophages isolated from mammary tumors changed their transcriptomic profile in a tumor-size dependent manner as seen by the variations in the PC2 axis (Figure 7A). Interestingly, the transcriptome of CADM1$^+$ macrophages was not influenced by the tumor size and clustered separately from FOLR2$^+$ macrophages. We found 6,139 DEG between FOLR2$^+$ and CADM1$^+$ macrophages isolated from the same tumors. We conclude that FOLR2$^+$ macrophages respond to the developing tumor but remain separable cellular entities from CADM1$^+$ macrophages. We found 1,356 DEG between mammary tumor FOLR2$^+$ macrophages and healthy MG FOLR2$^+$ macrophages. Among these DEG, mammary tumor FOLR2$^+$ macrophages expressed genes involved in the positive regulation of immune system processes including B and T cell chemoattractants (*Ccl6 to 9*, *Ccl12*, *Cxcl2*, *Cxcl13*, *Cxcl14*, and *Cxcl16*), adhesion

**Figure 6. FOLR2$^+$ macrophages are enriched in CD8$^+$ T cells infiltrated tumors and colocalize with lymphoid aggregates across cancers**

(A and B) Correlation map (A) and heatmaps (B) analyzing the association of FOLR2 and TREM2 genes to immune cell gene signatures in the METABRIC dataset (n = 1,017 patients).

(C) Differential enrichment of gene pathways analyzed in bulk RNA-seq of FOLR2$^+$ and CADM1$^+$TREM2$^+$ macrophages isolated from BC primary tumors.

(D) Representative confocal immunofluorescence images showing FOLR2$^+$ macrophages colocalizing with CD31$^+$ vessels and CD8$^+$ T cell in primary BC. Scale bars, 50 μ.

(E) Representative multiplex immunofluorescence images of tissue microarray showing CD8, FOLR2, and cytokeratin (CK) protein expression. Graph showing density of CD8$^+$ T cells in tumors with high or low FOLR2$^+$ cell density (see Figure 4E). Mann-Whitney test.

(F) Confocal images of BC tumor slices stained for FOLR2 (red), CD8 (green), and EPCAM (blue). Representative images of tumor regions with high or low density of FOLR2$^+$ macrophages. Graph of the average speed of endogenous CD8$^+$ T cells in contact or not with FOLR2$^+$ macrophages. Mann-Whitney test.

(G) Correlation map analyzing the association of FOLR2 and TREM2 genes to genes of T cell activation, cytotoxic function, or exhaustion in the METABRIC dataset (n = 1,017 patients).

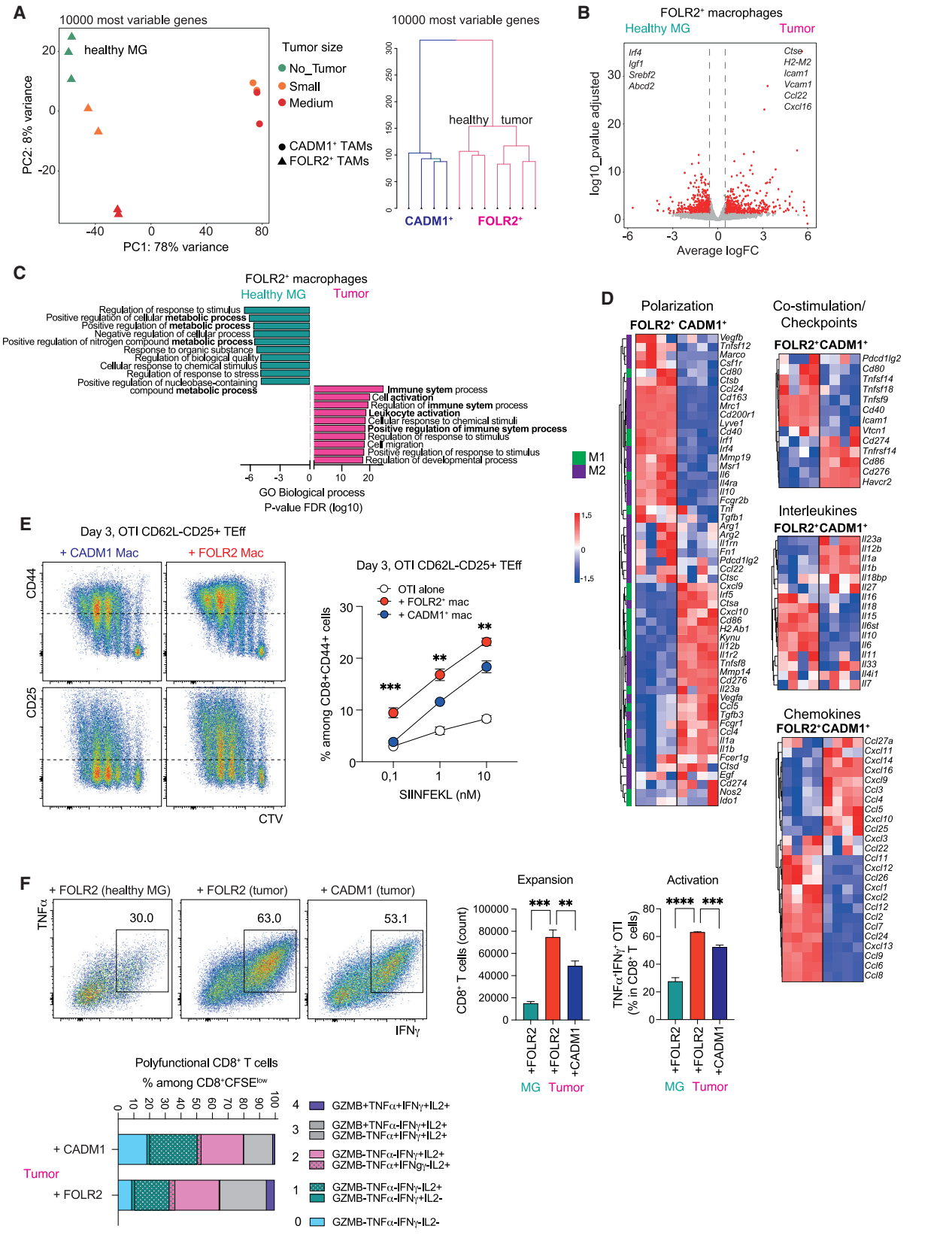


*(legend on next page)*

molecules (*Icam1*, *Vcam1*, and *Fn1*), and lysosomal proteins (*Ctse* and *Rab32*) (Figures 7B and 7C). In contrast, FOLR2$^+$ macrophages isolated from healthy MGs were enriched in genes regulating metabolic processes (*Igf1*, *Srebf2*, and *Abcd2*) (Figures 7B and 7C). Therefore, our data show that FOLR2$^+$ TRMs respond to tumor development.

Macrophage activation in tumors is often referred as "proinflammatory/M1" versus "anti-inflammatory/M2" (Mantovani et al., 2002; Murray et al., 2014). To test whether mammary tumor FOLR2$^+$ and CADM1$^+$ macrophage subsets harbor such functional specialization, we analyzed the expression of genes defining M1 or M2 gene signatures in the two macrophage subsets (Azizi et al., 2018). We found that both mammary tumor FOLR2$^+$ and CADM1$^+$ macrophages concomitantly express individual M1 and M2 genes (Figure 7D). For example, FOLR2$^+$ macrophages expressed *Cd80*, *Cd40*, and *Il6* "M1 genes" and *Cd163*, *Mrc1*, and *Il10* "M2 genes." CADM1$^+$ macrophages expressed *Cd86*, *Cxcl9*, and *Il12b* "M1 genes" and *Vegfa*, *Cd276*, and *Tgfb3* "M2 genes." This shows that macrophage activation in the tumor microenvironment does not fit with the *in vitro* M1/M2 polarization model and reveals the complexity of macrophage activation in the tumor microenvironment. Interestingly, mammary tumor FOLR2$^+$ and CADM1$^+$ macrophage subsets expressed distinct sets of functional genes that could be linked to T cell activation (Figures 7D and S7B). Therefore, to directly test the T cell-activation potential of the macrophage subsets, we set up two assays using FOLR2$^+$ and CADM1$^+$ macrophages isolated from the same tumors and cocultured with CD8$^+$ T cells. First, we set up a T cell suppression assay, in which purified TAMs were cocultured with polyclonal activated CD8$^+$ T cells. Here, FOLR2$^+$ macrophage did not display suppressive activity. Instead, FOLR2$^+$ macrophage improved CD8$^+$ T cell proliferation and differentiation (loss of CD62L and upregulation of CD44 and CD25) (Figure S7C). CADM1$^+$ macrophages did not suppress CD8$^+$ T cell activation either, but their ability to promote effector T cell differentiation was weaker than that of FOLR2$^+$ macrophages (Figure S7C). In previous studies (Ruffell et al., 2014; Katzenelenbogen et al., 2020), immunosuppressive activity was restricted to MHCII$^{NEG}$ tumor-associated myeloid cells. Instead, MHCII$^+$ TAMs were not exerting T cell inhibition. Here, we show that both CADM1$^+$ and FOLR2$^+$ TAMs express high levels of MHCII (Figure 3H) consistent with their lack of immunosuppressive activity. Since neither FOLR2$^+$ and CADM1$^+$ macrophage strongly suppressed T cell expansion, we set up an antigen-specific T cell-priming assay. Purified FOLR2$^+$ and CADM1$^+$ macrophages were loaded with the OTI-specific SIINFEKL peptide, washed, and subsequently cocultured with naive OTI CD8$^+$ T cells. In comparison to CADM1$^+$ macrophages isolated from the same tumors, FOLR2$^+$ macrophages showed higher capacity to induce the activation of naive T cells, their expansion, their polyfunctionality (IL-2, IFN-$\gamma$, and TNF-$\alpha$), and cytotoxic function (expression of granzyme B) (Figures 7E and 7F). Furthermore, we found that FOLR2$^+$ macrophages isolated from healthy MGs did not efficiently activate OTI CD8$^+$ T cells, whereas FOLR2$^+$ macrophages isolated from mammary tumors could induce T cell expansion and differentiation (Figure 7E). These results confirm that FOLR2$^+$ macrophages are activated during tumor development and acquire the ability to prime CD8$^+$ T cells. In sum, we provide evidence that FOLR2$^+$ macrophages do not behave like immunosuppressive cells. Instead, tumor-associated FOLR2$^+$ macrophages are potent antigen presenting cells displaying the functional ability to trigger CD8$^+$ T cell activation.

## DISCUSSION

We have identified an evolutionarily conserved TRM population expressing FOLR2 that is present in both human and mouse healthy MG. Human FOLR2$^+$ macrophages express MRC1 and LYVE1 and align to murine MRC1$^+$ TRMs that had been described in adult MG of healthy nulliparous mice (Jäppinen et al., 2019; Wang et al., 2020). In mice, MRC1$^+$ TRMs arise from fetal precursors as demonstrated by genetic labeling in *Csf1r*$^{Mer\text{-}iCre\text{-}Mer}$ or *Cx3cr1*$^{Cre\text{-}ERT2}$ mice (Jäppinen et al., 2019) and are locally maintained in adult mice through self-renewal (Wang et al., 2020). MRC1$^+$ TRMs coexist with a minor fraction of monocyte-derived, intraductal CX3CR1$^{high}$MRC1$^-$ TRMs expanding during tissue remodeling imposed by lactation (Dawson et al., 2020). Interestingly, most breast tumor-invading murine macrophages align transcriptionally to healthy intraductal CX3CR1$^{high}$MRC1$^-$ TRM (Dawson et al., 2020). Altogether, these findings highlight the ontogenetic and functional diversities within MG macrophage subsets. Here, we identify FOLR2$^+$ human macrophages as orthologs of murine MRC1$^+$ breast TRMs. We found that human FOLR2$^+$ macrophages represent the main macrophage population in healthy breast tissue, thereby qualifying for MG TRMs. In contrast, we show that CADM1$^+$TREM2$^+$ macrophages are scarce in healthy tissue and increase in primary tumors. We show that human CADM1$^+$TREM2$^+$ macrophages align with

**Figure 7. FOLR2$^+$ macrophages respond to tumor growth and acquire T cell-priming ability**

(A) Principal component analysis and hierarchical clustering of the 10,000 most variable genes expressed in bulk RNA-seq by FOLR2$^+$ macrophages isolated from healthy mammary glands (MG) or from small- or medium-sized tumors and in CADM1$^+$ macrophages isolated from the same tumors harvested from 22-week-old PyMT mice or age-matched littermates. Each dot of the same color corresponds to a replicate sample.

(B) Volcano plot showing DEG between FOLR2$^+$ macrophages isolated from healthy MG or mammary tumors.

(C) Differential enrichment of gene pathways between FOLR2$^+$ macrophages isolated from healthy MG or mammary tumors (bulk RNA-seq as in A).

(D) Heatmaps of selected genes between FOLR2$^+$ and CADM1$^+$ macrophages isolated from the same tumors (bulk RNA-seq as in A).

(E and F) SIINFEKL OVA peptide pulsed FOLR2$^+$ or CADM1$^+$ macrophages were cocultured with CTV labeled naive OTI CD8$^+$ T cells. (E) T cell proliferation and activation were assessed by flow cytometry after 3 days. Representative dot plots are for data obtained with macrophages pulsed with 1 nM of peptide. Data in the bar graph are mean ± SD of triplicate wells and representative of 3 experiments. Unpaired t test. (F) Intracellular expression of GZMB, TNF-$\alpha$, IL-2, and IFN-$\gamma$ measured by flow cytometry. Representative dot plots are for data obtained with macrophages pulsed with 1 nM of peptide. Data in the lower panel bar graph are mean ± SD of triplicate wells and represent Boolean analysis of the T cell populations. Unpaired t test. Data in the right panel represent OTI T cell counts and % of IFN-$\gamma^+$TNF-$\alpha^+$ CD8$^+$ T cells after 3 days coculture with the distinct macrophage populations pulsed with 1 nM of SIINFEKL. Data are mean ± SD of triplicate wells and representative of 2 experiments. Unpaired t test.

murine monocyte-derived CX3CR1$^{high}$MRC1$^{-}$ TAMs. Our bulk RNA-seq analysis of human CADM1$^{+}$TREM2$^{+}$ macrophages demonstrate their transcriptional closeness to CCR2$^{+}$ monocytes further suggesting a monocytic origin. CADM1$^{+}$TREM2$^{+}$ macrophages are likely to align to TREM2$^{+}$ macrophages recently identified in multiple cancer types (Molgora et al., 2020).

Recent studies have highlighted protumorigenic roles for murine TRMs. For instance, depletion of embryonic-derived TRMs delays the progression of tumor lesions in pancreatic cancer (Zhu et al., 2017). However, the impact on overall survival has not been assessed. Also, depletion of CD163$^{+}$ TRMs in ovarian cancer reduces epithelial to mesenchymal transition and overall tumor growth (Etzerodt et al., 2020). CD169$^{+}$ alveolar macrophages promote epithelial to mesenchymal transition of lung cancer cells *in vitro* (Casanova-Acebes et al., 2021). In murine PyMT BC, MHCII$^{+}$CD11b$^{+}$MRC1$^{+}$ TRMs present in healthy MGs persist in developing breast tumors despite dilution by incoming monocyte-derived TAMs (Franklin et al., 2014). TRM depletion *in vivo* prior to carcinogenesis did not affect T cell activation nor tumor growth in autochthonous BC models (Franklin et al., 2014; Linde et al., 2018) but increased early cancer cell dissemination (Linde et al., 2018). FOLR2$^{+}$ macrophages resemble MRC1$^{+}$ TRMs described by Franklin et al. (2014). We did not evidence any T cell inhibitory activity by FOLR2$^{+}$ macrophages. Instead, we show that FOLR2$^{+}$ TRMs acquire the ability to prime naive CD8$^{+}$ T cells into polyfunctional effectors (Granzyme B$^{+}$, IFN-$\gamma^{+}$, TNF-$\alpha^{+}$) upon activation associated to tumor development.

FOLR2$^{+}$ macrophages present a transcriptional signature of steady-state PV macrophages (*LYVE1*, *MRC1*, and *TIMD4*). Accordingly, we found that some FOLR2$^{+}$ macrophages were located in close proximity to CD31$^{+}$ vessels in human tissues. In mice, various studies have identified PV macrophages across organs (Chakarov et al., 2019; Goldmann et al., 2016; Lim et al., 2018; Mebius and Kraal, 2005; Utz et al., 2020). In mouse models, a protumoral subset of PV macrophages expressing the angiopoietin receptor TIE2 has been implicated in angiogenesis and tumor spreading (De Palma et al., 2005; Lewis et al., 2016). However, we do not favor the hypothesis according to which FOLR2$^{+}$ macrophages correspond to TIE2$^{+}$ macrophages for two reasons: (1) we did not find TIE2 expression in FOLR2$^{+}$ macrophages and (2) TIE2$^{+}$ PV macrophages differentiate from inflammatory proangiogenic TIE2$^{+}$ monocytes (Coffelt et al., 2010; Arwert et al., 2018).

A recent study has identified a subset of potentially immunosuppressive FOLR2$^{+}$ TAMs associated to human hepatocellular carcinoma (Sharma et al., 2020). To probe the function of FOLR2$^{+}$ macrophages in large BC datasets, we designed a gene signature that enabled us to infer FOLR2$^{+}$ macrophages abundance in BC bulk transcriptomes. We found that the abundance of FOLR2$^{+}$ TAMs associated with better prognosis in patients with BC. We provide a validation of this finding by showing that the cellular density of FOLR2$^{+}$ macrophages assessed by immunofluorescence positively correlates with increased BC patient survival. We next found that FOLR2$^{+}$—but not TREM2$^{+}$—macrophage abundance positively correlates with tumor-infiltrating CD8$^{+}$ T cell, B cells, and DCs. In addition, we found by confocal imaging that FOLR2$^{+}$ macrophages colocalized with CD8$^{+}$ T cell aggregates in the vicinity of endothelial cells. We validated the correlation between FOLR2$^{+}$ macrophage and CD8$^{+}$ T cell abundance by multispectral imaging: tumor lesions highly infiltrated with FOLR2$^{+}$ TAMs display significantly higher CD8$^{+}$ T cell density. Using live imaging on fresh human tumor sections, we showed that tumor-infiltrating CD8$^{+}$ T cells engage in long-lasting interactions with FOLR2$^{+}$ TAMs. Since CD8$^{+}$ T cell infiltration correlates with better survival probability in many cancers including BC, these results suggest that FOLR2$^{+}$ TAMs participate to the onset of antitumor immunity. Further studies are needed to identify the mechanisms by which FOLR2$^{+}$ TAMs regulate lymphocyte infiltration in tumors, a key event for the development of efficient antitumor immune responses.

### Limitations of the study

Tools enabling the *in vivo* specific deletion of FOLR2$^{+}$ TAMs, without impacting other monocyte/macrophage subsets are required to address the specific contribution of FOLR2$^{+}$ TAMs to tumor immunity. In addition, extension of the findings of this study beyond BC needs further thorough characterization of FOLR2$^{+}$ TAMs in other cancer types. We found that patients with luminal BC receiving endocrine therapy alone and presenting high FOLR2 gene-signature score have a significantly improved survival. Moreover, we showed that the FOLR2 gene signature is a significant prognostic factor when adjusted by several reported prognostic features of BC. Further studies are required to thoroughly benchmark the FOLR2 gene signature against other available stratification methods and to address its utility in specific, clinically relevant patient subgroups. Given the pronounced correlation with CD8$^{+}$ T cells and the well-established prognostic power of tumor-infiltrating lymphocytes and cytotoxic cells in BC, future studies should aim to distinguish whether FOLR2$^{+}$ TAMs hold independent prognostic power from CD8$^{+}$ T cells.

## STAR★METHODS

Detailed methods are provided in the online version of this paper and include the following:

- KEY RESOURCES TABLE
- RESOURCE AVAILABILITY
  - Lead contact
  - Materials availability
  - Data and code availability
- EXPERIMENTAL MODEL AND SUBJECT DETAILS
  - Human specimens
  - Cell lines
  - Mice
- METHOD DETAILS
  - Human samples processing
  - Mouse tumor orthotopic transplantation
  - Mouse tissues processing
  - Murine and human macrophage FACS sorting
  - Mouse T cell suppression assay
  - Mouse T cell priming assay
  - Mass cytometry staining
  - Human and mouse sample processing for single cell RNA-sequencing

- Single-cell RNA-sequencing
- Bulk RNA-sequencing
- Immunohistochemistry
- Immunofluorescence on fixed tumor slices
- Tumor slice imaging

- QUANTIFICATION AND STATISTICAL ANALYSIS
  - Flow cytometry analysis
  - CyTOF data analysis
  - Single-cell RNA-sequencing data processing and analysis
  - Human-mouse merging and seurat label transfer prediction score
  - Processing of published dataset
  - Bulk RNA-sequencing data processing and analysis
  - Dynamic imaging analysis
  - Multispectral immunofluorescence on paraffin-embedded tissues and tissue microarrays
  - METABRIC data analysis
  - CPTAC data analysis
  - Additional dataset analyses
  - TCGA data analysis
  - GTEx to TCGA comparison
  - Statistical analysis

## SUPPLEMENTAL INFORMATION

Supplemental information can be found online at https://doi.org/10.1016/j.cell.2022.02.021.

## ACKNOWLEDGMENTS

We thank A.M. Lennon-Dumenil, J. Waterfall, C. Thery, P. Sirven, and F. Benvenuti for helpful advice and reagents. E.P. team is supported by the SiRIC-Curie Program (grant INCa-DGOS-12554), the Labex DCBIOL (ANR-10-IDEX-0001-02 PSL and ANR-11-LABX-0043), the Fondation ARC (PA20181207706), the Ligue Nationale contre le cancer (RS19/75-92), and the Center of Clinical Investigation (CIC IGR-Curie 1428). High-throughput sequencing was performed by the ICGex NGS platform of the Institut Curie supported by the grants ANR-10-EQPX-03 and ANR-10-INBS-09-08, by the ITMO-Cancer Aviesan (Plan Cancer III), and by the SiRIC-Curie program (SiRIC Grant INCa-DGOS-4654). C.P.B. and S.Z. are supported by the NIHR Manchester BRC and by a Cancer Research UK Manchester Institute Award (A19258). W.V. is supported by the grant IG23179, A.I.R.C. P.G. is supported by IDEX (ANR-18-IDEX-0001), INCA (PL-BIO-ICR1), and ANR-17-CE11-0001-01.

## AUTHOR CONTRIBUTIONS

Conceptualization, R.N.R., E.P., and J.H.; methodology, R.N.R., Y.M.-K., Y.G.-F., and J.H.; formal analysis, W.R., Y.M.-K., C.P.B., and J.H.; investigation, R.N.R., Y.M.-K., Y.G.-F., N.G.N., J.T.B., C.P.B., M.B., J.D., P.C., F.K., L.L.N., C.-A.D., F.G., L.V., E.D., B.B., J.G., S.Z., W.V., L.M., and J.H.; resources, S.B., S.L., M.B., C.S., S.V., L.L., A.N., D.M., A.V.-S., and F.R.; writing – original draft, J.H.; writing—review & editing, J.H., P.G., S.Z., E.P., R.N.R., and E.D.; visualization, J.H., R.N.R., and Y.M.-K.; supervision, J.H.; funding acquisition, J.H. and E.P.

## DECLARATION OF INTERESTS

The authors J.H., R.N.R., E.P., and P.G. and their institutions have filed a patent related to this work.

Received: November 16, 2020
Revised: October 8, 2021
Accepted: February 15, 2022
Published: April 23, 2022

## REFERENCES

Ali, H.R., Chlon, L., Pharoah, P.D.P., Markowetz, F., and Caldas, C. (2016). Patterns of immune infiltration in breast cancer and their clinical implications: a gene-expression-based retrospective study. PLoS Med. *13*, e1002194.

Ali, H.R., Provenzano, E., Dawson, S.J., Blows, F.M., Liu, B., Shah, M., Earl, H.M., Poole, C.J., Hiller, L., Dunn, J.A., et al. (2014). Association between CD8$^+$ T-cell infiltration and breast cancer survival in 12,439 patients. Ann. Oncol. *25*, 1536–1543.

Anders, S., and Huber, W. (2010). Differential expression analysis for sequence count data. Genome Biol. *11*, R106.

Arwert, E.N., Harney, A.S., Entenberg, D., Wang, Y., Sahai, E., Pollard, J.W., and Condeelis, J.S. (2018). A unidirectional transition from migratory to perivascular macrophage is required for tumor cell intravasation. Cell Rep. *23*, 1239–1248.

Azizi, E., Carr, A.J., Plitas, G., Cornish, A.E., Konopacki, C., Prabhakaran, S., Nainys, J., Wu, K., Kiseliovas, V., Setty, M., et al. (2018). Single-cell map of diverse immune phenotypes in the breast tumor microenvironment. Cell *174*, 1293–1308.e36.

Becher, B., Schlitzer, A., Chen, J., Mair, F., Sumatoh, H.R., Teng, K.W.W., Low, D., Ruedl, C., Riccardi-Castagnoli, P., Poidinger, M., et al. (2014). High-dimensional analysis of the murine myeloid cell system. Nat. Immunol. *15*, 1181–1189.

Becht, E., Giraldo, N.A., Lacroix, L., Buttard, B., Elarouci, N., Petitprez, F., Selves, J., Laurent-Puig, P., Sautès-Fridman, C., Fridman, W.H., and de Reyniès, A. (2016). Estimating the population abundance of tissue-infiltrating immune and stromal cell populations using gene expression. Genome Biol. *17*, 218.

Bindea, G., Mlecnik, B., Hackl, H., Charoentong, P., Tosolini, M., Kirilovsky, A., Fridman, W.H., Pagès, F., Trajanoski, Z., and Galon, J. (2009). ClueGO: a cytoscape plug-in to decipher functionally grouped gene ontology and pathway annotation networks. Bioinformatics *25*, 1091–1093.

Bonapace, L., Coissieux, M.M., Wyckoff, J., Mertz, K.D., Varga, Z., Junt, T., and Bentires-Alj, M. (2014). Cessation of CCL2 inhibition accelerates breast cancer metastasis by promoting angiogenesis. Nature *515*, 130–133.

Bourdely, P., Anselmi, G., Vaivode, K., Ramos, R.N., Missolo-Koussou, Y., Hidalgo, S., Tosselo, J., Nuñez, N., Richer, W., Vincent-Salomon, A., et al. (2020). Transcriptional and functional analysis of CD1c$^+$ human dendritic cells identifies a CD163$^+$ subset priming CD8$^+$CD103$^+$ T cells. Immunity *53*, 335–352.e8.

Brummelman, J., Haftmann, C., Núñez, N.G., Alvisi, G., Mazza, E.M.C., Becher, B., and Lugli, E. (2019). Development, application and computational analysis of high-dimensional fluorescent antibody panels for single-cell flow cytometry. Nat. Protoc. *14*, 1946–1969.

Butler, A., Hoffman, P., Smibert, P., Papalexi, E., and Satija, R. (2018). Integrating single-cell transcriptomic data across different conditions, technologies, and species. Nat. Biotechnol. *36*, 411–420.

Casanova-Acebes, M., Dalla, E., Leader, A.M., LeBerichel, J., Nikolic, J., Morales, B.M., Brown, M., Chang, C., Troncoso, L., Chen, S.T., et al. (2021). Tissue-resident macrophages provide a pro-tumorigenic niche to early NSCLC cells. Nature *595*, 578–584.

Cassetta, L., Fragkogianni, S., Sims, A.H., Swierczak, A., Forrester, L.M., Zhang, H., Soong, D.Y.H., Cotechini, T., Anur, P., Lin, E.Y., et al. (2019). Human tumor-associated macrophage and monocyte transcriptional landscapes reveal cancer-specific reprogramming, biomarkers, and therapeutic targets. Cancer Cell *35*, 588–602.e10.

Cassetta, L., and Pollard, J.W. (2018). Targeting macrophages: therapeutic approaches in cancer. Nat. Rev. Drug Discov. *17*, 887–904.

Chakarov, S., Lim, H.Y., Tan, L., Lim, S.Y., See, P., Lum, J., Zhang, X.M., Foo, S., Nakamizo, S., Duan, K., et al. (2019). Two distinct interstitial macrophage

populations coexist across tissues in specific subtissular niches. Science *363*, eaau0964.

Chen, X., Li, J., Gray, W.H., Lehmann, B.D., Bauer, J.A., Shyr, Y., and Pietenpol, J.A. (2012). TNBCtype: a subtyping tool for triple-negative breast cancer. Cancer Inform. *11*, 147–156.

Chow, A., Schad, S., Green, M.D., Hellmann, M.D., Allaj, V., Ceglia, N., Zago, G., Shah, N.S., Sharma, S.K., Mattar, M., et al. (2021). Tim-4$^{+}$ cavity-resident macrophages impair anti-tumor CD8$^{+}$ T cell immunity. Cancer Cell *39*, 973–988.e9.

Coffelt, S.B., Tal, A.O., Scholz, A., De Palma, M., Patel, S., Urbich, C., Biswas, S.K., Murdoch, C., Plate, K.H., Reiss, Y., and Lewis, C.E. (2010). Angiopoietin-2 regulates gene expression in TIE2-expressing monocytes and augments their inherent proangiogenic functions. Cancer Res. *70*, 5270–5280.

Colonna, M., Trinchieri, G., and Liu, Y.J. (2004). Plasmacytoid dendritic cells in immunity. Nat. Immunol. *5*, 1219–1226.

Curtis, C., Shah, S.P., Chin, S.F., Turashvili, G., Rueda, O.M., Dunning, M.J., Speed, D., Lynch, A.G., Samarajiwa, S., Yuan, Y., et al. (2012). The genomic and transcriptomic architecture of 2,000 breast tumours reveals novel subgroups. Nature *486*, 346–352.

Davie, S.A., Maglione, J.E., Manner, C.K., Young, D., Cardiff, R.D., MacLeod, C.L., and Ellies, L.G. (2007). Effects of FVB/NJ and C57BL/6J strain backgrounds on mammary tumor phenotype in inducible nitric oxide synthase deficient mice. Transgen. Res. *16*, 193–201.

Dawson, C.A., Pal, B., Vaillant, F., Gandolfo, L.C., Liu, Z., Bleriot, C., Ginhoux, F., Smyth, G.K., Lindeman, G.J., Mueller, S.N., et al. (2020). Tissue-resident ductal macrophages survey the mammary epithelium and facilitate tissue remodelling. Nat. Cell Biol. *22*, 546–558.

De Palma, M., Venneri, M.A., Galli, R., Sergi Sergi, L., Politi, L.S., Sampaolesi, M., and Naldini, L. (2005). Tie2 identifies a hematopoietic lineage of proangiogenic monocytes required for tumor vessel formation and a mesenchymal population of pericyte progenitors. Cancer Cell *8*, 211–226.

DeNardo, D.G., Brennan, D.J., Rexhepaj, E., Ruffell, B., Shiao, S.L., Madden, S.F., Gallagher, W.M., Wadhwani, N., Keil, S.D., Junaid, S.A., et al. (2011). Leukocyte complexity predicts breast cancer survival and functionally regulates response to chemotherapy. Cancer Discov. *1*, 54–67.

Dobin, A., Davis, C.A., Schlesinger, F., Drenkow, J., Zaleski, C., Jha, S., Batut, P., Chaisson, M., and Gingeras, T.R. (2013). STAR: ultrafast universal RNA-seq aligner. Bioinformatics *29*, 15–21.

Dutertre, C.A., Becht, E., Irac, S.E., Khalilnezhad, A., Narang, V., Khalilnezhad, S., Ng, P.Y., van den Hoogen, L.L., Leong, J.Y., Lee, B., et al. (2019). Single-cell analysis of human mononuclear phagocytes reveals subset-defining markers and identifies circulating inflammatory dendritic cells. Immunity *51*, 573–589.e8.

Engblom, C., Pfirschke, C., and Pittet, M.J. (2016). The role of myeloid cells in cancer therapies. Nat. Rev. Cancer *16*, 447–462.

Etzerodt, A., Moulin, M., Doktor, T.K., Delfini, M., Mossadegh-Keller, N., Bajenoff, M., Sieweke, M.H., Moestrup, S.K., Auphan-Anezin, N., and Lawrence, T. (2020). Tissue-resident macrophages in omentum promote metastatic spread of ovarian cancer. J. Exp. Med. *217*, e20191869.

Finak, G., Bertos, N., Pepin, F., Sadekova, S., Souleimanova, M., Zhao, H., Chen, H., Omeroglu, G., Meterissian, S., Omeroglu, A., et al. (2008). Stromal gene expression predicts clinical outcome in breast cancer. Nat. Med. *14*, 518–527.

Finck, R., Simonds, E.F., Jager, A., Krishnaswamy, S., Sachs, K., Fantl, W., Pe'er, D., Nolan, G.P., and Bendall, S.C. (2013). Normalization of mass cytometry data with bead standards. Cytometry A *83*, 483–494.

Franklin, R.A., Liao, W., Sarkar, A., Kim, M.V., Bivona, M.R., Liu, K., Pamer, E.G., and Li, M.O. (2014). The cellular and molecular origin of tumor-associated macrophages. Science *344*, 921–925.

Gallina, G., Dolcetti, L., Serafini, P., De Santo, C.D., Marigo, I., Colombo, M.P., Basso, G., Brombacher, F., Borrello, I., Zanovello, P., et al. (2006). Tumors induce a subset of inflammatory monocytes with immunosuppressive activity on CD8$^{+}$ T cells. J. Clin. Invest. *116*, 2777–2790.

Gendoo, D.M.A., Ratanasirigulchai, N., Schröder, M.S., Paré, L., Parker, J.S., Prat, A., and Haibe-Kains, B. (2016). Genefu: an R/Bioconductor package for computation of gene expression-based signatures in breast cancer. Bioinformatics *32*, 1097–1099.

Goldmann, T., Wieghofer, P., Jordão, M.J.C., Prutek, F., Hagemeyer, N., Frenzel, K., Amann, L., Staszewski, O., Kierdorf, K., Krueger, M., et al. (2016). Origin, fate and dynamics of macrophages at central nervous system interfaces. Nat. Immunol. *17*, 797–805.

Gu, Z., Eils, R., and Schlesner, M. (2016). Complex heatmaps reveal patterns and correlations in multidimensional genomic data. Bioinformatics *32*, 2847–2849.

Guilliams, M., and Scott, C.L. (2017). Does niche competition determine the origin of tissue-resident macrophages? Nat. Rev. Immunol. *17*, 451–460.

Han, X., Wang, R., Zhou, Y., Fei, L., Sun, H., Lai, S., Saadatpour, A., Zhou, Z., Chen, H., Ye, F., et al. (2018). Mapping the mouse cell atlas by microwell-seq. Cell *172*, 1091–1107.e17.

Hanna, R.N., Cekic, C., Sag, D., Tacke, R., Thomas, G.D., Nowyhed, H., Herrley, E., Rasquinha, N., McArdle, S., Wu, R., et al. (2015). Patrolling monocytes control tumor metastasis to the lung. Science *350*, 985–990.

Hugues, S., Fetler, L., Bonifaz, L., Helft, J., Amblard, F., and Amigorena, S. (2004). Distinct T cell dynamics in lymph nodes during the induction of tolerance and immunity. Nat. Immunol. *5*, 1235–1242.

Jäppinen, N., Félix, I., Lokka, E., Tyystjärvi, S., Pynttäri, A., Lahtela, T., Gerke, H., Elima, K., Rantakari, P., and Salmi, M. (2019). Fetal-derived macrophages dominate in adult mammary glands. Nat. Commun. *10*, 281.

Katzenelenbogen, Y., Sheban, F., Yalin, A., Yofe, I., Svetlichnyy, D., Jaitin, D.A., Bornstein, C., Moshe, A., Keren-Shaul, H., Cohen, M., et al. (2020). Coupled scRNA-seq and intracellular protein activity reveal an immunosuppressive role of TREM2 in Cancer. Cell *182*, 872–885.e19.

Leek, R.D., Lewis, C.E., Whitehouse, R., Greenall, M., Clarke, J., and Harris, A.L. (1996). Association of macrophage infiltration with angiogenesis and prognosis in invasive breast carcinoma. Cancer Res. *56*, 4625–4629.

Lewis, C.E., Harney, A.S., and Pollard, J.W. (2016). The multifaceted role of perivascular macrophages in tumors. Cancer Cell *30*, 18–25.

Lewis, C.E., and Pollard, J.W. (2006). Distinct role of macrophages in different tumor microenvironments. Cancer Res. *66*, 605–612.

Li, T., Fan, J., Wang, B., Traugh, N., Chen, Q., Liu, J.S., Li, B., and Liu, X.S. (2017). TIMER: a web server for comprehensive analysis of tumor-infiltrating immune cells. Cancer Res. *77*, e108–e110.

Lim, H.Y., Lim, S.Y., Tan, C.K., Thiam, C.H., Goh, C.C., Carbajo, D., Chew, S.H.S., See, P., Chakarov, S., Wang, X.N., et al. (2018). Hyaluronan receptor LYVE-1-Expressing macrophages maintain arterial tone through hyaluronan-mediated regulation of smooth muscle cell collagen. Immunity *49*, 326–341.e7.

Lin, E.Y., Jones, J.G., Li, P., Zhu, L., Whitney, K.D., Muller, W.J., and Pollard, J.W. (2003). Progression to malignancy in the polyoma middle T oncoprotein mouse breast cancer model provides a reliable model for human diseases. Am. J. Pathol. *163*, 2113–2126.

Lin, E.Y., Li, J.F., Gnatovskiy, L., Deng, Y., Zhu, L., Grzesik, D.A., Qian, H., Xue, X.N., and Pollard, J.W. (2006). Macrophages regulate the angiogenic switch in a mouse model of breast cancer. Cancer Res. *66*, 11238–11246.

Linde, N., Casanova-Acebes, M., Sosa, M.S., Mortha, A., Rahman, A., Farias, E., Harper, K., Tardio, E., Reyes Torres, I., Jones, J., et al. (2018). Macrophages orchestrate breast cancer early dissemination and metastasis. Nat. Commun. *9*, 21.

Love, M.I., Huber, W., and Anders, S. (2014). Moderated estimation of fold change and dispersion for RNA-seq data with DESeq2. Genome Biol. *15*, 550.

Loyher, P.-L., Hamon, P., Laviron, M., Meghraoui-Kheddar, A., Goncalves, E., Deng, Z., Torstensson, S., Bercovici, N., Baudesson de Chanville, C., Combadière, B., et al. (2018). Macrophages of distinct origins contribute to tumor development in the lung. The J. Exp. Med. *215*, 2536–2553.

Mantovani, A., Marchesi, F., Malesci, A., Laghi, L., and Allavena, P. (2017). Tumour-associated macrophages as treatment targets in oncology. Nat. Rev. Clin. Oncol. *14*, 399–416.

Mantovani, A., Sica, A., Sozzani, S., Allavena, P., Vecchi, A., and Locati, M. (2004). The chemokine system in diverse forms of macrophage activation and polarization. Trends Immunol. *25*, 677–686.

Mantovani, A., Sozzani, S., Locati, M., Allavena, P., and Sica, A. (2002). Macrophage polarization: tumor-associated macrophages as a paradigm for polarized M2 mononuclear phagocytes. Trends Immunol. *23*, 549–555.

Mebius, R.E., and Kraal, G. (2005). Structure and function of the spleen. Nat. Rev. Immunol. *5*, 606–616.

Mempel, T.R., Henrickson, S.E., and Von Andrian, U.H. (2004). T-cell priming by dendritic cells in lymph nodes occurs in three distinct phases. Nature *427*, 154–159.

Molgora, M., Esaulova, E., Vermi, W., Hou, J., Chen, Y., Luo, J., Brioschi, S., Bugatti, M., Omodei, A.S., Ricci, B., et al. (2020). TREM2 modulation remodels the tumor myeloid landscape enhancing anti-PD-1 immunotherapy. Cell *182*, 886–900.e17.

Murray, P.J., Allen, J.E., Biswas, S.K., Fisher, E.A., Gilroy, D.W., Goerdt, S., Gordon, S., Hamilton, J.A., Ivashkiv, L.B., Lawrence, T., et al. (2014). Macrophage activation and polarization: nomenclature and experimental guidelines. Immunity *41*, 14–20.

Newell, E.W., Sigal, N., Bendall, S.C., Nolan, G.P., and Davis, M.M. (2012). Cytometry by time-of-flight shows combinatorial cytokine expression and virus-specific cell niches within a continuum of CD8$^+$ T cell phenotypes. Immunity *36*, 142–152.

Núñez, N.G., Tosello Boari, J., Ramos, R.N., Richer, W., Cagnard, N., Anderfuhren, C.D., Niborski, L.L., Bigot, J., Meseure, D., De La Rochere, P., et al. (2020). Tumor invasion in draining lymph nodes is associated with Treg accumulation in breast cancer patients. Nat. Commun. *11*, 3272.

Pagès, F., Mlecnik, B., Marliot, F., Bindea, G., Ou, F.S., Bifulco, C., Lugli, A., Zlobec, I., Rau, T.T., Berger, M.D., et al. (2018). International validation of the consensus Immunoscore for the classification of colon cancer: a prognostic and accuracy study. Lancet *391*, 2128–2139.

Peranzoni, E., Lemoine, J., Vimeux, L., Feuillet, V., Barrin, S., Kantari-Mimoun, C., Bercovici, N., Guérin, M., Biton, J., Ouakrim, H., et al. (2018). Macrophages impede CD8 T cells from reaching tumor cells and limit the efficacy of anti-PD-1 treatment. Proc. Natl. Acad. Sci. USA *115*, E4041–E4050.

Qian, B.Z., Li, J., Zhang, H., Kitamura, T., Zhang, J., Campion, L.R., Kaiser, E.A., Snyder, L.A., and Pollard, J.W. (2011). CCL2 recruits inflammatory monocytes to facilitate breast-tumour metastasis. Nature *475*, 222–225.

Ramos, R.N., Rodriguez, C., Hubert, M., Ardin, M., Treilleux, I., Ries, C.H., Lavergne, E., Chabaud, S., Colombe, A., Trédan, O., et al. (2020). CD163$^+$ tumor-associated macrophage accumulation in breast cancer patients reflects both local differentiation signals and systemic skewing of monocytes. Clin. Transl. Immunology *9*, e1108.

Ries, C.H., Cannarile, M.A., Hoves, S., Benz, J., Wartha, K., Runza, V., Rey-Giraud, F., Pradel, L.P., Feuerhake, F., Klaman, I., et al. (2014). Targeting tumor-associated macrophages with anti-CSF-1R antibody reveals a strategy for cancer therapy. Cancer Cell *25*, 846–859.

Ruffell, B., Au, A., Rugo, H.S., Esserman, L.J., Hwang, E.S., and Coussens, L.M. (2012). Leukocyte composition of human breast cancer. Proc. Natl. Acad. Sci. USA *109*, 2796–2801.

Ruffell, B., Chang-Strachan, D., Chan, V., Rosenbusch, A., Ho, C.M.T., Pryer, N., Daniel, D., Hwang, E.S., Rugo, H.S., and Coussens, L.M. (2014). Macrophage IL-10 blocks CD8$^+$ T cell-dependent responses to chemotherapy by suppressing IL-12 expression in intratumoral dendritic cells. Cancer Cell *26*, 623–637.

Ruffell, B., and Coussens, L.M. (2015). Macrophages and therapeutic resistance in cancer. Cancer Cell *27*, 462–472.

Samaniego, R., Palacios, B.S., Domiguez-Soto, Á., Vidal, C., Salas, A., Matsuyama, T., Sánchez-Torres, C., Torre, I. de la, Miranda-Carús, M.E., Sánchez-Mateos, P., et al. (2014). Macrophage uptake and accumulation of folates are polarization-dependent *in vitro* and *in vivo* and are regulated by activin A. J. Leukoc. Biol. *95*, 797–808.

Sharma, A., Seow, J.J.W., Dutertre, C.-A., Pai, R., Blériot, C., Mishra, A., Wong, R.M.M., Singh, G.S.N., Sudhagar, S., Khalilnezhad, S., et al. (2020). Onco-fetal reprogramming of endothelial cells drives immunosuppressive macrophages in hepatocellular carcinoma. Cell *183*, 377–394.e21.

Stuart, T., Butler, A., Hoffman, P., Hafemeister, C., Papalexi, E., Mauck, W.M., Hao, Y., Stoeckius, M., Smibert, P., and Satija, R. (2019). Comprehensive integration of single-cell data. Cell *177*, 1888–1902.e21.

Thomas, J.R., Appios, A., Zhao, X., Dutkiewicz, R., Donde, M., Lee, C.Y.C., Naidu, P., Lee, C., Cerveira, J., Liu, B., et al. (2021). Phenotypic and functional characterization of first-trimester human placental macrophages, Hofbauer cells. J. Exp. Med. *218*, e20200891.

Thorsson, V., Gibbs, D.L., Brown, S.D., Wolf, D., Bortone, D.S., Ou Yang, T.-H., Porta-Pardo, E., Gao, G.F., Plaisier, C.L., Eddy, J.A., et al. (2018). The immune landscape of cancer. Immunity *48*, 812–830.e14.

Utz, S.G., See, P., Mildenberger, W., Thion, M.S., Silvin, A., Lutz, M., Ingelfinger, F., Rayan, N.A., Lelios, I., Buttgereit, A., et al. (2020). Early fate defines microglia and non-parenchymal brain macrophage development. Cell *181*, 557–573.e18.

Van Gassen, S., Callebaut, B., Van Helden, M.J., Lambrecht, B.N., Demeester, P., Dhaene, T., and Saeys, Y. (2015). FlowSOM: using self-organizing maps for visualization and interpretation of cytometry data. Cytometry A *87*, 636–645.

Villani, A.C., Satija, R., Reynolds, G., Sarkizova, S., Shekhar, K., Fletcher, J., Griesbeck, M., Butler, A., Zheng, S., Lazo, S., et al. (2017). Single-cell RNA-seq reveals new types of human blood dendritic cells, monocytes, and progenitors. Science *356*, eaah4573.

Wang, Y., Chaffee, T.S., LaRue, R.S., Huggins, D.N., Witschen, P.M., Ibrahim, A.M., Nelson, A.C., Machado, H.L., and Schwertfeger, K.L. (2020). Tissue-resident macrophages promote extracellular matrix homeostasis in the mammary gland stroma of nulliparous mice. Elife *9*, e57438.

Wang, Y., Klijn, J.G.M., Zhang, Y., Sieuwerts, A.M., Look, M.P., Yang, F., Talantov, D., Timmermans, M., Meijer-van Gelder, M.E., Yu, J., et al. (2005a). Gene-expression profiles to predict distant metastasis of lymph-node-negative primary breast cancer. Lancet *365*, 671–679.

Wang, Y., Klijn, J.G.M., Zhang, Y., Sieuwerts, A.M., Look, M.P., Yang, F., Talantov, D., Timmermans, M., Meijer-van Gelder, M.E., Yu, J., et al. (2005b). Gene-expression profiles to predict distant metastasis of lymph-node-negative primary breast cancer. Lancet *365*, 671–679.

Yu, G., and He, Q.Y. (2016). ReactomePA: an R/Bioconductor package for reactome pathway analysis and visualization. Mol. Biosyst. *12*, 477–479.

Yuan, Z.-Y., Luo, R.-Z., Peng, R.-J., Wang, S.-S., and Xue, C. (2014). High Infiltration of Tumor-Associated Macrophages in Triple-Negative Breast Cancer is Associated with a Higher Risk of Distant Metastasis (Dove Press).

Zhao, X., Qu, J., Sun, Y., Wang, J., Liu, X., Wang, F., Zhang, H., Wang, W., Ma, X., Gao, X., Zhang, S., et al. (2017). Prognostic significance of tumor-associated macrophages in breast cancer: a meta-analysis of the literature. Oncotarget *8*, 30576–30586.

Zhu, Y., Herndon, J.M., Sojka, D.K., Kim, K.-W., Knolhoff, B.L., Zuo, C., Cullinan, D.R., Luo, J., Bearden, A.R., Lavine, K.J., et al. (2017). Tissue-resident macrophages in pancreatic ductal adenocarcinoma originate from embryonic hematopoiesis and promote tumor progression. Immunity *47*, 323–338.e6.

## STAR★METHODS

### KEY RESOURCES TABLE

| REAGENT or RESOURCE | SOURCE | IDENTIFIER |
|---|---|---|
| Antibodies | | |
| anti-human CD3 (clone OKT3) | Dako | Cat#A0452; RRID:AB_2335677 |
| anti-human APOE (clone EP1374Y) | Abcam | Cat#ab52607; RRID:AB_867704 |
| anti-human CD11c (clone 2F1C10) | Protein tech | Cat#60258; RRID:AB_2883128 |
| anti-human AE1/AE3 (Cytokeratin) (clone AE1/AE3) | Dako | Cat#GA05361-2; RRID:AB_2892089 |
| anti-human AE1/AE3 (Cytokeratin) (clone AE1/AE3) | Abcam | Cat#ab86734; RRID:AB_10674321 |
| anti-human LYVE-1 (clone 8C) | Merck-Millipore | Cat# MABS1929 |
| anti-human CD31 (clone JC70A) | Dako | Cat#GA610; RRID:AB_2892053 |
| anti-human CD8 (clone C8/114B) | Dako | Cat#GA623; RRID: AB_2892113 |
| anti-human FOLR2 (clone OTI4G6) | Thermo Fischer Scientific | Cat#MA5-26933; RRID:AB_2723188 |
| PE anti-human CD206 (clone 19.2) | BD Biosciences | Cat#555954; RRID:AB_396250 |
| PerCP/Cy5.5 anti-human CD8 (clone SK1) | BD Biosciences | Cat#565310; RRID:AB_2687497 |
| Alexa Fluor 488 anti-human CD31 (clone WM59) | Biolegend | Cat#303109; RRID:AB_493075 |
| Brilliant Violet 421 anti-human EpCAM (CD326) (clone 9C4) | Biolegend | Cat#324219; RRID: AB_11124342 |
| eFluor660 anti-human EpCAM (CD326) (clone 1B7) | eBioscience | Cat#50-9326-42; RRID:AB_10598658 |
| PE anti-human FOLR2 (clone 94/FOLR2) | Biolegend | Cat#391703; RRID:AB_2721335 |
| APC anti-human FOLR2 (clone 94/FOLR2) | Biolegend | Cat#391705; RRID:AB_2721302 |
| BUV395 anti-human Pan carcinoma (clone KS1/4) | BD Biosciences | Cat#745704; RRID:AB_2743186 |
| APC-Cy7 anti-human CD45 (clone 2D1) | BD Biosciences | Cat#557833; RRID:AB_396891 |
| PE-Cy7 anti-human CD11c (clone 3.9) | Thermo Fischer Scientific | Cat#25-0116-42; RRID:AB_1582274 |
| PerCP/Cy5.5 anti-human HLA-DR (clone G46-6) | BD Biosciences | Cat#552764; RRID:AB_394453 |
| PE-Cy7 anti-human CD1c (clone L161) | Thermo Fischer Scientific | Cat#46-0015-42; RRID:AB_10548936 |
| Alexa Fluor 700 anti-human CD14 (clone M5E2) | BD Biosciences | Cat#557923; RRID:AB_396944 |
| FITC anti-human CD14 (clone 61D3) | eBioscience | Cat#11-0149-42; RRID:AB_10597597 |
| Brilliant Violet 605 anti-human CD163 (clone GHI/61) | BD Biosciences | Cat#745091; RRID:AB_2742705 |
| Brilliant Violet 786 anti-human CD204 (clone U23-56) | BD Biosciences | Cat#742443; RRID:AB_2740786 |
| Alexa Fluor 647 anti-human S100A8/9 (clone 5.5) | BD Biosciences | Cat#566010; RRID:AB_2732837 |
| Alexa Fluor 488 anti-human APOE (clone EP1374Y) | Abcam | Cat#ab196463; RRID:AB_867704 |
| Brilliant Violet 421 anti-human CCR2 (clone K036C2) | Biolegend | Cat#357210; RRID:AB_2563463 |
| PE/Dazzle594 anti-human CCR2 (clone K036C2) | Biolegend | Cat#357222; RRID:AB_2566752 |
| anti-human/mouse SynCAM (TSLC1/CADM1) (clone 3E1) | MBL | Cat#CM004-3; RRID:AB_592783 |

(*Continued on next page*)

*Continued*

| REAGENT or RESOURCE | SOURCE | IDENTIFIER |
|---|---|---|
| PerCP eFluor 710 anti-human CD64 (clone 10.1) | eBioscience | Cat#46-0649-42; RRID:AB_2573692 |
| PE-CF594 anti-human CD64 (clone 10.1) | BD Biosciences | Cat#565389; RRID:AB_2739213 |
| APC anti-human CD3 (clone UCHT1) | BD Biosciences | Cat#561810; RRID:AB_10893350 |
| Brilliant Violet 650 anti-human CD3 (clone UCHT1) | BD Biosciences | Cat#563851; RRID:AB_2744391 |
| APC anti-human CD19 (clone HIB19) | BD Biosciences | Cat#555415; RRID:AB_398597 |
| Brilliant Violet 650 anti-human CD19 (clone SJ25C1) | BD Biosciences | Cat#563226; RRID:AB_2744313 |
| Brilliant Violet 650 anti-human CD26 (clone M-A261) | BD Biosciences | Cat#744451; RRID:AB_2742240 |
| Brilliant Violet 650 anti-human BTLA (clone J168-540) | BD Biosciences | Cat#564803; RRID:AB_2738962 |
| FITC anti-human XCR1 (clone S15046E) | Biolegend | Cat#372612; RRID:AB_2715831 |
| Alex Fluor 488 Chicken IgY (clone F(ab')2 Fragment Donkey Anti- Chicken IgY (IgG) (H+L) (min X Bov, Gt, GP, Sy Hms, Hrs, Hu, Ms, Rb, Rat, Shp Sr Prot) *ML) (secondary antibody) | Jackson Immuno Research | Cat#703-586-155; RRID:AB_2340378 |
| FITC anti-mouse NKp46 (clone 29A1.4) | eBioscience | Cat#11-3351-82; RRID:AB_1210843 |
| FITC anti-mouse B220 (clone RA3-6B2) | BD Biosciences | Cat#553088; RRID:AB_394618 |
| FITC anti-mouse CD19 (clone MB19-1) | Biolegend | Cat#101506; RRID:AB_312825 |
| FITC anti-mouse CD3epsilon (clone 145-2C11) | Biolegend | Cat#100306; RRID:AB_312671 |
| FITC anti-mouse Ly6G (clone 1A8) | BD Biosciences | Cat#551460; RRID:AB_394207 |
| APC anti-mouse CD64 (clone X54-5/7.1) | Biolegend | Cat#139306; RRID:AB_11219391 |
| APC-Cy7 anti-mouse CD45 (clone 30-F11) | BD Biosciences | Cat#557659; RRID:AB_396774 |
| Alexa Fluor 700 anti-mouse MHCII (I-A I-E) (clone M5/114.15.2) | eBioscience | Cat#56-5321-82; RRID:AB_494009 |
| Brilliant Violet 421 anti-mouse CCR2 (clone SA203G11) | Biolegend | Cat#150605; RRID:AB_2571913 |
| Brilliant Violet 650 anti-mouse F4/80 (clone BM8) | Biolegend | Cat#123133; RRID:AB_2562305 |
| Brilliant Violet 650 anti-mouse CD11b (clone M1/70) | Biolegend | Cat#101259; RRID:AB_2566568 |
| Brilliant Violet 785 anti-mouse Ly6C (clone HK1.4) | Biolegend | Cat#128041; RRID:AB_2565852 |
| PE-Cy7 anti-mouse CD11c (clone N418) | eBioscience | Cat#25-0114-82; RRID:AB_469590 |
| PE anti-mouse FOLR2 (clone 10/FR2) | Biolegend | Cat#153303; RRID:AB_2721343 |
| 209Bi_CD16 (clone 3G8) | Biolegend | Cat#302002; RRID: AB_314202 |
| 112Cd_CD14.1 (clone TüK4) | Invitrogen | Cat#MHCD1400; RRID: AB_1464896 |
| 114Cd_CD14.2 (cloneTüK4) | Invitrogen | Cat#MHCD1400; RRID: AB_1464896 |
| 161Dy_CD172a (clone SE5A5) | Biolegend | Cat#323801; RRID:AB_830700 |
| 162Dy_AXL (clone AF154) | R&D Systems | Cat#AF154; RRID:AB_354852 |
| 163Dy_CD123 (clone 7G3) | BD Biosciences | Cat#554527; RRID: AB_395455 |
| 166Er_CD86 (clone IT2.2) | BD Biosciences | Cat#555663; RRID: AB_396017 |
| 167Er_OX40L (clone MAB10541) | R&D Systems | Cat#MAB10541; RRID:AB_2272152 |
| 168Er_CCR7 (clone 150503) | NovusBio | Cat#MAB197-SP; RRID: AB_2072803 |
| 170Er_CD88 (clone S5/1) | Biolegend | Cat#344302; RRID: AB_2259318 |
| 151Eu_CADM1 (clone 3E1) | MBL | Cat#CM004-3; RRID: AB_592783 |
| 153Eu_FcER1 (cloneAER-37; CRA-1) | eBiosciences | Cat#14-5899-82; RRID: AB_467710 |

(*Continued on next page*)

*Continued*

| REAGENT or RESOURCE | SOURCE | IDENTIFIER |
|---|---|---|
| 155Gd_CD33 (clone WM53) | BD Biosciences | Cat#555449; RRID: AB_395842 |
| 156Gd_CD163 (clone GHI) | Biolegend | Cat#333602; RRID: AB_1088991 |
| 157Gd_CCR2 (clone K036C2) | Biolegend | Cat#357201; RRID: AB_2561850 |
| 158Gd_CD56 (clone NCAM16.2) | BD Biosciences | Cat#559043; RRID: AB_397180 |
| 160Gd_CD207 (clone 4C7) | Biolegend | Cat#144201; RRID: AB_2562087 |
| 165Ho_CD303 (clone 201A) | Biolegend | Cat#354202; RRID: AB_11124104 |
| 115In_CD15 (clone HI98) | Biolegend | Cat#301902; RRID: AB_314194 |
| 175Lu_PDL1 (clone 29E.2A3) | Abcam | Cat#ab259283 |
| 142Nd_CD5 (clone UCHT2) | Biolegend | Cat#300602; RRID: AB_314088 |
| 143Nd_CD2 (clone TS1/8) | Biolegend | Cat#309202; RRID: AB_314752 |
| 144Nd_CD64 (clone 10.1) | Biolegend | Cat#305002; RRID: AB_314486 |
| 145Nd_CD68 (clone KP1) | eBiosciences | Cat#14-0688-80; RRID: AB_11151503 |
| 146Nd_CD3 (clone OKT3) | Biolegend | Cat#317301; RRID: AB_571926 |
| 146Nd_CD19 (clone HIB19) | eBiosciences | Cat#14-0199-82; RRID: AB_467151 |
| 146Nd_CD20 (clone 2H7) | eBiosciences | Cat#14-0209-82; RRID: AB_467153 |
| 148Nd_CD45RA (clone HI100) | Biolegend | Cat#304102; RRID: AB_314406 |
| 150Nd_CD80 (clone L307.4) | BD Biosciences | Cat#557223; RRID: AB_396602 |
| 147Sm_CD26 (clone BA5b) | Biolegend | Cat#302702; RRID: AB_314286 |
| 149Sm_HLA-DR (clone L243) | Biolegend | Cat#307602; RRID: AB_314680 |
| 152Sm_CD1c (clone L161) | Biolegend | Cat#331502; RRID: AB_2661820 |
| 154Sm_CD327 (clone 767329) | R&D Systems | Cat#MAB2859; RRID: |
| 159Tb_SLAN (clone DD-1) | Miltenyi Biotec | Cat#130-119-952; RRID:AB_2751943 |
| 169Tm_LYVE1 (clone NB600-10080) | NovusBio | Cat#NB600-1008; RRID:AB_10000497 |
| 89Y_CD45 (clone HI30) | Fluidigm | Cat#3089003B; RRID: AB_2661851 |
| 171Yb_CD34 (clone 581) | Biolegend | Cat#343501; RRID: AB_1731969 |
| 172Yb_TSLPR (clone 1B4) | Biolegend | Cat#322802; RRID: AB_604159 |
| 173Yb_CX3CR1 (clone K0124E1) | Biolegend | Cat#355701; RRID: AB_2561725 |
| 174Yb_CD206 (clone 19.2) | BD Biosciences | Cat#555953; RRID: AB_396249 |
| 176Yb_CD11b (clone ICRF44) | Biolegend | Cat#301302; RRID: AB_314154 |
| 141Pr_CLEC12A (clone 687317) | R&D Systems | Cat#MAB2946; RRID: AB_10888842 |
| Purified NA/LE Hamster Anti-Mouse CD3e (clone 145-2C11) | BD Biosciences | Cat# 567114; RRID: AB_394590 |
| Purified NA/LE Hamster Anti-Mouse CD28 (clone 37.51) | BD Biosciences | Cat# 553294; RRID: AB_394763 |
| **Biological samples** | | |
| Formalin-fixed, paraffin-embedded (FFPE) specimens from distinct tumor types | Tissue bank of the Department of Pathology (ASST, Spedali Civili di Brescia, Brescia, Italy) | Contact: william.vermi@unibs.it |
| Breast cancer tissue microarrays | AMSBIO, England | N/A |
| Fresh breast tumor, non-tumoral breast tissue, metastatic lymph nodes and non-metastatic lymph nodes samples | Curie Hospital, Paris, France | N/A |
| Human peripheral blood | Curie Hospital, Paris, France | N/A |
| **Chemicals, peptides, and recombinant proteins** | | |
| Bovine Serum Albumin | SIGMA | Cat#A7906 |
| Human albumin | LFB | Vialebex (200mg/ml) |
| $CO_2$ independent medium | Gibco | Cat#18045088 |
| RPMI 1640 GlutaMAX | Gibco | Cat#61870036 |
| DNAse 1 | Roche | Cat#5401020001 |

(*Continued on next page*)

*Continued*

| REAGENT or RESOURCE | SOURCE | IDENTIFIER |
|---|---|---|
| Liberase TL | Sigma | Cat#10104159001 |
| EDTA | Gibco | Cat#15575-038 |
| RBC lysis buffer | Eliane Piaggio's Lab | N/A |
| Novolink Polymer | Leica Microsystem | Cat#RE7200-CE |
| beta-Mercaptoethanol | LifeTechnologies | Cat#31350-010 |
| HEPES | Gibco | Cat#15630-056 |
| FcR blocking reagent | Miltenyi | Cat#130-059-901 |
| Live and Dead AQUA | Thermo Fischer Scientific | Cat#L34957 |
| Fetal Calf Serum | Eurobio | Cat#CVFSVF00-01 |
| Penicillin-Streptomycin | Gibco | Cat#15140-122 |
| **Critical commercial assays** | | |
| Chromium Single Cell 3′ (v2 Chemistry) | 10x Genomics | Cat#CG00052 |
| Chromium Single Cell 3′ (v3 Chemistry) | 10x Genomics | Cat#CG000183 |
| Fixation/Permeabilization (Concentrate and Diluent) | eBioscience | Cat#00-5521-00 |
| Mach 4 MR-AP | Biocare Medical | Cat#M4U536 |
| Opal 7-Color IHC Kit | Akoya 23 Biosciences | Cat#NEL821001KT |
| **Deposited data** | | |
| Deposited raw data files for Single-cell RNA-seq and Bulk RNA-seq data from this study | This paper | GEO: GSE192935 |
| Raw data files for Single-cell RNA-seq | Azizi et al., 2018 | GEO: GSE114725 |
| Raw data files for Single-cell RNA-seq | Han et al., 2018 | GEO: GSE108097 |
| Microarray gene expression data from Franklin et al. (2014) | Franklin et al., 2014 | GEO: GSE56755 |
| Microarray gene expression data from Finak et al. (2008) | Finak et al., 2008 | GEO: GSE9014 |
| Gene expression data from Wang et al., (2005b) | Wang et al., 2005b | GEO: GSE2034 |
| TCGA datasets | Broad Institute portal | http://gdac.broadinstitute.org |
| scRNA-seq and bulk RNAseq codes | Adapted to this paper | https://data.mendeley.com/datasets/b2vfxbc2dp/1 (https://doi.org/10.17632/b2vfxbc2dp.1) |
| CPTAC BRCA study | Clinical Proteomic Tumor Analysis Consortium (NCI/NIH) | http://linkedomics.org/data_download/TCGA-BRCA/ |
| **Experimental models: Cell lines** | | |
| Py8119 (mesenchymal-like) | ATCC | CRL-3278 |
| Py230 (epithelial-like) | ATCC | CRL-3279 |
| 4T1 | Dr. Clotilde Thery Lab, Institut Curie, Paris, France | N/A |
| **Experimental models: Organisms/strains** | | |
| C57BL6/J mice | Institut Curie, Paris, France | N/A |
| MMTV-PyMT mice | Institut Curie, Paris, France | N/A |
| Balb/c mice | Institut Curie, Paris, France | N/A |
| NSG mice | Institut Curie, Paris, France | N/A |
| OTI $Rag^{-/-}$ mice | Institut Curie, Paris, France | N/A |
| **Software and algorithms** | | |
| FlowJo v10 | Tree Star | www.flowjo.com |
| GraphPad Prism v6 | GraphPad | www.graphpad.com |

(*Continued on next page*)

*Continued*

| REAGENT or RESOURCE | SOURCE | IDENTIFIER |
|---|---|---|
| Cell Ranger | 10x Genomics | www.10xgenomics.com/ |
| Seurat | Butler et al., 2018 | www.satijalab.org/seurat/ |
| R v4.0.2 | The R Project for Statistical Computing | www.r-project.org |
| Vectra 3.0 | PerkinElmer | perkinelmer.com |
| SCENIC | GitHub | https://github.com/aertslab/SCENIC |
| InForm Cell Analysis v2.4.6 | Akoya Biosciences | www.akoyabio.com |
| Similarity Score was defined using Seurat v3 | Stuart et al., 2019 | https://satijalab.org/seurat/articles/integration_introduction.html |
| REACTOME | Yu and He, 2016 | https://bioconductor.org/packages/release/bioc/html/ReactomePA.html |
| HALO | Indica Labs | indicalab.com/halo |
| NDPview2 | Hamamatsu | https://www.hamamatsu.com/us/en/product/life-science-and-medical-systems/digital-slide-scanner/U12388-01.html |
| DIVA | BD Biosciences | www.bdbiosciences.com/en-us |
| ClueGO, Cytoscape | Bindea et al., 2009 | https://apps.cytoscape.org/apps/cluego |
| Script for CyTOF analysis | N/A | N/A |
| FlowSOM | Van Gassen et al., 2015 | https://github.com/SofieVG/FlowSOM |
| Pheatmap | N/A | https://cran.r-project.org/web/packages/pheatmap/index.html |
| MCP counter | Becht et al., 2016 | N/A |
| TIMER2.0 | Li et al., 2017 | http://timer.cistrome.org/ |
| survival (3.1-12), R package | A Package for Survival Analysis in R. R package version 3.2-13 | https://CRAN.R-project.org/package=survival |
| survminer (0.4.6), R package | STHDA January 2016. survminer R package: Survival Data Analysis and Visualization. | https://CRAN.R-project.org/package=survminer |
| genefu (2.22.1), R package | Gendoo et al., 2016 | http://www.bioconductor.org/packages/release/bioc/html/genefu.html |
| corrplot R package (0.84) | R package 'corrplot': Visualization of a Correlation Matrix. (Version 0.92) | https://github.com/taiyun/corrplot |
| ggplot2 (3.3.0) | ggplot2: Elegant Graphics for Data Analysis. Springer-Verlag New York | https://CRAN.R-project.org/package=ggplot2 |
| ComplexHeatmap (2.7.6.1003) | Gu et al., 2016 | https://www.bioconductor.org/packages/release/bioc/html/ComplexHeatmap.html |
| biomaRt (2.46.3) | Durink et al., 2009 | https://bioconductor.org/packages/release/bioc/html/biomaRt.html |
| Imaris 7.4 | Oxford Instruments | https://imaris.oxinst.com/ |

## RESOURCE AVAILABILITY

### Lead contact

Further information and requests for resources and reagents should be directed to and will be fulfilled by the lead contact, Julie Helft, julie.helft@inserm.fr.

### Materials availability

This study did not generate new unique reagents.

### Data and code availability

Single-cell and bulk RNAseq data have been deposited at GEO and are publicly available as of the date of publication. Single-cell RNA-sequencing data were analyzed using the Seurat 3 R pipeline according to Butler et al. (2018) with modifications adapted to

our study. Bulk RNA-sequencing data were analyzed based on Love et al. (2014) with modifications adapted to our study. The codes are available at Mendeley Data (https://data.mendeley.com/datasets/b2vfxbc2dp/1). GEO accession numbers are listed in the key resources table.

Microscopy data reported in this paper will be shared by the lead contact upon request.

This paper analyzes existing, publicly available data. These accession numbers for the datasets are listed in the key resources table.

Any additional information required to reanalyze the data reported in this paper is available from the lead contact upon request.

## EXPERIMENTAL MODEL AND SUBJECT DETAILS

### Human specimens

Primary tumors, tissues adjacent to the tumor (juxta-tumor), metastatic and non-metastatic tumor-draining lymph nodes were surgically resected from treatment-free luminal breast cancer patients at the Institut Curie Hospital (Paris, France), in accordance with institutional ethical guidelines and after informed consent of patient was obtained. The protocol was approved by the Ethical Committee of Institut Curie (“Comité de la Recherche Institutionel” CRI-0804-2015). Patients clinical and pathological information are summarized in Table S1. Tumor metastasis in tumor draining lymph nodes were diagnosed by the pathology department of Institut Curie and further confirmed by measuring by flow cytometry the percentage of $EPCAM^{+}CD45^{-}$ cells among live cells.

FOLR2 and TREM2 immunohistochemistry were performed on tumor sections retrieved from the archive of the Pathology Unit, ASST Spedali Civili di Brescia (see Table S1).

### Cell lines

Murine tumor cell lines were grown in a humidified atmosphere at 37°C in 5% CO2. Py8119 and Py230 cell lines (ATCC) were cultured in F12K media (ATCC), complemented with 10% FCS (Eurobio), 1% Pencillin/Streptomycin, 0,1% β-Mercaptoethanol (LifeTechnologies) and 0,1% Mito+ serum extender (Corning) for Py230 cells. 4T1 cells were a gift from Dr. Clotilde Thery (Institut Curie, Paris) and were cultured in RPMI 1640 GlutaMAX (Gibco) containing 10% FCS (Eurobio), 1% Pencillin/Streptomycin, 1mM Sodium Pyruvate and 10mM HEPES (Gibco).

### Mice

Transgenic MMTV-PyMT mice in C57Bl/6 background (Davie et al., 2007), OTI x $Rag^{-/-}$ mice and NOD-scid-$IL2r\gamma^{-/-}$ (NSG) mice were maintained in a specific pathogen-free animal facility in accordance with Institut Curie guidelines. Healthy C57BL/6J and BALB/c female mice were obtained from Charles River Laboratories, maintained in a non-barrier facility and included at 8-12 weeks of age for experimental procedures. Animal care and use for this study were performed in accordance with the recommendations of the European Community (2010/63/UE) for the care and use of laboratory animals. Experimental procedures were specifically approved by the ethics committee of the Institut Curie CEEA-IC #118 (Authorization APAFiS#31138-2021042219022400-v1 given by National Authority) in compliance with the international guidelines.

MMTV-PyMT transgenic mice develop mammary tumors in all mammary glands. Tumors were allowed to grow for 12 weeks (neoplasia) to 24 weeks (late carcinoma) before harvest.

For analysis of tissue-resident macrophages, inguinal LNs were removed on the right and left sides and healthy $4^{th}$ mammary gland fat-pad were harvested in 8-12 weeks old WT C57Bl/6, BALB/c or NSG mice or MMTV-PyMT littermate controls.

## METHOD DETAILS

### Human samples processing

Patient samples were processed as previously described (Núñez et al., 2020). In brief, freshly resected human samples were cut into small fragments and digested with 0.1 mg/ml Liberase TL (Roche) and 0.1 mg/ml DNase (Roche) in CO2-independent medium (Gibco) containing 0,4 g/l of human albumin (Vialebex) for 30 min at 37°C. Single cell suspension of dissociated tissues was filtered on a 40μm cell strainer (BD Biosciences), washed with CO2-independent medium + 0.4 g/l of human albumin and resuspended in medium for cell counting.

### Mouse tumor orthotopic transplantation

Py230 ($10^6$ cells), Py8119 ($10^6$ cells), 4T1 ($0{,}5x10^6$ cells) suspended in 200μl of PBS 1X were injected sub-cutaneously in the $4^{th}$ mammary gland fat-pad of C57Bl/6 (Py230, Py8119) or BALB/c (4T1) mice. Tumors were allowed to grow during 30 days before harvest and analysis.

### Mouse tissues processing

For macrophage subset analysis, mammary tumors from MMTV-PyMT transgenic mice or from WT mice orthotopically transplanted with mammary tumor cell lines (Py230, Py8119, 4T1) were cut into small pieces and enzymatically digested for 1h at 37°C in CO2-independent medium (Gibco) containing 150 μg/mL DNAse and 75 μg/mL Liberase TL (Roche). Healthy mammary glands from

MMTV-PyMT littermate controls were digested following the same enzymatic digestion protocol for 20 minutes. After digestion, remaining tissue-pieces were mashed with a plunger and cell suspensions were filtered on a 40μm cell-strainer (BD Biosciences). For both healthy and malignant mammary glands tissue-suspension, red blood cells were lysed with homemade red blood lysis buffer (8,32mg/ml of NH4CL + 0,84mg/ml of NaHCo3 + 0,043mg/ml of EDTA in H2O) for 2 minutes at room temperature. Finally, cells were resuspended in cold FACS buffer (1x PBS containing 2mM EDTA (Invitrogen) and 0.5% bovine serum albumin (BSA; Sigma)) for further analysis.

$CD8^+$ T cells used for T cell assays were isolated from OTI x $Rag^{-/-}$ mice or WT C57Bl/6 mice. To this end, spleen and peripheral LNs were harvested, mashed through a 40μm cell strainer and washed in cold PBS before red blood cell lysis (2 minutes at room temperature). Cells were further washed in cold 1x PBS + 2mM EDTA + 0.5% BSA for further assays.

## Murine and human macrophage FACS sorting

After tissue-dissociation, cells were incubated with primary antibodies for 30 minutes at 4°C, washed twice and resuspended in FACS buffer (1x PBS containing 2mM EDTA (Invitrogen) and 0.5% bovine serum albumin (BSA; Sigma)). Fc receptors were blocked with the anti-mouse CD16/CD32 (clone 2.4.G2) mAb (BD) for murine cells or with FcR blocking reagent (Miltenyi) for human cells. For CADM1 staining, cells were washed after the primary staining and incubated with a secondary antibody for an additional 30 minutes at 4°C, washed twice and resuspended in FACS buffer. Live/dead cell discrimination was performed by extemporaneous DAPI staining (working concentration 0,01μg/ml, Invitrogen). Cells were sorted using BD FACS-ARIA III flow cytometer (BD Biosciences).

**Murine macrophages** were sorted as Lineage(CD3/CD19/NKP46/B220/Ly6G)$^-$Ly6C$^-$F4/80$^+$CD64$^+$Folr2$^+$ or Lineage(CD3/CD19/NKP46/B220/Ly6G)$^-$Ly6C$^-$F4/80$^+$CD64$^+$Folr2$^-$Cadm1$^+$

**Human macrophages** were sorted as CD45$^+$Lineage(CD3/CD19/CD56/CD1c)$^-$CD11c$^+$HLA-DR$^+$XCR1$^-$CD14$^+$CCR2$^-$CD64$^+$CADM1$^-$FOLR2$^+$ or CD45$^+$Lineage(CD3/CD19/CD56/CD1c)$^-$CD11c$^+$HLA-DR$^+$XCR1$^-$CD14$^+$CCR2$^-$CD64$^+$CADM1$^+$FOLR2$^-$. **Human monocytes** were sorted as Lineage(CD3/CD19/CD56/CD1c)$^-$CD11c$^+$HLA-DR$^+$XCR1$^-$ CD14$^+$CCR2$^+$.

## Mouse T cell suppression assay

### *Plate coating*

Flat bottom 96 well culture plate were coated with 10μg/ml of anti-CD3e (BD Bioscience) diluted in 1X PBS overnight at 4°C or 2h at 37°C. Plate was washed once with 1X PBS.

### *T cell preparation*

$CD8^+$ T cells from spleens and LNs of C57BL/6 WT mice were harvested and purified using the $CD8a^+$ T Cell Isolation Kit, (130-104-075, Miltenyi) after red blood cell lysis. For proliferation assay, purified $CD8^+$ T cells were labeled with 2μM of carboxyfluorescein succinimidyl ester (CFSE, Invitrogen) at 37° C for 8 minutes.

### *Macrophage isolation*

Lineage(CD3/CD19/NKP46/B220/Ly6G)$^-$Ly6C$^-$F4/80$^+$CD64$^+$FOLR2$^+$ or Lineage (CD3/CD19/NKP46/B220/Ly6G)$^-$Ly6C$^-$F4/80$^+$CD64$^+$CADM1$^+$ macrophages were isolated by FACs-sorting from mammary tumors of 22-24 weeks old PyMT mice or age-matched littermate controls (Figure S7A).

### *Macrophage and T cell co-culture*

50,000 macrophages were plated in 100μl/well in the anti-CD3-coated 96w-plate in complete RPMI medium (10% FCS + 1% Pencillin/Streptomycin + 1mM Sodium Pyruvate and 10mM HEPES). Anti-CD28 (1μg/ml final concentration, BD Bioscience) was added to the CFSE labelled T cells before plating at a ratio of 1 T cell for 2 macrophages. In some instance recombinant TGFβ (100ng/ml, Peprotech) was added to the culture.

### *T cell activation analysis by flow cytometry*

after 3 days of co-culture, T cells were stained for CD44, CD25, CD62L, PD-1 to analyze their activation status. CFSE dilution was analyzed to assess T cell proliferation.

## Mouse T cell priming assay

### *T cell preparation*

OTI $CD8^+$ T cells from spleens and lymph nodes of OTI x $Rag1^{-/-}$ mice were labeled for proliferation assay with 2μM of CellTrace Violet (CTV, Invitrogen) at 37°C for 20 minutes, washed and counted before culture with macrophages.

### *Macrophage isolation*

Lineage (CD3/CD19/NKP46/B220/Ly6G)-Ly6C$^-$F4/80$^+$CD64$^+$FOLR2$^+$ or Lineage (CD3/CD19/NKP46/B220/Ly6G)-Ly6C$^-$F4/80$^+$CD64$^+$CADM1$^+$ macrophages were isolated by FACs-sorting from healthy mammary glands or mammary tumors of 22-24 weeks old PyMT mice or age-matched littermate controls.

### *Macrophage and T cell co-culture*

25,000 macrophages were plated in flat-bottom 96 well plates and incubated with various doses of the SIINFEKL OVA peptide (0,1 to 100nM) in complete RPMI medium (10% FCS + 1% Pencillin/Streptomycin + 1mM Sodium Pyruvate and 10mM HEPES) for 45 minutes at 37°C. After 2 washes, 25,000 CTV labeled OTI $CD8^+$ T cells were added on top of the SIINFEKL pulsed macrophages at a 1:1 ratio.

### *T cell activation analysis by flow cytometry*

after 3 days of co-culture, T cells were stained for CD8, CD44, CD25, CD62L, PD-1 to analyze their activation status. CTV dilution was analyzed to assess T cell proliferation. For intracellular cytokine detection, T cells were first stained for cell surface CD8 expression, 30 minutes at 4°C, washed in complete RPMI medium and incubated for 4 hours at 37°C with phorbol 12-myristate 13-acetate (20 ng/ml; Sigma-Aldrich), 1 μM ionomycin (Sigma-Aldrich), and BD GolgiPlug in complete RPMI. After washing, re-stimulated T cells were stained for CD8 prior fixation with BD PermFix buffer for 20 minutes. Intracellular staining for GZMB, IFN-γ, TNF-α, IL-2 was performed in BD PermWash buffer for 30 minutes.

## Mass cytometry staining

For mass cytometry, pre-conjugated or purified antibodies were obtained from Invitrogen, Fluidigm (pre-conjugated antibodies), Biolegend, eBioscience, Becton Dickinson or R&D Systems. For some markers, fluorophore-conjugated or biotin-conjugated antibodies were used as primary antibodies, followed by secondary labeling with anti-fluorophore metal-conjugated antibodies (such as the anti-FITC clone FIT 22) or metal-conjugated streptavidin, produced as previously described (Becher et al., 2014). Briefly, patient lymph nodes cell suspension (around $30x10^6$ cells/well in a U-bottom 96 well plate; BD Falcon, Cat# 3077) were washed once with 200 mL FACS buffer (4% FBS, 2mM EDTA, 0.05% Azide in 1X PBS), then stained with 100 mL 200 mM cisplatin (SigmaAldrich, Cat# 479306-1G) for 5 min on ice to exclude dead cells. Cells were then washed with FACS buffer and once with PBS before fixing with 200 mL 2% paraformaldehyde (PFA; Electron Microscopy Sciences, Cat# 15710) in PBS overnight or longer. Following fixation, the cells were pelleted and resuspended in 200μL 1X permeabilization buffer (Biolegend, Cat# 421002) for 5 min at room temperature to enable intracellular labeling. Bromoacetamidobenzyl-EDTA (BABE)-linked metal barcodes were prepared by dissolving BABE (Dojindo, Cat# B437) in 100mM HEPES buffer (GIBCO, Cat# 15630) to a final concentration of 2 mM. Isotopically-purified PdCl2 (Trace Sciences) was then added to the 2 mM BABE solution to a final concentration of 0.5 mM. Similarly, DOTA-maleimide (DM)-linked metal barcodes were prepared by dissolving DM (Macrocyclics, Cat# B-272) in L buffer (MAXPAR, Cat# PN00008) to a final concentration of 1 mM. RhCl3 (Sigma) and isotopically-purified LnCl3 was then added to the DM solution at a final concentration of 0.5 mM. Six metal barcodes were used: BABE-Pd-102, BABE-Pd-104, BABE-Pd-106, BABE-Pd-108, BABE-Pd-110 and DMLn-113. All BABE and DM-metal solution mixtures were immediately snap-frozen in liquid nitrogen and stored at 80C. A unique dual combination of barcodes was chosen to stain each tissue sample. Barcode Pd-102 was used at a 1:4000 dilution, Pd-104 at a 1:2000, Pd-106 and Pd-108 at a 1:1000, and Pd-110 and Ln-113 at a 1:500. Cells were incubated with 100 mL barcode in PBS for 30 min on ice, washed in permeabilization buffer and then incubated in FACS buffer for 10 min on ice. Cells were then pelleted and resuspended in 100 mL nucleic acid Ir-Intercalator (MAXPAR, Cat# 201192B) in 2% PFA/PBS (1:2000), at room temperature. After 20 min, cells were washed twice with FACS buffer and twice with water before being resuspended in water. In each set, the cells were pooled from all tissue types, counted, and diluted to 0.5x106 cells/mL. EQ Four Element Calibration Beads (DVS Science, Fluidigm) were added at a 1% concentration prior to acquisition.

## Human and mouse sample processing for single cell RNA-sequencing

### *Mouse tumors*

After tissue processing, dissociation and cell counting, cell suspensions were maintained on ice and stained for FACS-sorting with DAPI and fluorophore-conjugated antibodies: Lineage (CD3, CD19, NKP46, B220, Ly6G) and CD45. $CD45^+$Lineage- cells were sorted with a FACS-ARIA III (BD) and collected in cold 1x PBS containing 0.04% of BSA for cell counting. The concentration of single cell suspensions was adjusted to 600 cells/μl. Approximately 6,000 to 10,000 sorted cells were loaded in a 10x Genomics Chromium chip.

### *Human tumors*

After tissue processing, dissociation and cell counting, cell suspensions were maintained on ice and stained for FACS-sorting with DAPI and fluorophore-conjugated antibodies (see key resources table). Cells were isolated using FACS-ARIA III (BD) cell sorter according to the gating strategies shown in Figure S2D and collected in cold 1x PBS containing 0.04% of BSA for cell counting. PBMC were obtained from fresh blood samples by density gradient centrifugation using Lymphoprep (Stemcell Technologies) according to the manufacturer instructions, then washed and resuspended in CO2-independent medium + 0.4 g/l of human albumin prior FACS-sorting. Patients samples were processed within 1 hour after tumor resection. The concentration of single cell suspensions was adjusted to 300 cells/μl, and 3,000 to 5,000 sorted cells were loaded in a 10x Genomics Chromium chip within 6 hours.

## Single-cell RNA-sequencing

Human and mouse cellular suspensions were loaded on a 10x Chromium Controller (10X Genomics) according to manufacturer's protocol based on the 10x GEMCode proprietary technology. Single-cell RNA-Seq libraries were prepared using Chromium Single Cell 3′ v2 or v3 Reagent Kit (10x Genomics) according to manufacturer's protocol. Briefly, the initial step consisted in performing an emulsion where individual cells were isolated into droplets together with gel beads coated with unique primers bearing 10X cell barcodes, unique molecular identifiers (UMI), and poly(dT) sequences. Reverse transcription reactions were engaged to generate barcoded full-length cDNA followed by the disruption of emulsions using the recovery agent and cDNA clean up with DynaBeads MyOne Silane. Bulk cDNA was amplified using a GeneAmp PCR System 9700 with 96-Well Gold Sample Block Module (Applied Biosystems) (98 °C for 3 min; cycled 11/12 ×: 98 °C for 15 s, 63 °C for 20 s and 72 °C for 1 min; held at 4 °C). Amplified cDNA product was cleaned

up with the SPRI select Reagent Kit (Beckman Coulter). Indexed sequencing libraries were constructed using the reagents from the Chromium Single Cell 3′ v3 Reagent Kit, following these steps: (1) fragmentation, end repair, and a-tailing; (2) size selection with SPRI select; (3) adaptor ligation; (4) post ligation cleanup with SPRI select; (5) sample index PCR and cleanup with SPRI select beads. Library quantification and quality assessment was performed using Qubit fluorometric assay (Invitrogen) with dsDNA HS (High Sensitivity) Assay Kit and Bioanalyzer Agilent 2100 using a High Sensitivity DNA chip (Agilent). Indexed libraries were pooled according to number of cells and sequenced on a NovaSeq 6000 (Illumina) using paired-end 28 × 91 bp. A depth around 50,000 reads per cell was obtained.

### Bulk RNA-sequencing

After tissue processing and cell count, cell suspensions were washed in cold FACS buffer (PBS + 0.5% BSA + 2mM EDTA) and stained with fluorophore conjugated antibodies and Fc-receptors blocking (Miltenyi) for 30 minutes at 4°C. Myeloid cell subsets were isolated using FACS-ARIA III (BD) cell sorter and directly collected on lysing TCL buffer (QIAGEN) containing 1% of beta-mercaptoethanol before storage at -80°C. RNA were extracted and isolated using the Single Cell RNA purification kit (Norgen, Cat#51800) according to the manufacturer's instructions. After extraction, total RNA was analyzed using Agilent RNA 6000 Pico Kit on the Agilent 2100 Bioanalyzer System. RNA quality was estimated based on capillary electrophoresis profiles using the RNA Integrity Number (RIN). RNA sequencing libraries were prepared using the SMARTer Stranded Total RNA-Seq Kit v2 - Pico Input Mammalian (Clontech/Takara). The input quantity of total RNA was comprised between 1 and 22ng. This protocol includes a first step of RNA fragmentation, using a proprietary fragmentation mix at 94°C. The time of incubation was set up for each sample, based on the RNA quality, and according to the manufacturer's recommendations. After fragmentation, indexed cDNA synthesis was performed. Then the ribodepletion step was performed, using probes specific to mammalian rRNA. PCR amplification was finally achieved to amplify the indexed cDNA libraries, with a number of cycles set up according to the input quantity of tRNA. Library quantification and quality assessment was performed using Qubit fluorometric assay (Invitrogen) with dsDNA HS (High Sensitivity) Assay Kit and LabChip GX Touch using a High Sensitivity DNA chip (Perkin Elmer). Libraries were then equimolarly pooled and quantified by qPCR using the KAPA library quantification kit (Roche). Sequencing was carried out on the NovaSeq 6000 (Illumina), targeting between 10 and 15M reads per sample and using paired-end 2 x 100 bp.

### Immunohistochemistry

Formalin-fixed, paraffin-embedded tissue blocks were cut with a microtome into fine slivers of 3 microns. Immunohistochemistry was processed in a Bond RX automated (Leica) with Bond Polymer refine detection kit (Leica, DS9800). Antigen retrieval was performed in BOND Epitope Retrieval Solution 1 (Leica, AR9961). Primary antibody APOE (Abcam; ab52607) was incubated 30 minutes at room temperature. Slides were counterstained with hematoxylin before mounting with resin. Images were acquired by using Digital Pathology slide scanner (Ultra Fast Scanner 1.8, Philips)

FOLR2 expression was tested on human tissues by using immunohistochemistry. Sample included reactive lymph nodes (n=7), primary carcinomas (n=47), metastatic tumor draining lymph nodes (n=7) and distant metastasis to lung (n=8) and liver (n=11) from different primary site (breast, bladder, gastro-intestinal, lung, kidney and skin) (Table S1) retrieved from the archive of the Pathology Unit, ASST Spedali Civili di Brescia. Briefly, anti-FOLR2 (clone OTI4G6, 1:100, Thermo Fisher SCIENTIFIC) and anti-TREM2 (clone D814C, 1:100, Cell Signaling Technology) antibodies were revealed using Novolink Polymer (Leica) followed by DAB. For double staining, FOLR2 was combined with anti-CD3 (clone LN10, 1:70, Leica Biosystem), anti-CD20 (clone L26, 1:200, Leica Biosystem), anti-CD31 (clone PECAM-1, 1:50, Leica) and anti-TREM2. Briefly, after completing the first immune reaction, the second immune reaction was visualized using Mach 4 MR-AP (Biocare Medical), followed by Ferangi Blue. Localization of FOLR2$^+$ cells within TLS was confirmed by double for the B-cell marker CD20 and the T-cell marker CD3.

### Immunofluorescence on fixed tumor slices

Biopsies were fixed overnight at 4°C in a Periodate-Lysine-Paraformaldehyde solution (0.05 M phosphate buffer containing 0.1 M L-lysine [pH 7.4], 2 mg/ml NaIO4, and 10 mg/ml paraformaldehyde). Fixed tumors were then embedded in 5% low-gelling-temperature agarose (type VII-A, Sigma-Aldrich) and cut into 400 μm-thick slices as previously described (Peranzoni et al., 2018). Tumor slices were stained for 15 minutes at 37°C with fluorophore conjugated antibodies (see key resources table). All antibodies were diluted in 1x PBS and used at a concentration of 5 μg/ml, except anti-FOLR2 and anti-CD31 antibodies that were used at 10 μg/ml. Z-stack images of 5x5 fields were taken with a 10x water immersion objective (10x/0.3 N.A.) on an inverted spinning disk confocal microscope (IXplore, Olympus). Virtual slices were reconstituted and analyzed with the ImageJ software.

### Tumor slice imaging

To evaluate resident CD8$^+$ T cell migration, tumor slices were prepared following the protocol described previously (Peranzoni et al., 2018). Briefly, samples were embedded in 5% low-gelling-temperature agarose (type VII-A; Sigma-Aldrich) prepared in 1x PBS. Slices (400 μm) were cut with a vibratome (VT 1000S; Leica) in a bath of ice-cold PBS. Slices were transferred to 0.4-μm organotypic culture inserts (merck millipore Cat# PICM03050) in 35-mm Petri dishes containing 1 ml RPMI 1640 without Phenol Red. Live vibratome sections were stained with the following antibodies: BV421-anti-human EpCAM (9C4 clone; BioLegend), PerCP-Cy5.5-anti-human- CD8a (SK1 clone; BioLegend) and APC-anti-human FOLR2 (94b clone; BioLegend) at 10 μg/mL in RPMI 1640 without Phenol

Red supplemented with 3% of huma serum. T cells were imaged with a DM500B upright microscope equipped with an upright spinning disk confocal microscope (Leica) with a 37°C thermostatic chamber. For dynamic imaging, tumor slices were secured with a stainless-steel slice anchor (Warner Instruments) and perfused at a rate of 0.3 mL/min with a solution of RPMI without Phenol Red, bubbled with 95% $O_2$ and 5% $CO_2$. Images from a first microscopic field were acquired with a 25× water immersion objective (20×/0.95 N.A.; Olympus). For four-dimensional analysis of cell migration, stacks of 6–10 sections (z step = 8 μm) were acquired every 20 s for 20 min at depths up to 80 m. Regions were selected for imaging when tumor parenchyma, stroma, FOLR2$^+$ macrophages, and CD8$^+$ T cells were simultaneously present in the same microscopic field. Between two and four microscopic fields were selected for each tumor samples for time-lapse experiments.

## QUANTIFICATION AND STATISTICAL ANALYSIS

### Flow cytometry analysis

After tissue processing and cell counting, cell suspensions (around 2x10$^6$ human cells or 5x10$^6$ murine cells) were stained with Live/Dead Fixable Aqua Dead Cell Stain Kit (Life Technologies) in PBS for 10 minutes at room temperature. Cells were then washed in 1x PBS + 2mM EDTA + 0.5% BSA and stained with fluorophore-conjugated antibodies in the presence of Fc-receptors blocking reagent during 30 minutes at 4°C. When needed, cell suspensions were subsequently washed with FACs buffer and submitted to intracellular staining (1 hour at 4°C) using fixation/permeabilization kit (eBiosciences for human cells or BD Biosciences for murine cells) according to the manufacturer instructions. Data acquisition was performed using an LSR-Fortessa (BD), compensation and analysis were done using FlowJo software (TreeStar).

### CyTOF data analysis

Cell data were acquired and analyzed using a CyTOF Mass cytometer (Fluidigm). The CyTOF data were exported in a conventional flow-cytometry file (.fcs) format and normalized using previously-described software (Finck et al., 2013). Events with zero values were randomly assigned a value between 0 and –1 using a custom R script employed in a previous version of the mass cytometry software (Newell et al., 2012). Cells for each barcode were deconvolved using the Boolean gating algorithm within FlowJo. The CD45$^+$Lineage (CD3/CD19/CD20)$^-$HLA-DR$^{+/-}$ CD14+ population of lymph nodes were gated using FlowJo, exported as a.fcs file and uploaded into R studio (R software environment, version R4) using ‘‘flowCore’’ packages. To obtain an unbiased overview, we systematically reduced the flow cytometry data to two dimensions by applying uniform manifold approximation (UMAP, R package ‘‘umap’’). All cells were clustered using the FlowSOM algorithm (R package ‘‘FlowSOM’’) (Van Gassen et al., 2015) in conjunction with consensus clustering (R package ‘‘ConsensusClusterPlus’’) and subsequently manually annotated accordingly to Brummelman et al. (2019).

### Single-cell RNA-sequencing data processing and analysis

#### *Alignment and raw expression matrix construction*

Human and mouse raw sequencing data were respectively aligned on reference genome GRCh38/84 and GRCm38/84 (genome assembly/ENSEMBL release) using 10X software CellRanger (Version 3.0.2) with default parameters. Gene expression counts for individual cells were generated using cellranger count.

#### *Cell selection, filtering, and normalization*

For both human and mouse raw count matrix, we kept cells expressing at least 200 genes. Cells with mitochondrial content greater than 10 to 20 % were removed. After this quality control, data were normalized by total counts following the Seurat 3 R pipeline (Butler et al., 2018). Cells identified as contaminant of the gating strategy (T/B/NK cells, LAMP3$^+$ DCs *e.g.*) or cells with high heat-shock-protein or ribosomal coding genes content in which no myeloid cell identifying gene could be detected, were filtered out.

#### *Variable gene selection and sample merging*

For sample merging we applied a VST (Variance Stabilizing Transformation) method selecting for the most variable genes. We performed the Seurat V3 integration pipeline using the most 8000 genes for the ten human samples. The 3000 most variable genes were used to merge the two mice samples. For both anchors selection and integration steps we used the default parameters of Seurat V3 functions.

#### *Dimensionality reduction and visualization*

Data were scaled by applying a regression using as variation factors, the total UMI counts, the percent of expressed mitochondrial genes, the origin sample and tissue of each cell and the version of CellRanger chemistry kit used for sequencing. Heatmaps are showing z-scores of this scaled matrix. The UMAP visualization was built using respectively the 50 and 30 most informative components of the PCA for Human and Mouse.

#### *Clustering and differential gene expression analysis*

The clustering was processed by constructing a Shared Nearest Neighbor (SNN) Graph. The 20 neighbors of each cell were first determined. The resulting KNN graph was used to construct the SNN graph by calculating the neighborhood overlap (Jaccard index) between every cell and its 20 nearest neighbors. Clustering was then applied on this graph using the Louvain graph-based algorithm. Differential gene expression analysis was applied on each sample log normalized matrix. We used the Seurat function *FindAllMarkers()*, with a Logistic Regression test, and adding as variation factors, the origin sample and tissue of each cell and the version of CellRanger sequencing kit used. Only genes expressed in more than 10% of the cells in a cluster and having at least 0.10 of log

Fold-Change between compared groups were tested. We were able to detect low signals produced by genes with dropouts. For the volcano plots only the first condition was kept. At the end, only genes with a significative adjusted p-value (pv<0.05, false discovery rate (FDR) adjusted p-value) were kept and used to define each cluster.

### Human-mouse merging and seurat label transfer prediction score

To compare mouse and human macrophages, we selected conserved orthologue genes between both species. Corresponding gene symbols table was provided by the Mouse Genome Informatics database (Table S3). For genes with more than one corresponding orthologue in the other species, we took the mean expression of all orthologues. Seurat label transfer scoring algorithm was applied from mouse (as query) to human dataset (as reference) (Stuart et al., 2019). For the anchors searching step, we used the 10 000 most variable genes of the reference dataset. The following steps of the Seurat pipeline was applied with default parameters.

### Processing of published dataset

We downloaded the dataset of Azizi et al. (2018) (GSE114725). We used the classical pipeline for single cell analysis of Seurat V3 (without integration correction) from the raw count matrix (supplementary file GSE114725_rna_raw.csv.gz). We next perform Louvain graph-based clustering. At the resolution 0.9 we obtained 39 clusters: 14 clusters of T cells, 6 clusters of B cells, 5 clusters of NK cells, 1 cluster of pDCs, DC1, DC2, $CD16^+$ monocytes, $CD14^+$ monocytes, neutrophils or mast cells, 3 clusters of macrophages and 4 clusters of contaminating cells. We merged clusters of the same immune cell types (Figure 4B). We downloaded the dataset of Han et al. (2018) (GSE108097). We integrated 2 samples of virgin mammary gland and 1 sample of pregnant mammary gland from the raw data (supplementary file GSE108097_RAW.tar). We used the same pipeline described above including the integration step. Figure S3D shows clustering at the resolution 0.1.

### Bulk RNA-sequencing data processing and analysis

The raw sequencing data was initially aligned on the human reference genome hg19 or the murine reference genome mm10, using STAR aligner (v2.5.3a) (Dobin et al., 2013). Raw read counts matrix was made with STAR (using the parameter –quantMode GeneCounts). FastQ files quality control were applied with FastQC (removing of adapters and low-quality bases). Non-expressed genes (the sum of counts in all samples less than 2) and lowly expressed genes (background; $\log_2$ of the average of raw counts in all samples less than 2) were removed from the raw read count matrix. For differential expression analysis, we used the R package DESeq2 (version 1.24.0) (Love et al., 2014) with a p-value correction. The DESeq matrix was designed using the information of the patient and the cell type (following the formula design = ~ batch + condition). For the normalization, we used the median of ratios method (Anders and Huber, 2010) and the rlog transformation for visualization and clustering as proposed in the DESeq2 tutorial. We used ClueGO and Cytoscape for pathway annotation in Figures 6C and 7C (Bindea et al., 2009).

### Dynamic imaging analysis

A 3D image analysis was performed on x, y, and z planes using Imaris 7.4 (Oxford Instruments). Cellular motility parameters were then calculated. Tracks of >10% of the total recording time were included in the analysis. Tracks with high fluorescence intensity of FOLR2 in more than 3 time-points were assigned as« cells in contact ».

### Multispectral immunofluorescence on paraffin-embedded tissues and tissue microarrays

Paraffin-embedded tissue blocks from Institut Curie Hospital were cut with a microtome into fine slivers of 5 microns for subsequent analysis. Tissue microarrays (TMA) from breast cancer patients (TMA#1 n=122 spots; TMA#2 n=126 spots) were obtained commercially (AMSBIO, England). Immunostaining was processed in a Bond RX automated (Leica) with Opal™ 7-Color IHC Kits (Akoya Biosciences, NEL821001KT) according to the manufacturer's instructions using antibodies (see key resources table). Tissue sections were coverslipped with Prolong™ Diamond Antifade Mountant (Thermo Fisher) and stored at 4°C. Subsequently, slides were scanned using the Vectra® 3 automated quantitative pathology imaging system (Vectra 3.0.5; Akoya Biosciences). Multispectral images were unmixed and analyzed using the inForm Advanced Image Analysis Software (inForm 2.4.6; Akoya Biosciences) and the HALO software for immune subsets quantification.

### METABRIC data analysis

METABRIC gene expression data (Curtis et al., 2012), as well as clinical and sample level metadata were downloaded from cBioPortal. We annotated patient breast cancer subtypes by the following definitions: Luminal A (ER or PR positive, HER2 negative), Luminal B (ER positive, PR negative, HER2 positive), HER2 (ER and PR negative, HER2 positive) and TNBC (ER, PR, HER2 negative). Patients that died of other causes not related to their disease, as well as patients with breast sarcomas were removed. TNBC expression data was submitted to the TNBC type (Chen et al., 2012) algorithm that removed a further 6 patients from the TNBC cohort (MB-3297, MB-7269, MB-5008, MB-6052, MB-0179, MB-2993. The final cohort consisted of 1381 samples (250 TNBC, 114 HER2, 968 Luminal A and 49 Luminal B). To score individual samples for gene-signatures of interest, we Z-score normalised the gene expression data, and then calculated a mean level of expression across signature genes. To define the optimal cut-off by which to stratify patients into high and low groups according to the FOLR2 gene-signature and macrophage gene-signature expression, we fit univariate CoxPH models for the signature using cut-off values between 0.2 and 0.8 with increments of 0.02. The optimal cut-off was defined as

that with the lowest Wald test P value. We carried out survival analysis using the survival (3.1-12) and survminer (0.4.6) packages in R. To obtain the PAM50 subtype of patients we harnessed the R package genefu (2.22.1) (Gendoo et al., 2016) and the function *molecular.subtyping*. We computed pairwise Spearman correlations between signatures of interest and plotted these as a correlation heatmap using the corrplot R package (0.84). The MCP counter algorithm was used to infer immune cell abundance (Becht et al., 2016). Correlations that were statistically non-significant ($p<0.05$) were marked with a dash (-). We used ggplot2 (3.3.0) and ComplexHeatmap (2.7.6.1003) for plotting data (Gu et al., 2016).

### CPTAC data analysis

Data used in this publication were generated by the Clinical Proteomic Tumor Analysis Consortium (NCI/NIH). Log-ratio normalized proteomic data including clinical information and RNA sequencing data from the CPTAC BRCA study were downloaded (http://linkedomics.org/data_download/TCGA-BRCA/). BRCA patient samples annotated as either ER or PR positive, and HER2 negative, were selected for downstream analysis. Patients were then stratified according to a 25% cut-off by FOLR2 protein expression and univariate Cox regression analysis was carried out. Logrank test scores were plotted on Kaplan-Meier plots.

### Additional dataset analyses

Breast stroma microarray gene expression data (Finak et al., 2008) was downloaded from the GEO database under accession GSE9014. For genes with multiple mapped probes, the probe with the highest variance was selected. Signature score were computed as in other datasets, and for samples with duplicates the mean value was taken as the final per-patient signature score. Wilcoxon tests were used to compare patients with poor (increased rate of recurrence and shorter relapse-free survival) versus mixed/ good outcome. Gene expression data from the Wang dataset (Wang et al., 2005b) was downloaded from GEO (GSE2034). Again, in instances where multiple probes mapped to the same gene, the probe with the highest variance was selected. Patients could only be stratified into ER positive and negative groups based on the clinical data provided. Signature scores were computed as above.

### TCGA data analysis

We downloaded transcriptomic data (files ending.uncv2.mRNAseq_RSEM_normalized_log2.txt) generated by The Cancer Genome Atlas (TCGA) from the Broad Institute portal (http://gdac.broadinstitute.org). Samples from tumor-adjacent, healthy tissue were excluded (TCGA barcode ID ending in 11 or 12). Pan-cancer overall survival, progression-free interval and immune biomarker data were obtained from the supplemental information (Supp1a.txt) of Thorsson et al. (2018). Melanomas were split into those from the primary tumour and those from metastatic samples. Gene-signatures were calculated as above. Univariate Cox regression models were fit for predictors of interest as continuous variables. Hazard ratios, 95% confidence intervals and Wald test P values were extracted from each model. For the TCGA BRCA study, subtyping was carried out as above. HER2 positivity was determined by IHC or by FISH assay status. Altogether, there were 45 HER2 patients, 675 Luminal A, 35 Luminal B and 180 TNBC. 328 were indeterminate due to a lack of data. Additional clinical data were obtained using the TCGAbiolinks R package (2.18.0).

### GTEx to TCGA comparison

To compare TREM2 and FOLR2 mRNA expression between non-disease healthy tissue, tumour-adjacent normal tissue, and tumour tissue, we harnessed datasets from GTEx and TCGA consortia. For breast, colon and lung studies, we downloaded normalised transcriptomic data from Github (https://github.com/mskcc/RNAseqDB/tree/master/data/normalized). We used non-parametric, Wilcoxon T tests to compare TREM2 and FOLR2 expression between tissue types. **The Genotype-Tissue Expression** (GTEx) Project was supported by the Common Fund of the Office of the Director of the National Institutes of Health, and by NCI, NHGRI, NHLBI, NIDA, NIMH, and NINDS.

### Statistical analysis

The tests used for statistical analyses are described in the legends of each concerned figure and have been performed using GraphPad Prism v8 or R v3.4. Symbols for significance: ns, non-significant; *, <0.05, **, <0.01; ***, <0.001; ****, <0.0001. Values were expressed as mean ± SEM or median of biological replicates, as specified.

CellPress

# Supplemental figures

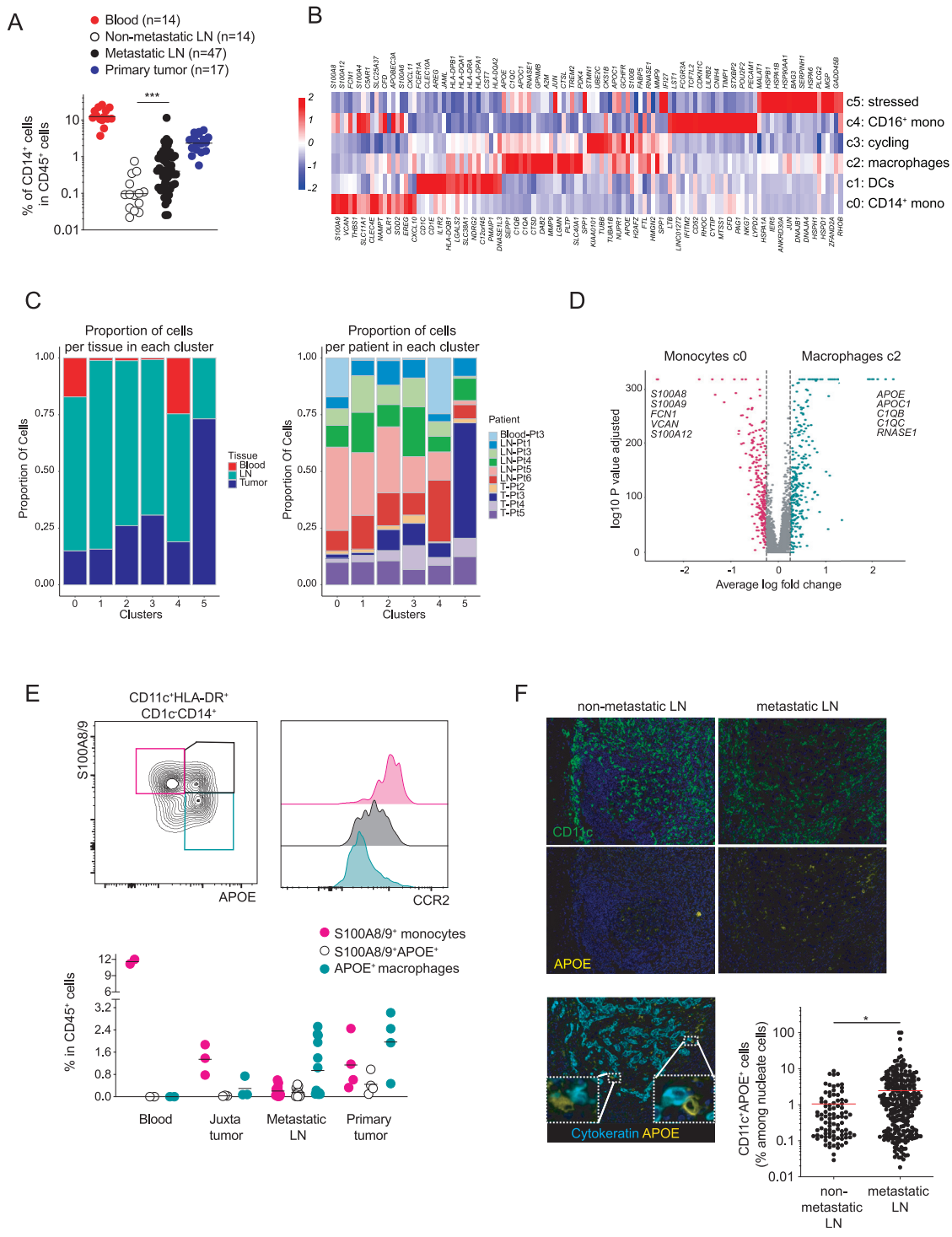


**Figure S1. APOE expression defines tumor-associated macrophages in human breast cancer related to Figure 1**

(A) Flow cytometry quantification of CD14$^+$ cells among CD45$^+$ cells in blood, nonmetastatic lymph nodes, metastatic lymph nodes, and primary tumors of treatment-naive patients with luminal breast cancer. Number of patients per group is indicated. Kruskal-Wallis multiple comparison test.

*(legend continued on next page)*

(B) Heatmap showing normalized expression of the top 10 most variable genes for each myeloid cell cluster defined in Figure 1D.
(C) Proportion of cells per tissue or per patients in each cluster.
(D) Volcano plot showing DEG between clusters 0 and 2. Selected genes among the Top25 were depicted.
(E) The intracellular proteins S100A8 and S100A9 are specifically expressed in $CD14^+$ monocyte cluster 0. S100A8/A9 expression follows the protein-expression pattern of cell-surface CCR2, which is not detected in our scRNA-seq dataset. Representative contour plot showing the expression of S100A8/9, APOE, and CCR2 in $CD11c^+HLA\text{-}DR^+CD1c^-CD14^+$ cells measured by flow cytometry. Quantification of each gates in blood, juxta-tumor tissue, metastatic lymph nodes, and primary tumors of treatment-naive patients with luminal breast cancer. At least n = 3 patients per group. Mann-Whitney test.
(F) Immunofluorescence images of $APOE^+$ macrophages and $cytokeratin^+$ tumor cells in nonmetastatic and metastatic lymph nodes. Quantification of $CD11c^+APOE^+$ cells among nucleated cells from multispectral images of nonmetastatic and metastatic lymph nodes (n = 3 patients; 1 nonmetastatic LN and 1 metastatic LN per patient were quantified). Mann-Whitney test.

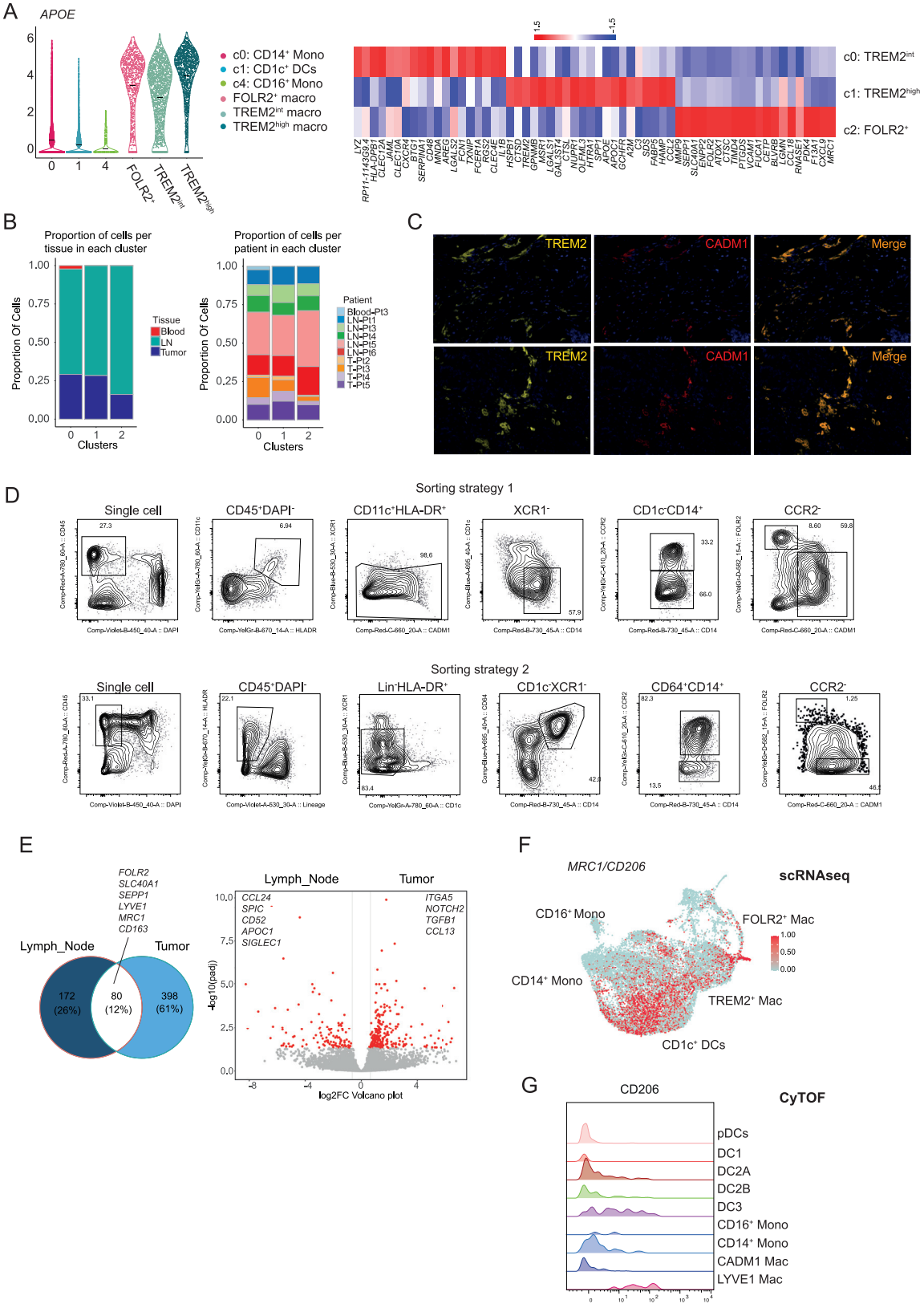


(legend on next page)

**Figure S2. Single-cell RNA sequencing reveals two main subsets of APOE$^+$ macrophages, related to Figure 2**

(A) Violin plots showing expression distributions *APOE* in cluster 0 (CD14$^+$ monocytes), cluster 1 (CD1c$^+$ DCs), cluster 4 (CD16$^+$ monocytes), FOLR2$^+$ macrophages, TREM2$^{int}$, and TREM2$^{high}$ macrophages. Heatmap showing normalized expression of the top 20 most variable genes for each macrophage cluster defined in Figure 2A.

(B) Proportion of cells per tissue or per patients in each cluster.

(C) Immunofluorescence images of TREM2$^+$CADM1$^+$ macrophages in colorectal cancer tissue section.

(D) Gating strategies for FACS sorting of FOLR2$^+$ and CADM1$^+$ macrophages isolated from metastatic lymph nodes or primary tumors. To avoid contamination by XCR1$^+$CADM1$^+$ DC1, CADM1$^+$ macrophages were sorted according to the gating strategy 2, which includes a lineage excluding lymphocytes and DCs (BTLA, CD26, CD3, and CD19).

(E) Venn diagram showing specific and common DEG of FOLR2$^+$ macrophage bulk RNA-seq data from tumor-draining LNs and tumors.

(F) UMAP plot showing promiscuous expression of *MRC1/CD206* between CD1c$^+$ DCs, CD14$^+$ monocytes, and APOE$^+$ macrophages.

(G) MRC1/CD206 protein expression measured by CyTOF in myeloid cell subsets in tumor-draining metastatic LNs.

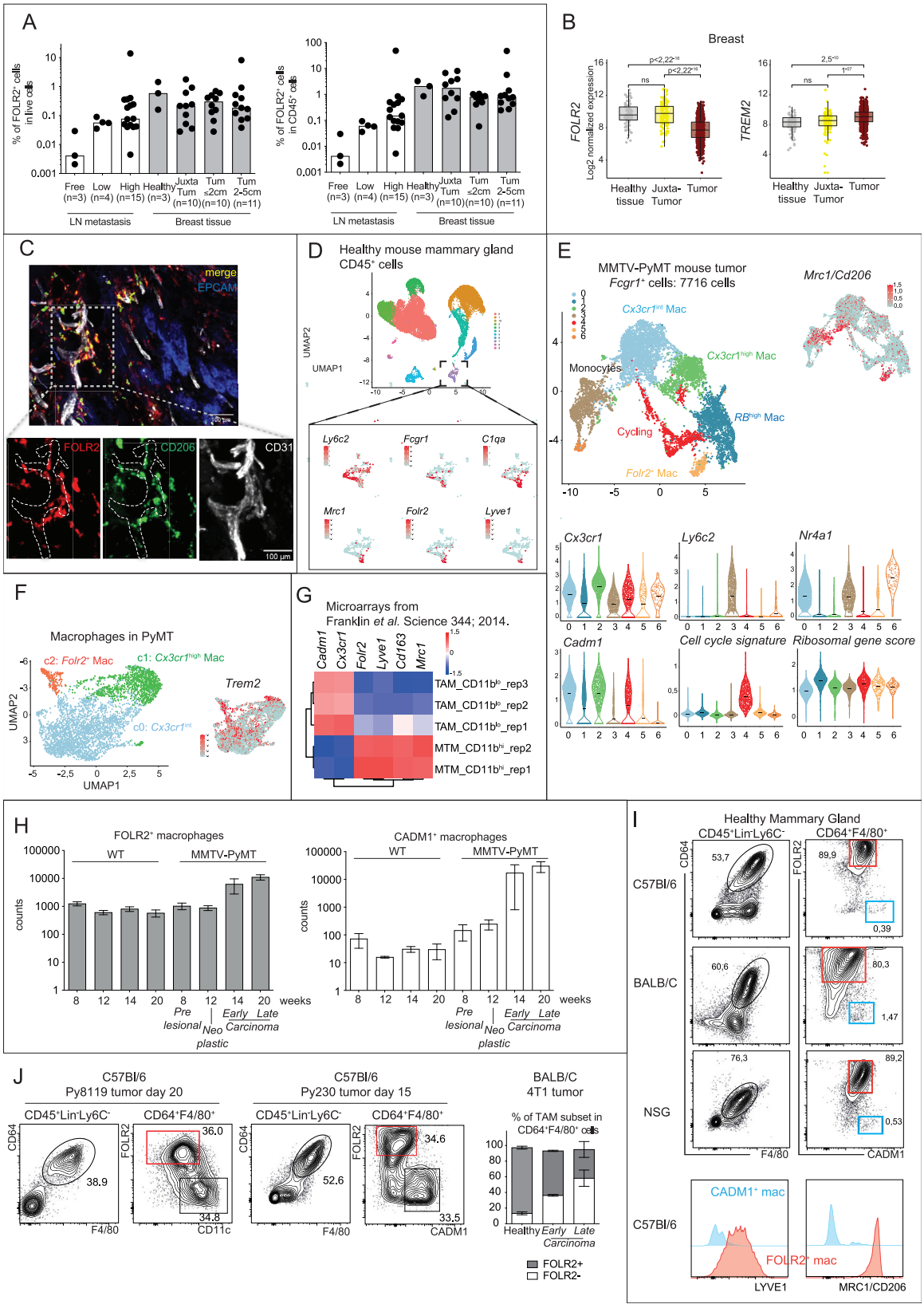


(legend on next page)

**Figure S3. FOLR2$^{+}$ macrophages are tissue-resident macrophages, related to Figure 3**

(A) Quantification of FOLR2$^{+}$APOE$^{+}$ and FOLR2$^{-}$APOE$^{+}$macrophages across distinct breast cancer patient tissues (tumor-draining LNs, healthy breast and breast tumors) using flow cytometry. Percentage of each population among total live cells or CD45$^{+}$ cells. Number of patients per group is indicated. Mann-Whitney test.

(B) *FOLR2* and *TREM2* mRNA expression between healthy tissue, tumor-adjacent normal tissue, and tumor tissue from GTEx and TCGA datasets.

(C) Representative confocal immunofluorescence images performed in primary breast cancer tissues. showing FOLR2$^{+}$CD206$^{+}$ macrophages colocalizing with CD31$^{+}$ vessels, near EPCAM$^{+}$ tumor cells. Scale bars, 100 μ.

(D) UMAP plot visualization of CD45$^{+}$ hematopoietic cells isolated from healthy mouse mammary gland from the Han et al. dataset. Feature plots illustrating expression of *Ly6c2*, *Fcgr1*, *C1qa*, *Mrc1*, *Folr2*, and *Lyve1* in macrophages.

(E) UMAP plot vizualization of *Fcgr1*$^{+}$ cells (n = 7,716) isolated from mammary tumors of 23-week-old PyMT mice (n = 2). Violin plots illustrating expression distributions of *Cx3cr1*, *Ly6c2*, *Nr4a1*, *Cadm1*, a cell cycle gene signature and a ribosomal gene score. UMAP plot showing promiscuous expression of *Mrc1*/*CD206* between *Ly6C*$^{+}$ monocytes, *Cx3Cr1*$^{+}$, and *Folr2*$^{+}$ macrophages.

(F) Feature plots illustrating expression of *Trem2* in macrophage subsets from mammary tumors (see Figure 3E).

(G) Heatmap showing selected gene expression in TAM and MTM murine subsets defined by Franklin et al. (2014).

(H) Quantification of Folr2$^{+}$ mammary macrophages by flow cytometry during tumor development. Bar plots represent cell count of Folr2$^{+}$ macrophage in WT mammary glands (n = 16) or tumors (n = 16). Data are represented as mean ± SEM.

(I) Flow cytometry analysis of CD64$^{+}$F4/80$^{+}$ macrophage populations in healthy mouse mammary glands of various mouse strains: C57Bl/6, BALB/C, and NSG. Protein expression of LYVE1 and CD206 in FOLR2$^{+}$ macrophages in C57Bl/6 mice healthy mammary glands.

(J) Quantification of FOLR2$^{+}$ and FOLR2$^{-}$ macrophages by flow cytometry during tumor development in Py8119 and Py230 tumor mouse models. Representative contour plots of macrophage subsets in mammary gland from Py8119 or Py230 tumor-bearing mice, 20 or 15 days after tumor transplant respectively. Right panel shows a longitudinal quantification of FOLR2$^{+}$ and FOLR2$^{-}$ macrophages in healthy mammary glands and early and late 4T1 carcinoma transplanted in BALB/C mice.

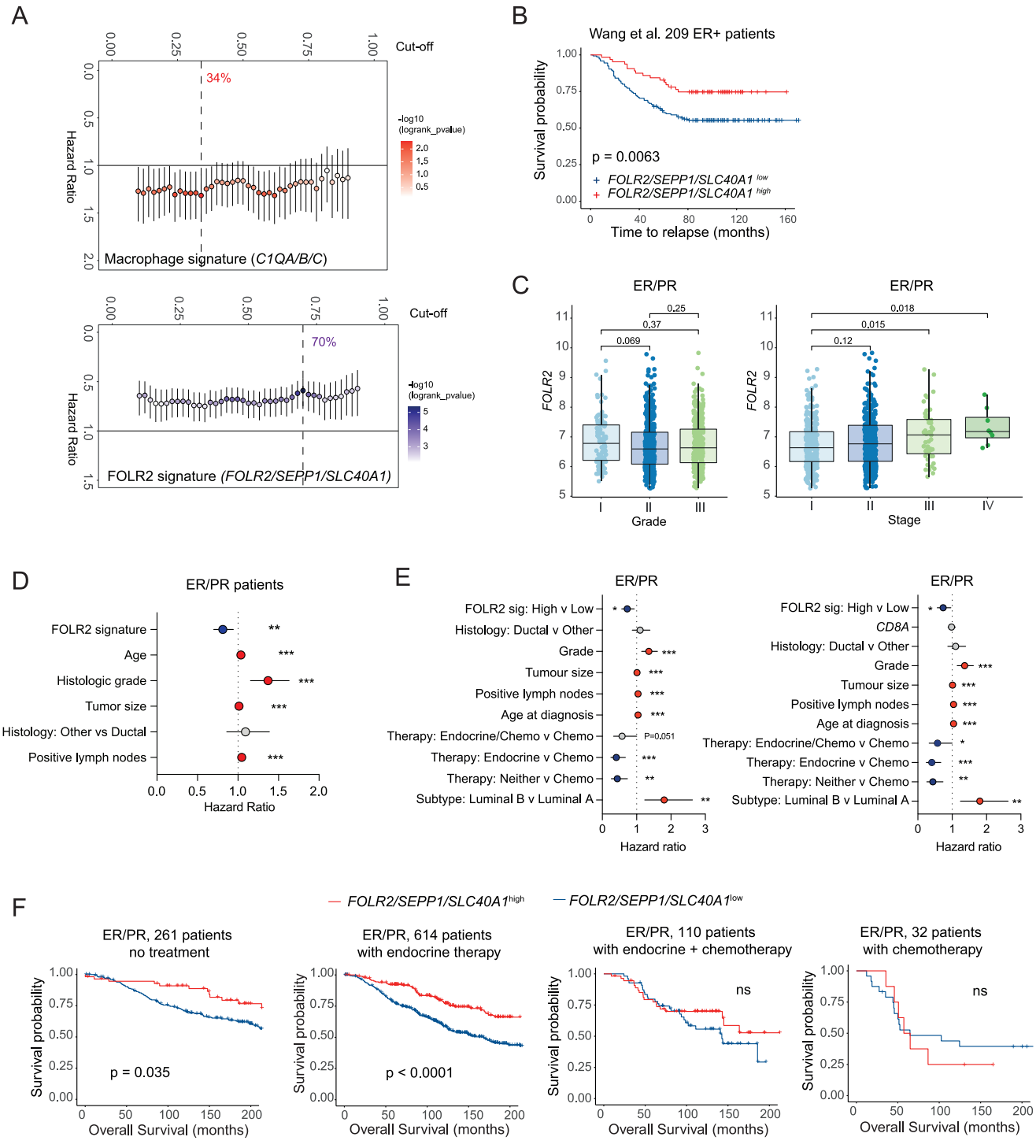


**Figure S4. FOLR2$^+$ macrophages correlate with increased survival in patients with breast cancer, related to Figure 4**

(A) To determine the association of the gene signatures with patient overall survival, we tested a range of cutoff values for stratifying patients. Graphs showing the hazard ratio (plus error) forest plot for the pan macrophage signature (*C1QA/C1QB/C1QC*) (top panel) and the FOLR2 signature (FOLR2/SLC40A1/SEPP1) (lower panel) in the METABRIC LuminalA/B (ER/PR) dataset using cutoff values between 0.2 and 0.8 with 0.02 increments. The color of the points correlates with p value strength. More blue/red = stronger predictive value. With a 34% cutoff or a 70% cutoff, the pan-macrophage signature or the FOLR2 signature are bad and good prognostic factors, respectively, in LumA/B patients (n = 1,017 patients).

(B) Kaplan-Meier survival curves generated for the FOLR2$^+$ macrophage gene signature (*FOLR2/SEPP1/SLC40A1*) in the Wang et al. luminal breast cancer cohort (n = 209 patients). Patients were divided in high- and low-expressing groups based on the 70% quantile of signature expression.

*(legend continued on next page)*

(C) *FOLR2* mRNA expression in luminal (ER/PR) breast tumors of different grades and stages from the METABRIC dataset.
(D) Multivariate analysis of the prognostic value of the FOLR2 gene signature (*FOLR2*/*SEPP1*/*SLC40A1*) as a continuous variable adjusted for age, histological grade, tumor size, histology (reference = ductal), and number of disease-positive lymph nodes. Hazard ratios with 95% confidence intervals are shown. Asterisks refer to p values from the Wald test for each variable. Patients are luminal A/B from the METABRIC dataset (n = 1,017 patients).
(E) As in (D), these multivariate analyses also include the treatment received by the patients and the subtypes (luminal B versus A) and *CD8A* expression (right panel). Interestingly, the FOLR2 signature has additional prognostic power independently of *CD8A* expression, (which probes $CD8^+$ T cell infiltration in tumors), suggesting a direct role of $FOLR2^+$ macrophages to pathogenesis.
(F) To test the prognostic power of the FOLR2 signature in distinct treatment groups, we performed a univariate analysis in patients with luminal BC classified according to the therapy received. Kaplan-Meier survival curves generated for the $FOLR2^+$ macrophage gene signature (*FOLR2*/*SEPP1*/*SLC40A1*) in the METABRIC dataset in luminal A/B patients stratified by treatment received. The FOLR2 gene signature has a significant prognostic value in patients receiving endocrine therapy alone. The FOLR2 gene signature did not have significant prognostic power in patients receiving endocrine therapy + chemotherapy or chemotherapy alone. Patients were divided in high- and low-expressing groups based on the 70% quantile of signature expression. Number of patients is indicated for each groups.

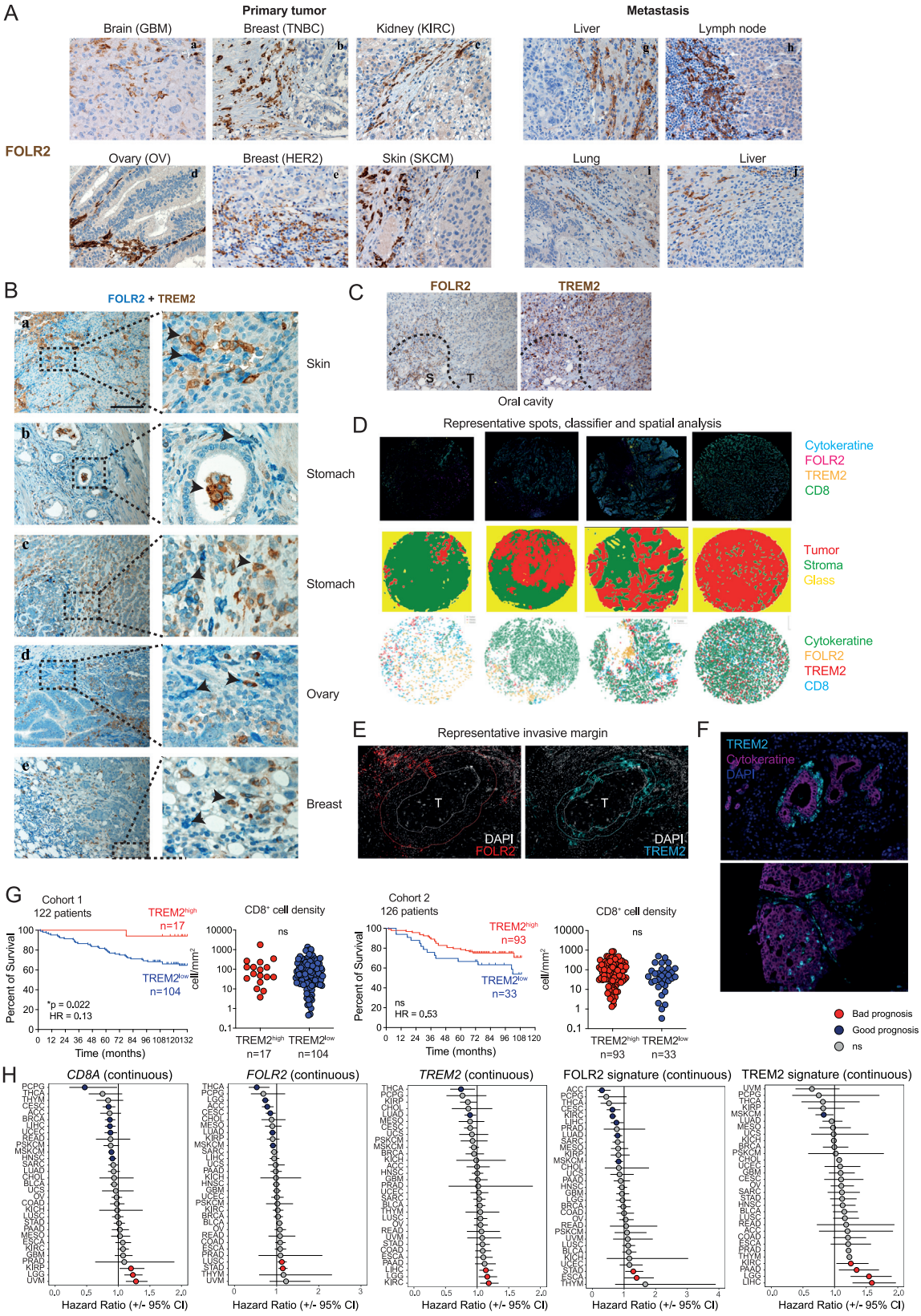


*(legend on next page)*

**Figure S5. FOLR2$^+$ macrophages are spatially separated from TREM2$^+$ macrophages, related to Figure 5**

(A) Spatial distribution of FOLR2$^+$ TAMs in human primary and metastatic cancer. Sections are from cases of primary cancer including (a) glioblastoma, (b) triple negative breast carcinoma, (c) renal clear cells carcinoma, (d) serous ovarian carcinoma, (e) HER2$^+$ breast carcinoma, (f) cutaneous melanoma, and cases of metastatic carcinomas to liver (g and j), lymph node (h), and lung (i) stained as labeled.

(B) Costaining for FOLR2 and TREM2 confirmed mutually exclusive expression of the two markers on distinct cells. Sections are from cutaneous melanomas (a), gastric carcinomas (b and c), a serous ovarian carcinoma (d), a breast carcinoma (e), and stained as labeled; low (left panels) and high (right panels) magnifications are reported. Double stain from FOLR2 and TREM2 confirms a dominant mutually exclusive distribution of the two markers. Sections are counterstained with Mayer's hematoxylin. Magnification = 100×, scale bars, 200 micron (left panels); 400×, scale bars, 100 micron (right panels).

(C) Spatial distribution of FOLR2$^+$ macrophages and TREM2$^+$ TAMs in human primary oral cavity squamous cell carcinoma.

(D) (Upper row) Representative images of multiplex immunofluorescence from tissue microarray stained for cytokeratin, FOLR2, TREM2, and CD8. (Middle row) Automated classifier of CK$^+$ tumor nest (red) versus CK$^-$ tumor stroma (green). (Lower row) Spatial analysis of FOLR2$^+$ (yellow), TREM2$^+$ (red), and CD8$^+$ (cyan) cells with the HALO software.

(E) Representative images of multiplex immunofluorescence from tissue microarray stained for FOLR2 (red) or TREM2 (cyan) and showing a representative invasive margin and mean distance between macrophages subsets and the tumor nest (calculated in Figure 5C).

(F) Representative images of multiplex immunofluorescence stained for cytokeratin (violet) and TREM2 (cyan) and illustrating the spatial distribution of TREM2$^+$ cells clustering around (left) or infiltrating (right) tumor nests.

(G) Kaplan-Meier survival curves generated for TREM2$^+$ macrophage density calculated by multispectral analysis of tumors from 2 cohorts (cohort 1: n = 122 patients and cohort 2: n = 126 patients). Graph showing density of CD8$^+$ T cells in tumors with high or low TREM2$^+$ cell density. Patients were divided in high- and low-cell density groups based on best p value cutoff (**$p \leq 0.01$).

(H) Graphs showing the hazard ratio (plus error) forest plots for the various gene expression (*CD8A, FOLR2, TREM2*) or signature scores (*FOLR2*/*SEPP1*/*SLC40A1* and *TREM2*/*SPP1*) as continuous variable for cancers of the TCGA dataset.

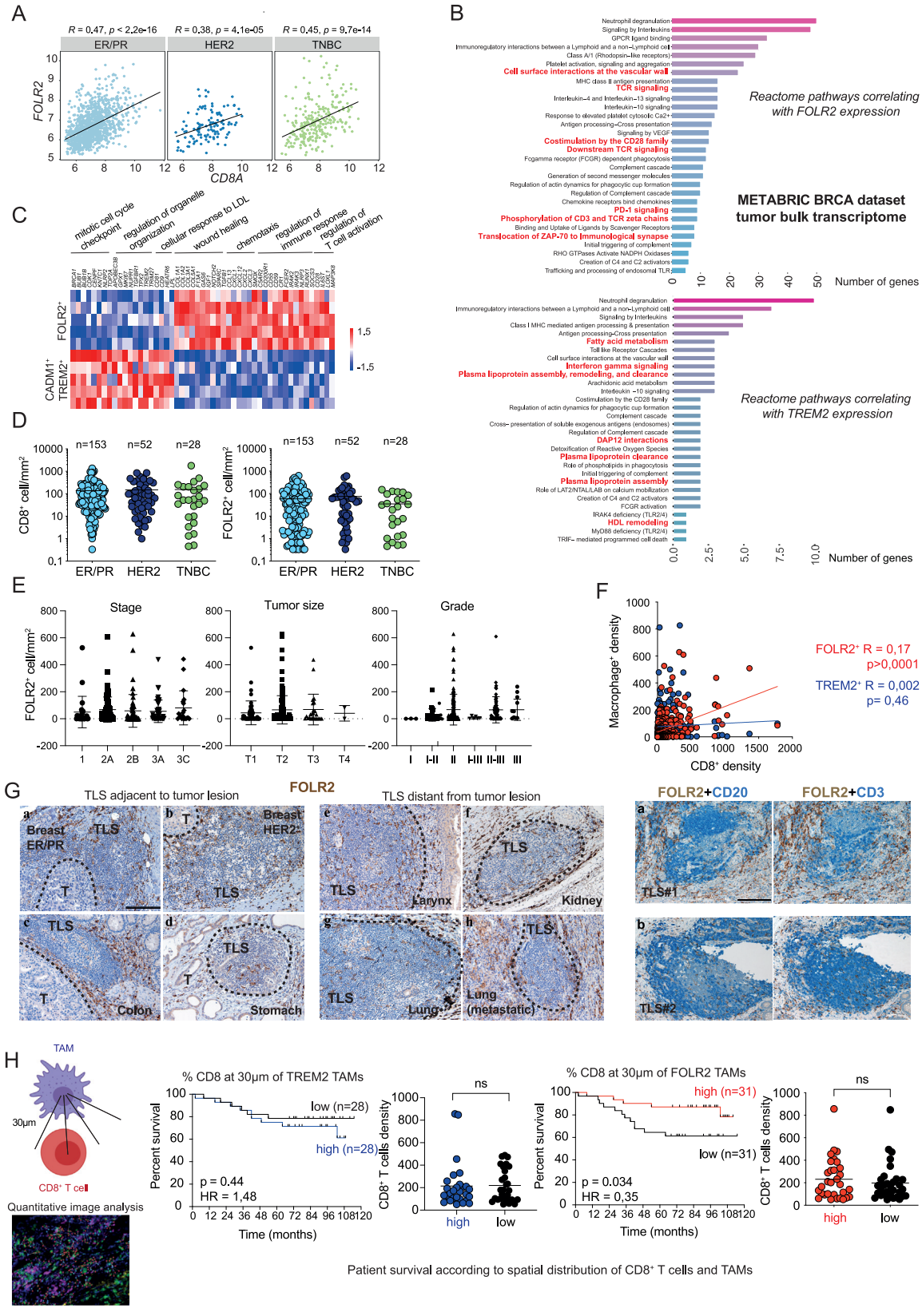


(legend on next page)

**Figure S6. FOLR2$^+$ macrophages are enriched in CD8$^+$ T cells infiltrated tumors and colocalize with lymphoid aggregates across cancers, related to Figure 6**

(A) Correlation between *FOLR2* and *CD8A* expression in patients from the METABRIC dataset stratified by subtypes.

(B) Bulk transcriptome of breast tumors from the METABRIC dataset. Reactome pathway analysis (Yu and He, 2016) for genes positively correlating with either *FOLR2* or *TREM2* expression ($r \geq 0.4$). p value < 0.01.

(C) Heatmap showing expression by FOLR2$^+$ and CADM1$^+$TREM2$^+$ macrophages of representative genes of differentially enriched gene pathways analyzed in bulk RNA-seq of FOLR2$^+$ and CADM1$^+$TREM2$^+$ macrophages isolated from primary tumors (see Figure 6D).

(D) CD8$^+$ cell and FOLR2$^+$ cell densities quantified by multispectral immunofluorescence in the two tissue microarrays. Patients are stratified by subtypes. Mann-Whitney test.

(E) FOLR2$^+$ cell density quantified by multispectral immunofluorescence in the two tissue microarrays. Patients are stratified by tumor stage, size, and grade. Mann-Whitney test.

(F) Correlation between FOLR2$^+$ cell density (red line) or TREM2$^+$ cell density (blue line) with the CD8$^+$ cell density quantified by multispectral immunofluorescence in the two tissue microarrays (see Figure 4D).

(G) FOLR2 staining: sections are from primary luminal A (for anti-FOLR2. FOLR2$^+$ macrophages are found in TLS adjacent to (a–d) or distant from (e–h) neoplastic cells. Sections are counterstained with Mayer's hematoxylin. Magnification 100×, scale bars, 200 μ (a–h). FOLR2$^+$CD20$^+$CD3$^+$ staining: sections are from two colorectal carcinomas (a and b) and stained as labeled. FOLR2$^+$ TAMs are found at the periphery of TLS, defined by CD20 and CD3 aggregates, as well as within the CD3$^+$ T cell area. Magnification = 100×. Sections are counterstained with Mayer's hematoxylin.

(H) Quantitative image analysis of CD8$^+$ cells at a distance of 30 μm from macrophages subsets in the tissue microarray (cohort 2). Kaplan-Meier survival curves generated for the % of CD8$^+$ cells at a distance of 30 μm from macrophage subsets in tumors presenting a CD8$^+$ cell density superior to 50 cells/mm$^2$. Graph showing density of CD8$^+$ T cells in tumors. Patients were divided in high and low % of CD8$^+$ cells near macrophage subset based on a 50% cutoff.

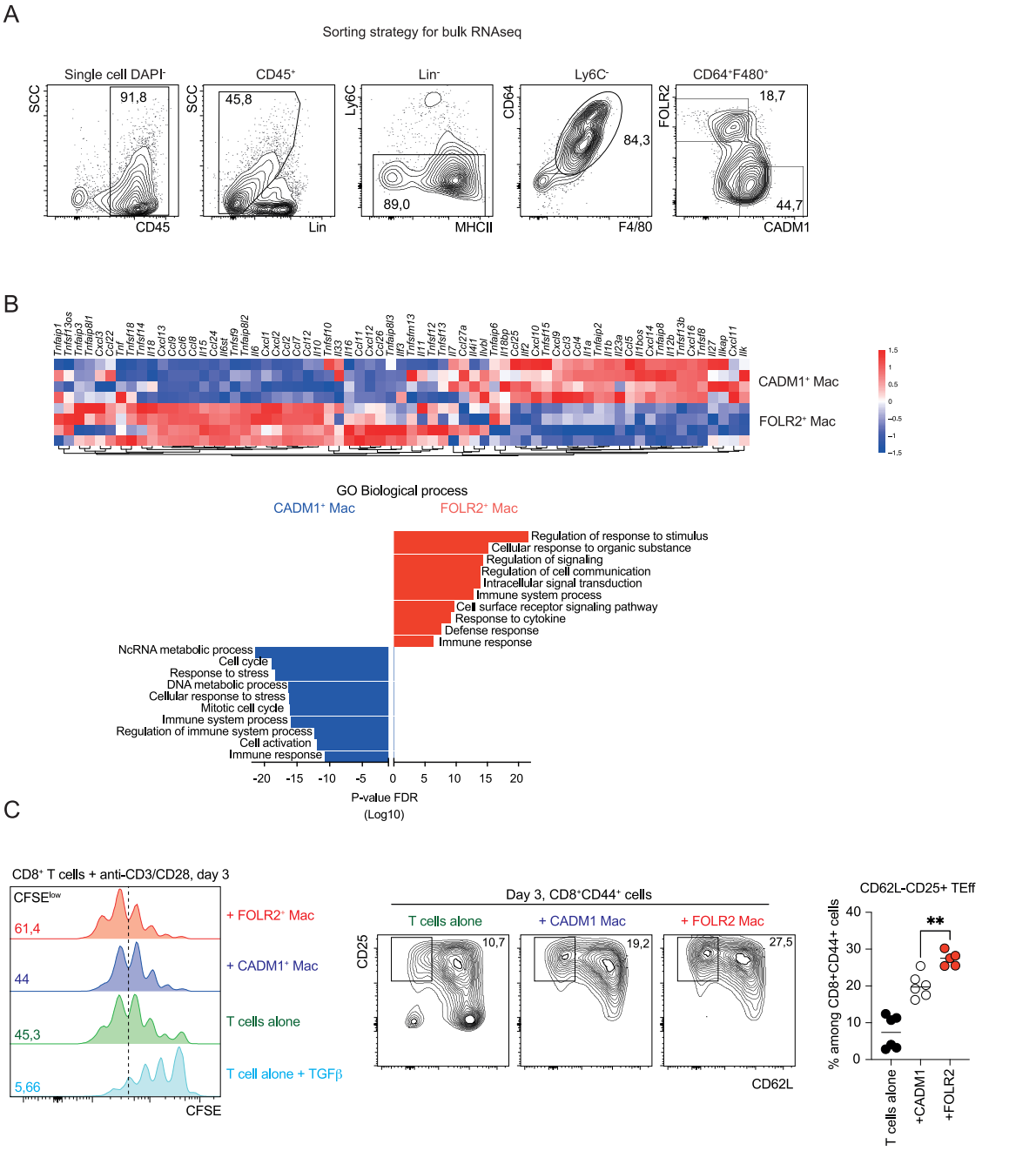


**Figure S7. FOLR2$^+$ macrophages respond to tumor growth and acquire T cell-priming ability, related to Figure 7**

(A) Gating strategy for FACS-sorting of FOLR2$^+$ and CADM1$^+$ macrophages from mammary tumors of 22-week-old PyMT mice. Lineage includes anti-CD3,-CD19,-NKP46,-B220,-Ly6G antibodies.

(B) Heatmaps of selected immune related genes between FOLR2$^+$ and CADM1$^+$ macrophages isolated from the same tumors (bulk RNA-seq). Differential enrichment of gene pathways between FOLR2$^+$ and CADM1$^+$ macrophages.

(C) T cell proliferation and activation were assessed by flow cytometry after 3 days. Representative histograms showing CFSE dilution by T cells alone, with TGF-β or after coculture with FOLR2$^+$ or CADM1$^+$ macrophages isolated from the same tumor. Representative dot plots showing CD25 and CD62L expression in CD8$^+$CD44$^+$ effector T cells. The gate highlights fully differentiated CD25$^+$CD62L$^-$ effector T cells. Quantification is shown on the right. Data are representative of 3 experiments. Unpaired t test.